

Electronic structure of selected materials with superconductivity and topologically nontrivial phases

Marcin Rosmus

Supervisor: dr. hab. Paweł Starowicz



JAGIELLONIAN UNIVERSITY
IN KRAKÓW

Marian Smoluchowski Institute of Physics

A dissertation submitted for the degree of
Doctor of Philosophy

June 2023

Oświadczenie

Ja niżej podpisany Marcin Rosmus (nr indeksu: 1063746) doktorant Wydziału Fizyki, Astronomii i Informatyki Stosowanej Uniwersytetu Jagiellońskiego oświadczam, że przedłożona przeze mnie rozprawa doktorska pt. „Electronic structure of selected materials with superconductivity and topologically non-trivial phases” jest oryginalna i przedstawia wyniki badań wykonanych przeze mnie osobiście, pod kierunkiem dra hab. Pawła Starowicza. Pracę napisałem samodzielnie.

Oświadczam, że moja rozprawa doktorska została opracowana zgodnie z Ustawą o prawie autorskim i prawach pokrewnych z dnia 4 lutego 1994 r. (Dziennik Ustaw 1994 nr 24 poz. 83 wraz z późniejszymi zmianami).

Jestem świadom, że niezgodność niniejszego oświadczenia z prawdą ujawniona w dowolnym czasie, niezależnie od skutków prawnych wynikających z ww. ustawy, może spowodować unieważnienie stopnia nabytego na podstawie tej rozprawy.

Kraków, dnia

Marcin Rosmus

Acknowledgment

First and foremost, I would like to express my sincere gratitude to my supervisor dr. hab. Paweł Starowicz for his guidance during the writing of this thesis and for introducing me to the world of condensed matter physics.

I am grateful to dr. Natalia Olszowska and prof. dr. hab. Jacek J. Kołodziej from URANOS beamline at the National Synchrotron Radiation Centre SOLARIS in Krakow for help during experiments and many valuable discussions on angle-resolved photoelectron spectroscopy technique. I am also grateful to the entire SOLARIS team for the professional performance of the synchrotron centre.

I would like to offer my special thanks to dr. Rafał Kurleto and dr. Bogusław Penc for help with sample preparation and measurements.

I am also grateful to dr. hab. Andrzej Ptok for his help during my PhD studies and his advice concerning the explanation of theoretical aspects.

I am deeply grateful to my family and friends for their support and patience.

Streszczenie

W ramach niniejszej pracy doktorskiej przeprowadzono badania struktury elektronowej metodą kątoworozdzielczej spektroskopii fotoelektronów (ARPES) na następujących związkach: nadprzewodnikach opartych na żelazie $\text{FeTe}_{0.65}\text{Se}_{0.35}$ i $\text{Fe}_{1-y}\text{M}_y\text{Te}_{0.65}\text{Se}_{0.35}$ ($\text{M} = \text{Ni}$ i Co); nienadprzewodzącym CaFe_2As_2 oraz $\text{CaFe}_{2-x}\text{Co}_x\text{As}_2$ w którym podstawianie kobaltu w miejsce żelaza powoduje pojawienie się nadprzewodnictwa; LaAgSb_2 , dla którego obserwuje się fazę nadprzewodzącą oraz fazę fal gęstości ładunku; oraz nadprzewodzącym LaCuSb_2 .

W związku $\text{Fe}_{1.01}\text{Te}_{0.65}\text{Se}_{0.35}$ podstawianie niklu lub kobaltu w miejsce żelaza powoduje tłumienie nadprzewodnictwa. Badania przeprowadziliśmy na związku niedomieszkowanym oraz na $\text{Fe}_{0.97}\text{Ni}_{0.05}\text{Te}_{0.65}\text{Se}_{0.35}$, $\text{Fe}_{0.91}\text{Ni}_{0.11}\text{Te}_{0.65}\text{Se}_{0.35}$ i $\text{Fe}_{0.94}\text{Co}_{0.09}\text{Te}_{0.67}\text{Se}_{0.33}$. Zaobserwowaliśmy deformację struktury pasmowej pod wpływem domieszkowania oraz wyznaczyliśmy przesunięcia pasm oraz zmiany objętości powierzchni Fermiego. Elektronowa część powierzchni Fermiego zwiększa się, natomiast dziurowa zanika, co skutkuje zmianą w jej topologii nazywaną przejściem Lifshitz'a. Pokazaliśmy, że zmiany w strukturze pasmowej nie mogą być traktowane jako proste przesunięcie energii Fermiego, ale odkształcenie całej struktury. Domieszkowanie kobaltem okazało się mieć znacznie większy wpływ na strukturę pasmową niż domieszkowanie niklem, przy czym to domieszkowanie niklem wpływa we większym stopniu na właściwości transportowe tych związków. Oznacza to, że podstawianie żelaza niklem prowadzi do większego rozpraszania na domieszkach i większych efektów korelacji niż podstawianie kobaltem. Ponadto, pokazaliśmy, że domieszkowanie powoduje zanikanie nestingu powierzchni Fermiego.

W przypadku CaFe_2As_2 podstawianie kobaltu w miejsce żelaza powoduje pojawianie się nadprzewodnictwa w układzie oraz przejście z fazy antyferromagnetycznej o strukturze ortorombowej do fazy paramagnetycznej o strukturze tetragonalnej. Zbadaliśmy trzy próbki: nienadprzewodzący CaFe_2As_2 oraz nadprzewodzące $\text{CaFe}_{1.93}\text{Co}_{0.07}\text{As}_2$ i $\text{CaFe}_{1.85}\text{Co}_{0.15}\text{As}_2$. Zaobserwowaliśmy dwa typy struktury elektronowej, odpowiadającą fazie antyferromagnetycznej dla próbek niedomieszkowanej i słabo domieszkowanej oraz fazie paramagnetycznej dla próbki silnie domieszkowanej. W ramach fazy antyferromagnetycznej nie zaobserwowaliśmy wyraźnych zmian struktury elektronowej. Dla obu próbek antyferromagnetycznych zaobserwowaliśmy istnienie stożków Diraca, które w tym związku nie były dotąd raportowane. Struktura elektronowa silnie domieszkowanego związku składa się z pasm przecinających poziom Fermiego w punktach $\bar{\Gamma}$ i \bar{X} i tworzących kwasi-dwuwymiarowe walce na powierzchni Fermiego. Jest to struktura typowa dla większości nadprzewodników żelazowych.

LaAgSb_2 jest semimetałem Diraca, w którym obserwuje się nadprzewodnictwo i fale gęstości ładunku. Powierzchnia Fermiego tego związku składa się z czterech pasm tworzących kształt diamentu. Zaobserwowaliśmy występowanie liniowych pasm tworzących charakterystyczne przecięcia o kształcie X, linie nodalne ciągnące się w kierunku Γ -Z oraz stany powierzchniowe sugerujące, że badana powierzchnia odpowiada

terminacji LaSb. Nie udało się potwierdzić istnienia stożków Diraca na odcinku $\bar{\Gamma}$ - \bar{M} , które było sugerowane we wcześniejszych publikacjach na temat tego związku.

Struktura LaCuSb₂ również składa się z liniowych pasm tworzących przecięcia w kształcie X. Istnienie takich świadczy o potencjalnym występowaniu fermionów Diraca w obu tych układach. W związku tym zaobserwowaliśmy także linie nodalne na odcinku Γ -Z. Porównanie powierzchni Fermiego LaCuSb₂ i LaAgSb₂ wskazuje na silniejszy nesting w pierwszym z nich. Długości zaobserwowanych wektorów nestingu są inne niż wektory modulacji fal gęstości ładunku w LaAgSb₂, dlatego nie tłumaczą istnienia tej fazy.

Abstract

The doctoral dissertation is devoted to the study of the electronic structure of the following compounds: iron-based superconductors $\text{Fe}_{1.01}\text{Te}_{0.65}\text{Se}_{0.35}$ and $\text{Fe}_{1-y}\text{M}_y\text{Te}_{0.65}\text{Se}_{0.35}$ ($\text{M} = \text{Ni}$ and Co); parent compound CaFe_2As_2 and $\text{CaFe}_{2-x}\text{Co}_x\text{As}_2$ system, in which the substitution of cobalt in a place of iron induces superconductivity to; LaAgSb_2 , for which a superconducting phase and a phase of charge density waves are observed; and superconducting LaCuSb_2 . Measurements were carried out using the angle-resolved photoemission spectroscopy (ARPES) technique.

For the $\text{Fe}_{1.01}\text{Te}_{0.65}\text{Se}_{0.35}$ compound, the substitution of nickel or cobalt in place of iron results in suppression of superconductivity. We conducted research on the undoped compound and on $\text{Fe}_{0.97}\text{Ni}_{0.05}\text{Te}_{0.65}\text{Se}_{0.35}$, $\text{Fe}_{0.91}\text{Ni}_{0.11}\text{Te}_{0.65}\text{Se}_{0.35}$ and $\text{Fe}_{0.94}\text{Co}_{0.09}\text{Te}_{0.67}\text{Se}_{0.33}$. We observed the deformation of the band structure under the influence of doping and determined band shifts and changes in the volume of the Fermi surface. The electron part of the Fermi surface increases while the hole part disappears, which results in a change in its topology called the Lifshitz transition. We have shown that changes in the band structure cannot be understood as a simple Fermi energy shift, but as a deformation of the entire structure. Cobalt doping turned out to have a much greater effect on the band structure than nickel doping, with nickel doping having a greater impact on the transport properties of these compounds. This means that substituting iron with nickel leads to a greater scattering on impurities and greater correlation effects than substituting with cobalt. Moreover, we have shown that doping causes the Fermi surface nesting to disappear.

In the case of CaFe_2As_2 , the substitution of cobalt in place of iron causes the appearance of superconductivity in the system and the transition from the antiferromagnetic phase with orthorhombic structure to the paramagnetic phase with tetragonal structure. We tested three samples: non-superconducting CaFe_2As_2 and superconducting $\text{CaFe}_{1.93}\text{Co}_{0.07}\text{As}_2$ and $\text{CaFe}_{1.85}\text{Co}_{0.15}\text{As}_2$. We observed two types of electronic structure, representing the antiferromagnetic phase for the undoped and lightly doped samples and the paramagnetic phase for the highly doped sample. As part of the antiferromagnetic phase, we did not observe any clear changes in the electronic structure. For both antiferromagnetic samples, we observed the existence of Dirac cones, it has not been reported so far for this compound. The electronic structure of the highly doped compound consists of bands that cross the Fermi level at points $\bar{\Gamma}$ and \bar{X} forming quasi-two-dimensional cylinders on the Fermi surface. This structure is typical of most iron-based superconductors.

LaAgSb_2 is a Dirac semimetal where superconductivity and charge density waves are observed. The Fermi surface of this compound consists of four bands that form a diamond-like shape. We observed the presence of linear bands that form characteristic X-shaped crossings, nodal lines that extend in the Γ -Z direction and surface states suggesting that the studied surface corresponds to the termination of LaSb . It was not possible to confirm the existence of Dirac cones in the section $\bar{\Gamma}$ - \bar{M} which was suggested in earlier publications on that compound.

The structure of LaCuSb_2 also consists of linear bands that form X-shaped crossings. The existence of such bands indicates the potential presence of Dirac fermions in both systems. Therefore, we also observed the nodal lines in the direction Γ -Z. Comparison of the Fermi surfaces of LaCuSb_2 and LaAgSb_2 indicates stronger nesting in the first compound. In LaAgSb_2 the lengths of the observed nesting vectors are different from the charge density wave modulation vectors; therefore they do not explain the existence of this phase.

Table of Contents

1. Motivation	13
2. Introduction	15
2.1. Superconductivity	15
2.1.1. London's Theory and Meissner Effect	17
2.1.2. BCS Theory	19
2.1.3. Superconductivity in Iron Pnictides and Chalcogenides	21
2.1.4. Topological Superconductivity	24
2.2. Topological Materials	24
2.2.1. Dirac Equation	26
2.2.2. Quantum Hall Effect	28
2.2.3. Topological Insulators	29
2.2.4. Topological Dirac Semimetals	30
2.2.5. Topological Weyl Semimetals	31
2.2.6. Topological Nodal-Line Semimetals	33
2.2.7. Topological Chiral Semimetals	34
2.3. Description of Investigated Systems	35
2.3.1. $\text{FeTe}_x\text{Se}_{1-x}$	35
2.3.2. $\text{CaFe}_{2-x}\text{Co}_x\text{As}_2$	37
2.3.3. LaTSb_2 (T=Ag, Cu)	40
3. Experimental Technique	42
3.1. Angle-Resolved Photoemission Spectroscopy	42
3.2. Measurement Systems	47
4. Effect of Electron Doping in $\text{FeTe}_{1-y}\text{Se}_y$ Realized by Co and Ni Substitution	50
5. Observation of Dirac Dispersions in Co-doped CaFe_2As_2	66
6. Electronic Band Structure and Surface States in Dirac Semimetal LaAgSb_2	76
7. Dirac Dispersions and Fermi Surface Nesting in LaCuSb_2	99
8. Summary	109
9. List of Published Articles	110
10. Bibliography	112

1. Motivation

The motivation for this doctoral thesis was the study of superconductivity, in particular changes in the electronic structure occurring when selected atoms are replaced in chemical formulas. Three types of superconducting compounds were selected, in which doping resulted in different effects. To determine changes in the electronic structure, systematic angle-resolved photoelectron spectroscopy (ARPES) studies were carried out, thanks to which phenomena like band shifts, Fermi surface (FS) modifications, nesting disturbances, and Lifshitz transitions were observed.

The first investigated compound was the iron-based superconductor $\text{FeTe}_{1-y}\text{Se}_y$ ($y \sim 0.35$), in which iron atoms were substituted by transition metals: cobalt and nickel. In the case of this compound, such doping causes suppression of superconducting properties. Transport studies on these samples showed several intriguing phenomena, including a change in the sign of the Hall coefficient, which occurs only below room temperature¹. Significant differences in the attenuation of superconductivity after doping with cobalt or nickel point to different scenarios behind the modification of the transport properties. Previous studies have shown that the lowering of T_c by Co is associated with electron doping, while in the case of Ni, the reason for the rapid decrease of T_c is the strong localization of electrons. The simplest phenomenon we were looking for was the shift of the bands caused by the addition of carriers to the system and the answer to the question of whether these modifications can be understood as a simple shift of the Fermi level, or a more complicated deformation of the bands occurs. Moreover, superconductivity suppression may be related to changes in nesting, i.e. in a situation where two parts of the Fermi surface can be reconstructed by translating with the vector different from the one resulting from the lattice symmetry. All of this made this system extremely interesting from the point of view of the examination of the electron structure.

The second compound was CaFe_2As_2 , in which, unlike $\text{FeTe}_{1-y}\text{Se}_y$, the substitution of cobalt in place of iron improves the superconducting properties². This compound is characterised by a rich phase diagram^{2,3}; the selection of samples located at the phase boundaries allowed for a comprehensive study of the electronic structure. $\text{CaFe}_{2-x}\text{Co}_x\text{As}_2$ exhibits a phase transition between tetragonal, collapsed tetragonal and orthorhombic structures, and it is particularly interesting to compare the electronic structure of each of these phases. These transitions occur depending on the dopant concentration, temperature or applied external pressure. Moreover, spin density waves are observed in the phase of orthorhombic structures further increasing the complexity of the electronic structures present in this compound^{4,5}. The research focused on a nonsuperconducting parent compound, a lightly doped superconductor with a Co concentration corresponding to the appearance of superconductivity in the system, and a heavily doped sample from the antiferromagnetic phase. CaFe_2As_2 is a close "cousin" of the well-studied and very often described in the literature BaFe_2As_2 , but so far the publications on it are much more modest. The original experimental goal guiding us in the study of this compound was to determine the effects of Co doping, band shifts and compare them with the previously

measured $\text{Fe}_{1-x}\text{M}_x\text{Te}_{1-y}\text{Se}_y$, $\text{M}=\text{Co}, \text{Ni}$ in an attempt to search for a universal explanation of the doping mechanism.

The last type of compounds were LaCuSb_2 and LaAgSb_2 . The first one is a superconductor below $T_c = 0.7 \text{ K}$ ⁶, the second one is a superconductor with $T_c = 0.29 \text{ K}$ ⁷ and a charge density wave system having two different modulation vectors⁸. As a result of their practically identical crystal structure, these compounds provide an ideal platform for studying the differences between the two mentioned competing phases.

An additional common feature of the selected compounds is the occurrence of nontrivial topological states. For $\text{FeTe}_{1-y}\text{Se}_y$, there are experimental reports of the observation of Dirac surface states associated with topological superconductivity and Majorana fermions^{9,10}. For the compound BaFe_2As_2 , there are ARPES studies with observations of Dirac cones¹¹ and theoretical predictions about their connections with CDW^{12,13}, however, the occurrence of similar states in CaFe_2As_2 has not yet been demonstrated experimentally. In the case of LaCuSb_2 and LaAgSb_2 , there is both theoretical and experimental evidence that these materials are host to the Dirac fermions and these states are connected with the existence of the Dirac-like structure¹⁴⁻¹⁶. Literature reports suggest that in LaAgSb_2 these states create nested fragments of the Fermi surface, and their modification may be related to the disappearance of superconductivity and the appearance of charge density waves^{8,14}.

All these properties make the study of compounds extremely intriguing from the point of view of the development of solid-state physics and deepening our understanding of the phenomenon of superconductivity and its relationship with other phases of matter.

2. Introduction

2.1. Superconductivity

Superconductors are materials that are characterized by three main phenomena. The first is the complete disappearance of the static electrical resistance below a certain temperature T_c called the critical temperature. The second phenomenon is the Meissner effect, i.e. the removal of the magnetic field from the entire volume of the material except for a thin near-surface layer. The third characteristic feature of a superconductor is the quantization of the magnetic flux value¹⁷. It is easy to imagine the possibilities of such materials in the industry; therefore, the development and research of superconductors have become one of the most important tasks in the field of solid-state physics.

The phenomenon of superconductivity was discovered in 1911 by Heike Kamerlingh Onnes during the measurement of the electrical resistance of mercury¹⁸. Superconducting properties were observed in several elements and more complicated materials in the following decades.

There are several ways to classify superconducting materials. The first is the distinction between type I and type II superconductors. The first of them passes to the normal state in the presence of an external magnetic field, called a critical field. For type II superconductors, there are two values of the critical field. Above the first, the magnetic field enters the volume of the material in the form of vortices. Above the second value of the critical field, the superconducting state disappears¹⁷. The description of these phenomena was developed phenomenologically by Ginzburg and Landau in 1950¹⁹.

Another way to classify superconductors is a division according to the theory describing the superconducting state. There are conventional and unconventional superconductors. The mechanism of conventional superconductivity was explained by J. Bardeen, L. Cooper, and J. R. Schrieffer, and their theory was named BCS after their names. The basic idea of BCS theory is the concept of the pairing of electrons. That pairing occurs through interaction mediated by phonons and results in forming a phase that can move and so conduct electricity without energy dissipation. Such pairs of electrons are called Cooper pairs. Materials in which superconductivity goes beyond the description of the BCS theory are called unconventional. The explanation of the mechanism responsible for unconventional superconductivity is probably the most discussed and most controversial issue in physics. One of the proposed interactions is based on antiferromagnetic spin fluctuation²⁰.

Another popular classification considers the superconducting transition temperature. There are low-temperature superconductors with a superconducting transition temperature below the boiling point of liquid nitrogen (77 K), and high-temperature superconductors with a superconducting transition temperature above the boiling point of liquid nitrogen. The timeline of the discovery of new superconductors and their critical temperatures is shown in Figure 2.1.

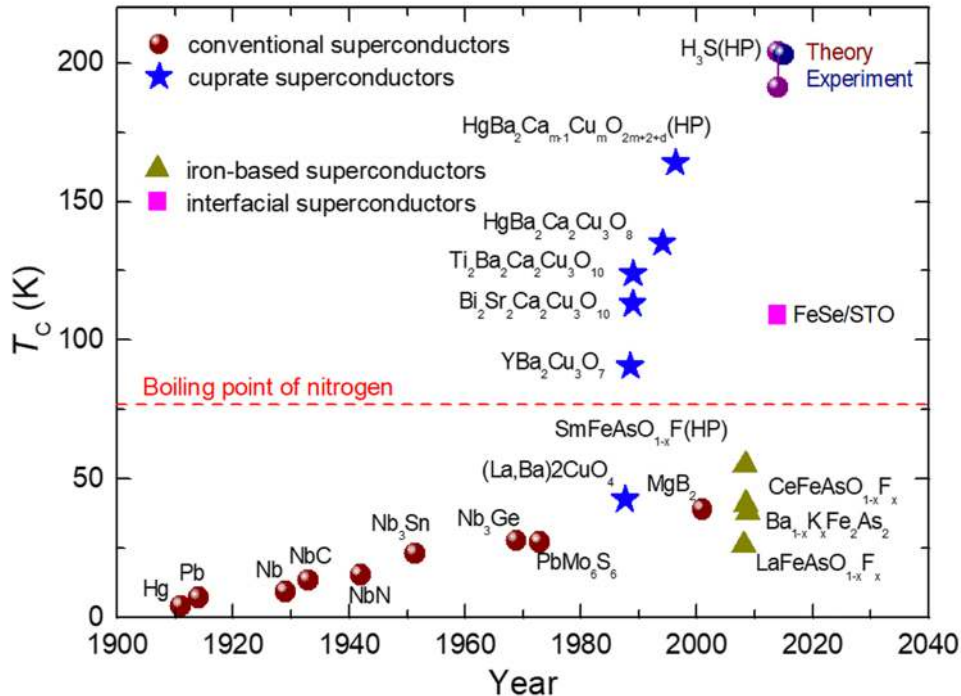


Figure 2.1. Evolution of high-temperature superconductivity over time. Taken from Ref. 21.

The last way to classify superconductors relates to their structure and chemical composition. Superconductivity is observed in some pure elements (e.g. mercury, lead, niobium, vanadium, and others), alloys (e.g. NbTi), and ceramics like layered materials, consisting of layers of copper oxide (cuprates) or layers of iron (so-called iron-based superconductors).

The discovery of superconductivity in cuprates by Johannes Georg Bednorz and K. Alex Müller in 1986²² was one of the most important milestones in the history of condensed matter physics. The compound they discovered, lanthanum barium copper oxide (LBCO), reached a superconducting state at a temperature of 35 K, which exceeds the upper limit imposed by the BCS theory. Cuprates are layered materials, and their common features are superconducting layers of copper oxide and other layers that contain ions such as lanthanum, barium, or strontium. In this class of materials, it was possible to achieve critical temperatures exceeding 100 K, which significantly facilitated the practical use of superconductors.

The next important step in the development of superconductors, and one of the greatest achievements of solid physics in the recent years, was the discovery of superconductivity in iron-based materials. These superconductors contain layers of iron and a p-block element, usually arsenic or phosphorus, or a chalcogen. The first known iron-based superconductor is LaOFeP with a critical temperature of about 4 K²³. So far, the highest critical temperature has been obtained in single-layer FeSe films doped with SrTiO₃ and was above 100 K²⁴.

2.1.1. London's Theory and Meissner Effect

The first successful attempt at a theoretical description of superconductivity was proposed in 1935 by Fritz and Heinz London. The basis of this theory is the assumption that Maxwell's laws are universal and must be satisfied in superconducting substances. Electrons in a superconductor behave differently from Ohm's law, so another relationship must be found to explain the Meissner effect. As a result, it was possible to formulate a description of the penetration depth of the superconductor by the magnetic field, explain the occurrence of the phenomenon of decay of electrical resistance and decay of the magnetic field.

The theory is based on the division of electrons involved in electrical conductivity into two groups: those subject to scattering on the ions of the crystal lattice and those that are not subject to scattering, and thus responsible for superconductivity. They then postulated that the current density \vec{j} in the superconducting state is directly proportional to the magnetic vector potential \vec{A} and depends on the number of electrons in the superconducting state n_s , the electron mass m_e , and the electron charge e :

$$\vec{j} = -\frac{n_s e^2}{m_e} \vec{A} = -\frac{1}{\mu_0 \lambda_L^2} \vec{A}, \quad (2.1)$$

where λ_L is a constant. The vector potential \vec{A} has the London gauge: $\vec{\nabla} \cdot \vec{A} = 0$ and $\vec{A}_n = 0$ (n is the surface normal) for any external surface through which no current flows into the superconductor. The boundary conditions are as follows: $\vec{\nabla} \cdot \vec{j} = 0$ i $j_n = 0$. The equation (2.1) is correct for simple sample shapes, in the case of a ring or cylinder, additional terms will appear. If we consider, formula (2.1) in the Ampere equation for a constant field strength \vec{E} we get:

$$e\vec{\nabla} \times \vec{B} = \mu_0 \vec{j} = -\frac{1}{\lambda_L^2} \vec{A}. \quad (2.2)$$

Then, the rotations of both sides of the equation are calculated, and using the relationship $\vec{\nabla} \times (\vec{\nabla} \times \vec{a}) = \vec{\nabla}(\vec{\nabla} \cdot \vec{a}) - \vec{\nabla}^2 \vec{a}$, and Gauss's law for magnetism $\vec{\nabla} \cdot \vec{B} = 0$ we get:

$$\vec{\nabla}^2 \vec{B} = \frac{1}{\lambda_L^2} \vec{B}, \quad (2.3)$$

This equation describes the Meissner effect. The constant value of the field $\vec{B}(\vec{r}) = B_0 = \text{const}$ is its solution only when $B_0 = 0$. If we substitute $B_0 = 0$ into equation (2.2) we get $\vec{j} = 0$. This means that the zero value of the magnetic field induction inside the superconductor is associated with the disappearance of the current. The internal field is shielded by currents that flow near the surface of the superconductor. A schematic representation of the Meissner effect is shown in the Figure 2.2

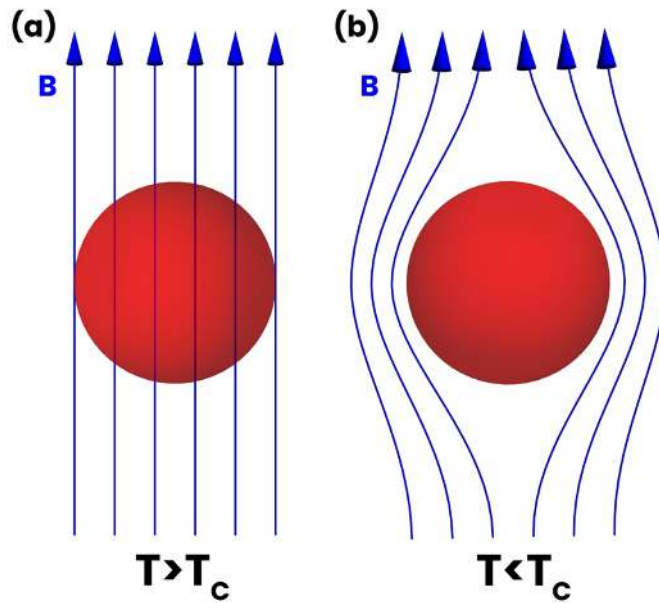


Figure 2.2. Diagram of the Meissner effect. (a) Material in the normal state, (b) superconductor with magnetic field lines are excluded from the bulk.

Consider a superconductor whose magnetic field near its surface is $\vec{B}(0)$. Inside such material we have:

$$B(x) = B(0)e^{-\frac{x}{\lambda_L}}, \quad (2.4)$$

where x is the distance from the edge of the sample. It follows that the parameter λ_L determines the depth of penetration of the magnetic field induction into the interior of the superconductor. This is called the London Penetration Depth. For carriers with charge q , mass m , and concentration n , the London depth of derivation is given by:

$$\lambda_L = \sqrt{\frac{\epsilon_0 m c^2}{n q^2}}. \quad (2.5)$$

2.1.2. BCS Theory

The Bardeen-Cooper-Schrieffer (BCS) theory is a theoretical model of superconductivity that was developed in the 1950s²⁵. It is a fundamental concept in the field of superconductivity and provides a theoretical framework for understanding the properties of conventional superconductors and for studying the mechanisms of superconductivity in other materials. The phenomenon of superconductivity is explained as a result of the formation of pairs of electrons, called Cooper pairs. The total wave vector of the electron forming pair is zero, so it can be written symbolically as $+\mathbf{k} \uparrow$ and $-\mathbf{k} \downarrow$. The Feynman diagram corresponding to the interaction of two electrons via a phonon is shown in Figure 2.3. The electrons in a pair interact with each other through vibrations of phonons.

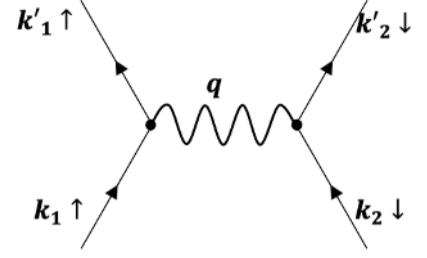


Figure 2.3. Feynman diagram corresponding to the interaction of two electrons via a phonon.

The initial Hamiltonian \mathcal{H} of a single Cooper pair in the second quantization formalism has the following form:

$$\mathcal{H} = \sum_{\mathbf{k}\sigma} \epsilon_{\mathbf{k}} a_{\mathbf{k}\sigma}^{\dagger} a_{\mathbf{k}\sigma} - V \sum_{\mathbf{k}\mathbf{k}'} a_{\mathbf{k}\uparrow}^{\dagger} a_{-\mathbf{k}\downarrow}^{\dagger} a_{-\mathbf{k}'\uparrow} a_{\mathbf{k}'\downarrow}, \quad (2.6)$$

Where a^{\dagger} and a are the creation and annihilation operators, respectively. For an electron gas, a variable number of particles is taken into account (so the term is included: $-\mu N_e \equiv -\mu \sum_{\mathbf{k}\sigma} a_{\mathbf{k}\sigma}^{\dagger} a_{\mathbf{k}\sigma}$ where μ is chemical potential), and the Hamiltonian is taken in the following form:

$$\mathcal{H}_{BCS} = \sum_{\mathbf{k}\sigma} (\epsilon_{\mathbf{k}} - \mu) a_{\mathbf{k}\sigma}^{\dagger} a_{\mathbf{k}\sigma} - \sum_{\mathbf{k}\mathbf{k}'} V_{\mathbf{k}\mathbf{k}'} a_{\mathbf{k}\uparrow}^{\dagger} a_{-\mathbf{k}\downarrow}^{\dagger} a_{-\mathbf{k}'\uparrow} a_{\mathbf{k}'\downarrow}, \quad (2.7)$$

The first term of \mathcal{H} describes the kinetic energy of the system, and the second describes the scattering of an electron from the state $+\mathbf{k} \uparrow$ to the state $-\mathbf{k} \downarrow$. V describes the interaction between particles. Only electrons from the energy range $(E_F, E_F + \hbar\omega_D)$, where E_F is Fermi energy and ω_D is Debye frequency, interact with phonons which leads to the formation of an attractive interaction, and it is non-zero and constant near the Fermi surface:

$$V_{\mathbf{k}\mathbf{k}'} = \begin{cases} -V & \text{for } k_F - \Delta k_F \leq k, k' \leq k_F + \Delta k_F \\ 0 & \text{otherwise} \end{cases}. \quad (2.8)$$

$V > 0$, corresponds to the attraction of electrons, which causes a gap in the energy spectrum and is associated with the formation of pairs.

Using mean-field decoupling of the quartic term:

$$a_{\mathbf{k}\uparrow}^{\dagger} a_{-\mathbf{k}\downarrow}^{\dagger} a_{-\mathbf{k}'\downarrow} a_{\mathbf{k}'\uparrow} \cong \langle a_{\mathbf{k}\uparrow}^{\dagger} a_{-\mathbf{k}\downarrow}^{\dagger} \rangle a_{-\mathbf{k}'\downarrow} a_{\mathbf{k}'\uparrow} + \langle a_{-\mathbf{k}'\downarrow} a_{\mathbf{k}'\uparrow} \rangle a_{\mathbf{k}\uparrow}^{\dagger} a_{-\mathbf{k}\downarrow}^{\dagger} - \langle a_{\mathbf{k}\uparrow}^{\dagger} a_{-\mathbf{k}\downarrow}^{\dagger} \rangle \langle a_{-\mathbf{k}'\downarrow} a_{\mathbf{k}'\uparrow} \rangle, \quad (2.9)$$

and defining terms:

$$\Delta_{\mathbf{k}} \equiv \sum_{\mathbf{k}'} V_{\mathbf{k}\mathbf{k}'} \langle a_{-\mathbf{k}'\downarrow} a_{\mathbf{k}'\uparrow} \rangle \quad (2.10)$$

$$\Delta_{\mathbf{k}}^* \equiv \sum_{\mathbf{k}'} V_{\mathbf{k}\mathbf{k}'} \langle a_{\mathbf{k}\downarrow}^\dagger a_{-\mathbf{k}\uparrow}^\dagger \rangle \quad (2.11)$$

we get an effective BCS Hamiltonian:

$$\begin{aligned} \mathcal{H}_{BCS} = & \sum_{\mathbf{k}\sigma} (\epsilon_{\mathbf{k}} - \mu) n_{\mathbf{k}\sigma} + \sum_{\mathbf{k}} (\Delta_{\mathbf{k}} a_{\mathbf{k}\uparrow}^\dagger a_{-\mathbf{k}\uparrow}^\dagger + \Delta_{\mathbf{k}}^* a_{-\mathbf{k}\downarrow} a_{\mathbf{k}\downarrow}) \\ & - \sum_{\mathbf{k}'\mathbf{k}} V_{\mathbf{k}\mathbf{k}'} \langle a_{\mathbf{k}'\uparrow}^\dagger a_{-\mathbf{k}'\downarrow}^\dagger \rangle \langle a_{-\mathbf{k}'\downarrow} a_{\mathbf{k}'\uparrow} \rangle \end{aligned} \quad (2.12)$$

This Hamiltonian can be made diagonalizable by applying the Bogoliubov transformation:

$$\begin{cases} a_{\mathbf{k}\uparrow} = u_{\mathbf{k}} \alpha_{\mathbf{k}} - v_{\mathbf{k}} \beta_{\mathbf{k}}^\dagger \\ a_{-\mathbf{k}\uparrow}^\dagger = v_{\mathbf{k}} \alpha_{\mathbf{k}} + u_{\mathbf{k}} \beta_{\mathbf{k}}^\dagger \end{cases} \quad (2.13)$$

Where:

$$\begin{cases} u_{\mathbf{k}} = \frac{1}{\sqrt{2}} \left(1 + \frac{\epsilon_{\mathbf{k}}}{E_{\mathbf{k}}} \right)^{1/2} \\ v_{\mathbf{k}} = \frac{1}{\sqrt{2}} \left(1 - \frac{\epsilon_{\mathbf{k}}}{E_{\mathbf{k}}} \right)^{1/2} \end{cases} \quad (2.14)$$

The equation for delta Δ has the following form:

$$\Delta = -V \sum_{\mathbf{k}} \langle a_{-\mathbf{k}\downarrow} a_{\mathbf{k}\uparrow} \rangle = -V \sum_{\mathbf{k}} u_{\mathbf{k}} v_{\mathbf{k}} [\langle \alpha_{\mathbf{k}}^\dagger \alpha_{\mathbf{k}} \rangle + \langle \beta_{\mathbf{k}}^\dagger \beta_{\mathbf{k}} \rangle + 1] \quad (2.15)$$

Which can be rewritten as:

$$\Delta = \frac{1}{2} V \sum_{\mathbf{k}} \left(1 - \frac{\epsilon_{\mathbf{k}}^2}{E_{\mathbf{k}}^2} \right)^{1/2} (1 - 2) \langle a_{\mathbf{k}}^\dagger a_{\mathbf{k}} \rangle \quad (2.16)$$

Using the fact that states are subject to the Fermi-Dirac statistic, we get:

$$\Delta = V \Delta \sum_{\mathbf{k}} \frac{1}{2E_{\mathbf{k}}} \operatorname{tgh} \left(\frac{E_{\mathbf{k}}}{2k_B T} \right) \quad (2.17)$$

This equation has two solutions:

$$\Delta \equiv 0, \quad (2.18)$$

and:

$$1 = V \sum_{\mathbf{k}} \frac{1}{2E_{\mathbf{k}}} \tanh\left(\frac{E_{\mathbf{k}}}{2k_B T}\right). \quad (2.19)$$

The first one is trivial and corresponds to the normal state. The second one could be used to estimate the value of the superconducting gap. The derivation of this relationship is one of the most important achievements of the theory:

$$\Delta \cong \frac{2\hbar\omega_D}{\exp\left(\frac{1}{N(0)V}\right)}. \quad (2.20)$$

$N(0)$ is the density of states at the Fermi level. The second important achievement is a relation between the superconducting transition temperature (T_c) and the density of states at the Fermi level. T_c is inversely proportional to the strength of the attractive interaction between electrons:

$$T_c = 1.14 \frac{\hbar\omega_d}{k_B} \exp\left(-\frac{1}{V N(0)}\right), \quad (2.21)$$

This means that the higher the density of states at the Fermi level and the weaker the attractive interaction between electrons, the higher the T_c .

The BCS theory was able to explain the main properties of conventional superconductors, such as lead and mercury, and is still used today to understand the properties of these materials. However, it cannot explain high T_c superconductors, with T_c typically higher than 30 K.

2.1.3. Superconductivity in Iron Pnictides and Chalcogenides

Superconductivity in iron-based pnictides and chalcogenides was discovered in 2006 in layered oxy-pnictide $\text{LaOFeP}^{23,26}$. In these compounds, superconductivity is based on conductive iron layers and pnictides (elements in group 15 of the periodic table) or chalcogens (group 16)²⁷.

A widely used method of classifying iron-based superconductors is related to their crystal structure. Many so-called families have been distinguished, for example, '11', '111', '122', '1111', with these names referring to their stoichiometry²⁸. All iron-based pnictides and chalcogenides have a similar structure with characteristic Fe-pnictogen or Fe-chalcogen layers. Each layer is composed of Fe ions that form a square lattice, and the rest of the atoms are located above or below the centre of a square pattern.

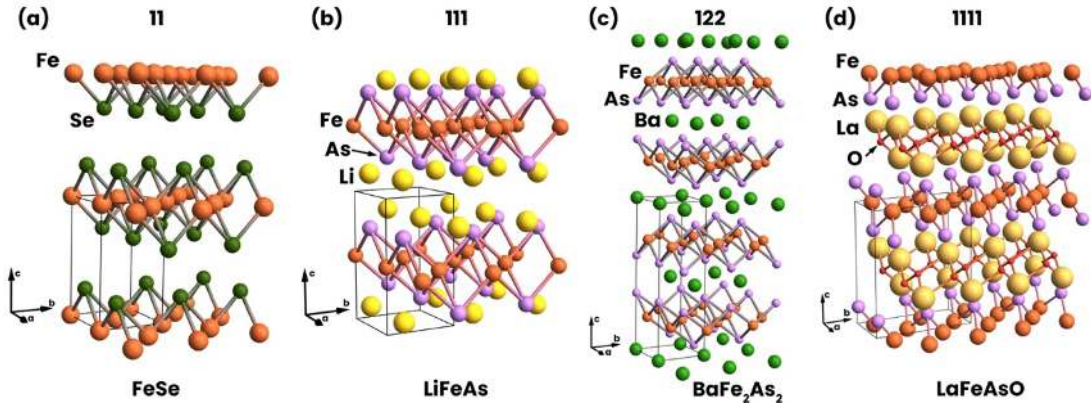


Figure 2.4. Crystal structure of selected families of iron superconductors: (a) ‘11’, (b) ‘111’, (c) ‘122’, (d) ‘1111’.

The electronic structure of most of these materials is made up of multiple bands that crossed the Fermi level and formed quasi-2d hole pockets in the middle of the Brillouin zone and electron pockets at the boundaries of the Brillouin zone^{28,29}. A schematic example of the Fermi surface of a typical iron-based superconductor is shown in the Figure 2.5.

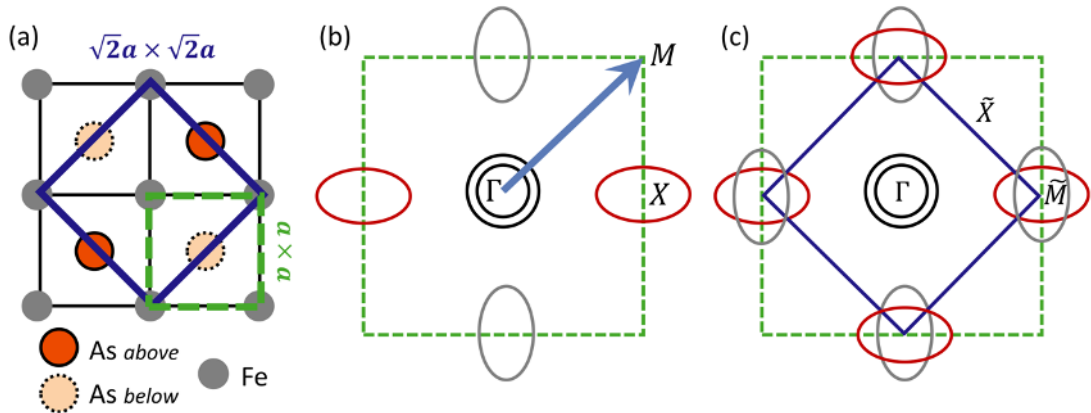


Figure 2.5. (a) Square FeAs lattice and (b,c) example of Fermi surface of iron-based superconductors. The difference between the presented fermi surfaces results from different ways of defining a unit cell, (b) 1-Fe BZ with boundaries indicated by a green dashed square, (c) 2-Fe folded BZ with boundaries shown by a solid blue square. Taken from Ref. 30.

The properties of iron-based compounds change dramatically with doping, so studying their phase diagrams was a subject of intensive research. One of the most interesting iron-based superconductors is $\text{Fe}_{1+y}\text{Te}_{1-x}\text{Se}_x$ with a transition temperature of about 14 K. Its phase diagram starts with the magnetic order for a low dopant (Se) level and ends with a superconductivity dome. An interesting fact is that inducing superconductivity by substituting Se for Te occurs even though the elements are isovalent, and the hole/electron concentration in the system does not change. The situation is different in the case of substituting iron with transition metals with higher

number of valence electrons; this causes an increase in the concentration of electrons and the disappearance of superconductivity. The electronic structure of $\text{Fe}_{1+y}\text{Te}_{1-x}\text{Se}_x$ has been extensively studied by various techniques. It is known that for an optimal doping level, the Fermi surface consists of two hole pockets around the Γ point and two electron pockets around the M point²⁸. Replacing the iron atoms in such a way as to add extra electrons to the system (e.g. by using cobalt or nickel atoms) reduces the surface of the hole pockets and increases the size of the electron pockets³¹. However, the observed changes in the size of the electron and hole pockets are not consistent with the rigid band model, which assumes that modification of the electronic structure can be understood as a simple shift of the chemical potential³¹.

This compound is of particular interest in the $\text{FeTe}_{0.5}\text{Se}_{0.5}$ stoichiometry because of the observation of the topological spin-helical Dirac surface states proximity coupled to bulk *s*-wave superconductivity^{10,32,33}.

Another popular family of iron superconductors is 122. A typical phase diagram of system 122 (e.g., BaFe_2As_2 or CaFe_2As_2 compounds) starts with the antiferromagnetic phase. By replacing the alkaline earth metal (Ba), pnictogen (As), transition metal (Fe) with the appropriate atoms, the antiferromagnetic non-superconducting phase disappears and the non-magnetic state of the superconductor is created^{2,34-36}. A schematic representation of phase diagram of 122 family is shown in the Figure 2.6. In the case of these compounds, a structural transition from the orthorhombic to the tetragonal phase due to doping is also observed^{2,37,38}. The electronic structure of 122 compounds in the superconducting phase is analogous to the rest of iron-based superconductors, but there are significant differences in the antiferromagnetic phase, for which spin density waves (SDW) are observed. In the case of BaFe_2As_2 or CaFe_2As_2 compounds in the SDW phase, the Fermi surface is formed from petal-shaped pockets and the size of the BZ is reduced. The doping of these compounds may cause two basic effects on the electronic structure; the first is related to the phase transition and is observed as the disappearance of the petal-like structure and the appearance of concentric pockets. The second effect is the shift of the binding energy of the bands. Such shifts may lead to the disappearance or the appearance of pockets on the Fermi surface, a phenomenon that can be treated as a discontinuous change of its topology. It is called the Lifshitz phase transition³⁹.

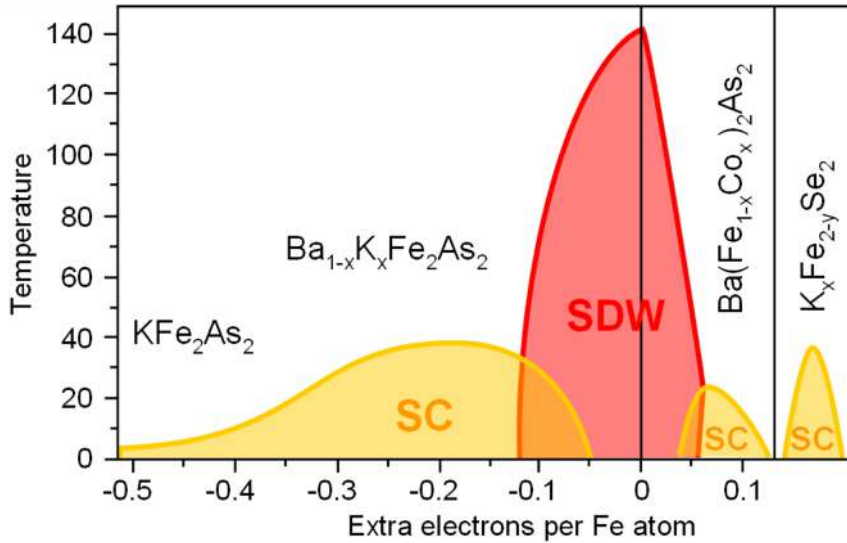


Figure 2.6. A schematic phase diagram of 122 family. Taken from Ref. 40.

2.1.4. Topological Superconductivity

In a classic superconductor, Cooper pairs are formed by conduction electrons with spin directed both up and down. The discovery of three-dimensional topological insulators gave rise to theoretical proposals for the development of this concept. In these materials, an energy gap is observed for the electronic volume states, whereas the surface states appear as an odd number of Dirac cones in which the spin of electrons at the Fermi surface is fixed. It follows that electrons moving in each direction will only have one spin direction, therefore pairing is only possible with electrons with the opposite spin. This is the main idea behind topological superconductivity and results in several non-trivial consequences. Unlike the topological insulator, where the surface states consist of electrons, the surface states in a topological superconductor are made up of Majorana fermions, or particles that are their own antiparticles⁴¹. Moreover, it is predicted that there are some quantum phase transitions related to topological superconductivity, which may result in the quantized of supersymmetry in condensed matter⁴².

2.2. Topological Materials

In recent years, the study of a topological material of the electronic structure (or materials with non-trivial topology, depending on the naming convention) has become one of the most popular topics in solid-state physics. The history of research on these materials starts with the quantum Hall effect and develops the huge set of systems that includes topological insulators, different types of topological semi-metals, or topological superconductors^{43–45}. The schematic timeline of the development of topological materials is shown in Figure 2.7.

It is worth starting any description of the concept of topological materials with the term topology. In a very basic approach, it is a branch of mathematics that studies properties that do not change even after radically deformed objects. There is a classic example that is used to explain this concept. Let's imagine the transformation of a torus

into a mug of coffee. Both the torus and the cup have one ‘hole’, so such a transformation is continuous. We can say that these two objects are homeomorphic, they have identical topological properties, and in the matter of the topology, they are the same. On the contrary, transformation from a sphere to the torus requires creating an additional ‘hole’ so that the sphere is not homeomorphic to the torus. In other words, the two objects are ‘topologically equivalent’ if they can be smoothly transformed into each other. In the case of the topological materials, the topological transformation refers to the mapping from the crystal momentum \mathbf{k} to the Bloch Hamiltonian. These operations are associated with topological invariants that cannot change when the Hamiltonian varies smoothly^{43,46}.

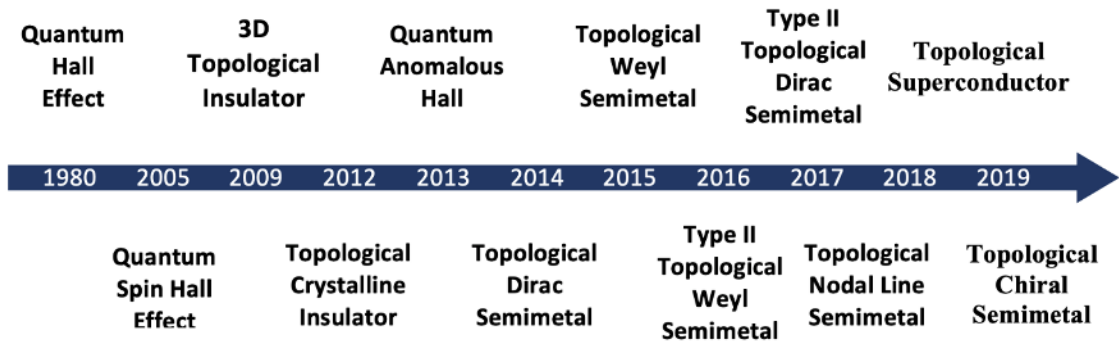


Figure 2.7. Timeline of the Development of Topological Materials.

The difference between ordinary states of matter and topological materials was explained by the concept of a topological invariant. The two-dimensional band structure could be mapped into the Bloch Hamiltonian. The equivalence of the classes of Hamiltonian could be used to classify the gapped band structure. The topological invariant, called Chern number: $n \in \mathbb{Z}$ (\mathbb{Z} - integers), is used to distinguish these classes. The physical meaning of this invariant is related to the Berry phase. The Bloch wave function $|u_m(\mathbf{k})\rangle$ appears with a well-defined Berry phase when \mathbf{k} moves around the closed loop and that Berry phase is given by $\mathcal{A}_m = i\langle u_m | \nabla_{\mathbf{k}} | u_m \rangle$, which can be written as a surface integral of the Berry flux $\mathcal{F}_m = \nabla \times \mathcal{A}_m$. The total Berry flux in the Brillouin zone:

$$n_m = \frac{1}{2\pi} \int d^2\mathbf{k} \mathcal{F}_m, \quad (2.22)$$

is the Chern number. This quantity is the key to defining the material topology; materials with nonzero Berry curvature exhibit properties nontrivially topologically⁴⁷. The importance of the Chern number can be demonstrated by considering the Dirac equations or by the example of the simplest of the topological phases, a two-dimensional free electron gas, showing the quantum Hall effect.

2.2.1. Dirac Equation

From the point of view of mathematical description, the key to explaining topological materials is the Dirac equation⁴⁸. It describes a relativistic quantum mechanical wave function of the particle with spin $\frac{1}{2}$:

$$H = c\mathbf{p} \cdot \boldsymbol{\alpha} + mc^2\beta, \quad (2.23)$$

where m is the mass of the particle, c is the speed of light, $\boldsymbol{\alpha}$ and β are at least 2×2 Dirac matrices. Examples of such matrices are Pauli matrices:

$$\sigma_x = \begin{pmatrix} 0 & 1 \\ 1 & 0 \end{pmatrix}, \sigma_y = \begin{pmatrix} 0 & -i \\ i & 0 \end{pmatrix}, \sigma_z = \begin{pmatrix} 1 & 0 \\ 0 & -1 \end{pmatrix}. \quad (2.24)$$

The solution of the Dirac equation depends on the dimensionality of the problem. In one dimension, any two of the Pauli matrices could be Dirac matrices. In two dimensions, all three Pauli matrices are Dirac matrices. In three dimensions, four Dirac matrices are at least four-dimensional and could be expressed using Pauli matrices:

$$\alpha_i = \begin{pmatrix} 0 & \sigma_x \\ \sigma_x & 0 \end{pmatrix} \equiv \sigma_x \otimes \sigma_i, \quad (2.25)$$

$$\beta = \begin{pmatrix} \sigma_0 & 0 \\ 0 & -\sigma_0 \end{pmatrix} \equiv \sigma_z \otimes \sigma_0, \quad (2.26)$$

where σ_0 is the identity matrix.

In that way, the relativistic energy-momentum relation is a solution of the following equation:

$$E^2 = m^2c^4 + p^2c^2, \quad (2.27)$$

and in the three-dimensional case there are two solutions for positive and negative energy:

$$E_{\pm} = \pm\sqrt{m^2c^4 + p^2c^2}. \quad (2.28)$$

The two positive solutions of the above equation are used to describe the motion of the electron with spin, one for the state with the spin-up and the second for the spin-down. A negative solution refers to the electron's antiparticle, the positron. However, this formalism can also be used to introduce the concept of a hole in a solid. The absence of an electron (with negative mass and kinetic energy) could be understood as a particle with positive mass and positive energy.

To find the description of the topological insulator using the Dirac equation, let's introduce the quadratic correction $-Bp^2$:

$$H = c\mathbf{p} \cdot \boldsymbol{\alpha} + (mv^2 - Bp^2)\beta, \quad (2.29)$$

The v is an effective velocity and is used to replace c as I am considering the solids, mv^2 is the band gap of the particle. This term makes this equation topologically distinct from the original Dirac equation due to breaking the symmetry between positive and negative masses.

Let's consider one-dimensional case. Equation (2.29) could be written in the form:

$$h(x) = vp_x\sigma_x + (mv^2 - Bp_x^2)\sigma_z, \quad (2.30)$$

where mv^2 is a band gap. For the bound state with zero energy, the eigenvalue equation takes the form:

$$[vp_x\sigma_x + (mv^2 - Bp_x^2)\sigma_z]\varphi(x) = 0 \quad (2.31)$$

Its solution, assuming that the wave function must vanish for $x = 0$ and $x = +\infty$, takes the form:

$$\varphi_\eta(x) = \frac{c}{\sqrt{2}} \begin{pmatrix} \text{sgn}(B) \\ i \end{pmatrix} \left(\exp\left(-\frac{x}{\xi_+}\right) - \exp\left(-\frac{x}{\xi_-}\right) \right), \quad (2.32)$$

where $\xi_{\pm}^{-1} = \frac{v}{2|B|\hbar}(1 - 4mB)$, C is normalization constant. The wave function described by this solution is distributed dominantly near the boundary and decays exponentially. Parameters ξ_{\pm} characterize end state, when $B \rightarrow 0$, $\xi_+ \rightarrow |B|\hbar/v$ and $\xi_- = \hbar/mv$ so the ξ_+ approaches to zero and ξ_- is determined by the energy gap. When $m \rightarrow 0$, $\xi_- = +\infty$ so the state evolves into bulk state, the end state disappears, and a topological phase transition takes places for $m = 0$.

The full solution of (2.29) takes the following form:

$$\psi_1 = \frac{c}{\sqrt{2}} \begin{pmatrix} \text{sgn}(B) \\ 0 \\ 0 \\ i \end{pmatrix} \left(\exp\left(-\frac{x}{\xi_+}\right) - \exp\left(-\frac{x}{\xi_-}\right) \right), \quad (2.33)$$

and

$$\psi_2 = \frac{c}{\sqrt{2}} \begin{pmatrix} 0 \\ \text{sgn}(B) \\ i \\ 0 \end{pmatrix} \left(\exp\left(-\frac{x}{\xi_+}\right) - \exp\left(-\frac{x}{\xi_-}\right) \right), \quad (2.34)$$

Solutions for higher dimensions, for the edge and surface states, are closely related to this solution.

In two dimensions (2.29) the equation has the following form:

$$h_{\pm} = vp_x\sigma_x \pm vp_y\sigma_y + (mv^2 - Bp^2)\sigma_z, \quad (2.35)$$

This equation breaks the time-reversal symmetry under the transformations under the following transformation: $\sigma_i \rightarrow -\sigma_i$ and $p_i \rightarrow -p_i$. Its solutions:

$$\psi_1 = \frac{c}{\sqrt{2}} \begin{pmatrix} \text{sgn}(B) \\ 0 \\ 0 \\ i \end{pmatrix} \left(\exp\left(-\frac{x}{\xi_+}\right) - \exp\left(-\frac{x}{\xi_-}\right) \right) \exp\left(\frac{ip_y y}{\hbar}\right), \quad (2.36)$$

And

$$\psi_2 = \frac{c}{\sqrt{2}} \begin{pmatrix} 0 \\ \text{sgn}(B) \\ i \\ 0 \end{pmatrix} \left(\exp\left(-\frac{x}{\xi_+}\right) - \exp\left(-\frac{x}{\xi_-}\right) \right) \exp\left(\frac{ip_y y}{\hbar}\right), \quad (2.37)$$

The dispersion relation takes the linear form:

$$\epsilon_{p_y} = \pm vp_y \text{sgn}(B) \quad (2.38)$$

To distinguish between a topologically trivial and a nontrivial system in two dimensions, we could use the Chern number. For a two-band Hamiltonian in the form $H = \mathbf{d}(p) \cdot \sigma$ the Chern number is expressed as:

$$n_c = -\frac{1}{4\pi} \int d\mathbf{p} \frac{\mathbf{d} \cdot (\partial_{p_x} \mathbf{d} \times \partial_{p_y} \mathbf{d})}{d^3}, \quad (2.39)$$

where $d^2 = \sum_{\alpha=x,y,z} d_\alpha^2$. For (1.13), the Chern number takes the form:

$$n_\pm = \pm \frac{1}{2} (\text{sgn}(m) + \text{sgn}(B)). \quad (2.40)$$

Therefore, when m and B have the same sign, the system is topologically non-trivial, and when the signs are different, $n_\pm = 0$.

The way of thinking in the case of three dimensions is analogous and leads to the description of surface states.

2.2.2. Quantum Hall Effect

The first known system in which a nontrivial topology was observed was a two-dimensional electron gas in a strong magnetic field and very low temperature known as the quantum Hall effect⁴⁴. A characteristic feature of the quantum Hall systems is quantized conductivity:

$$\sigma_{xy} = \frac{Ne^2}{h}. \quad (2.41)$$

It has been shown⁴⁹ that σ_{xy} calculated with Kubo formula, has the same form so the N is identical as the Chern number in (2.22). Hence, the quantized value of the Hall conductance relates to the topological invariant, which is related to Berry's phase and is equal to the Berry phase divided by 2π . In a simplified way, we can assume that this invariant is analogous to the number of topologically different closed curves that exist on a certain manifold. It is insensitive to smooth changes in systems Hamiltonian (like material parameters) which explains the lack of influence of the experimental conditions on the quantised conductivity values. The invariant could change only when the system passes through a quantum phase transition, and it is understood as a change in topology.

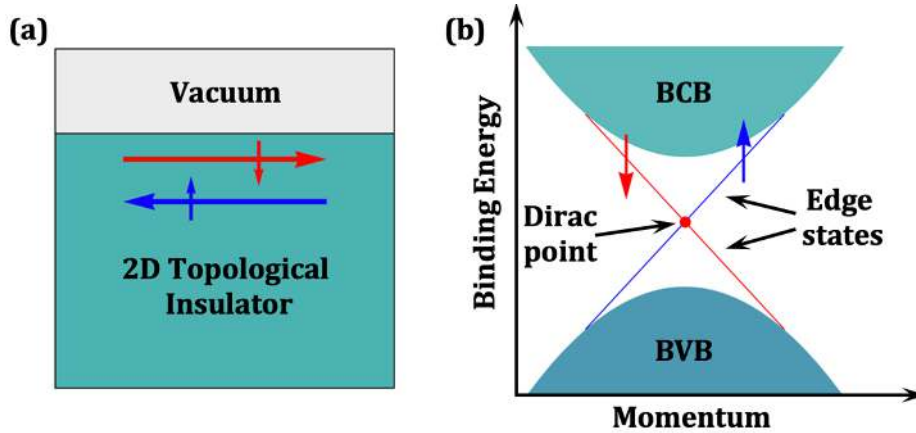


Figure 2.8. (a) Schematic real space diagram of the 2D topological insulator with spin-polarized edge and surface states at the system boundary, (b) energy band diagram of the 2D topological insulator in momentum space. BCB: bulk conduction band, BVB: bulk valence band.

The consequence of the existence of a nontrivial topology is the existence of one-dimensional conducting boundary edge states surrounding the entire sample (Figure 2.8 (a)). The non-trivial edge states cross each other at the so-called Dirac point (Figure 2.8 (b)). These states are insensitive to scattering on impurities and defects in the crystal^{43,46,50}.

2.2.3. Topological Insulators

Topological insulators are the materials that are bulk insulators but have spin-degenerate conductive states on the surface (shown schematically in Figure 2.9 (a)) and are robust to any type of defect or disorder. Three-dimension topological insulators are characterised by the topological invariant called Z_2 , which is based on parity. This concept can be explained using Kramer's theory for spins $\frac{1}{2}$ electrons. The energy of two bands with the same $|k|$ is the same because of the time-reversal symmetry. Such a pair of bands is called a Kramer pair. These pairs are degenerate at certain points in the Brillouin zone. The value of the invariant Z could be determined by counting how often surface states cross the Fermi energy between two degenerate points. For an odd number of intersections $Z_2 = 1$, for an even number $Z_2 = 0$ ⁴⁶. If the value is equal to 1 the phase is nontrivial, while 0 indicates trivial topology. The nature of the surface state of the topological insulator is a consequence of the boundary conditions that arise as a result of the combination of the nontrivial bulk states and the vacuum, which is a trivial insulator. In the described situation, the topology changes from non-trivial to trivial. The topological invariant changes at the interface, and the energy gap closes, so the metallic surface states appear. Therefore, it follows that in topological insulators, surface gaps must always be present.

The characteristic feature of the surface states observed in topological insulators is spin degeneracy. This creates separate channels for the up and down spins whose momenta are locked in a manner that maintains symmetry with the time-reversal. The consequence of this behaviour is the formation of the gapless Dirac cone with linear dispersion and helical spin texture (Figure 2.9 (b))^{47,51}. The existence of a spin-degenerate cone results in a non-trivial Berry phase equal to π . This value is intuitively easy to understand because the electrons that create the Dirac state follow a closed path around the Dirac point.

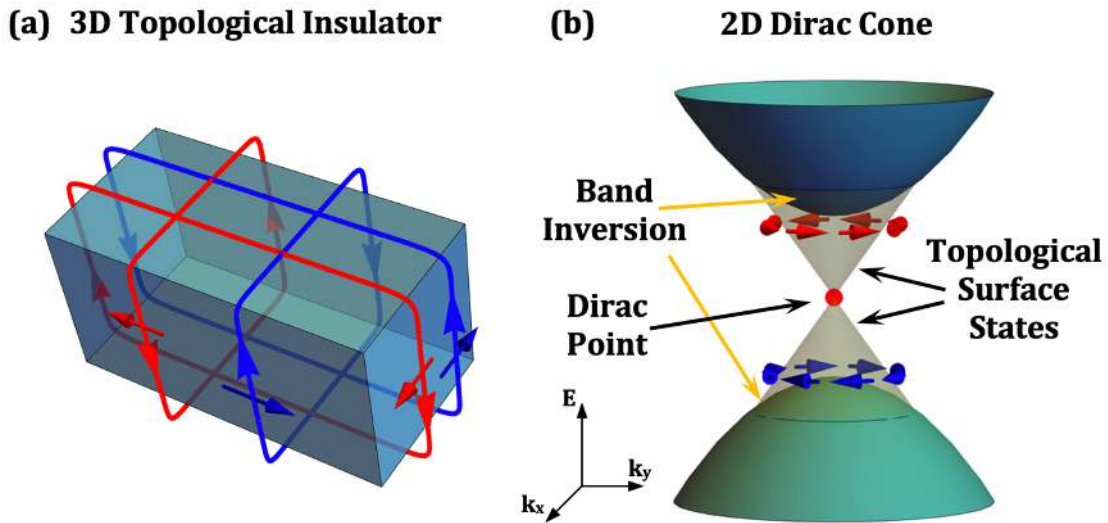


Figure 2.9. (a) Schematic real space diagram of 3D topological insulators with spin-polarized surface states at the system boundary. (b) Energy band diagram of the 3D topological insulator in momentum space, showing the formation of a 2D Dirac cone.

The first three-dimensional topological insulator to be realized experimentally was $\text{Bi}_{1-x}\text{Sb}_x$ ⁵². To date, such behavior has been observed in various systems such as binary V2-VI3 compounds (Bi_2Te_3 ⁵², Bi_2Se_3 ⁵³ and Sb_2Te_3 ⁵⁴ or the ternary III-V-VI₂ family of compounds (e.g., TlBiTe_2 ⁵⁵, TlBiSe_2 ⁵⁶)

2.2.4. Topological Dirac Semimetals

As a development of the idea of the topological insulator, we can imagine the situation when there is no energy gap between the valence band and the conduction band (schematically shown in Figure 2.10). They touch each other at isolated momentum points. These points are called Dirac points. In these materials, we can observe linear dispersions across the 3D Dirac points along with all the momentum directions in the bulk. The crosses of the bands are protected by the symmetries of the system and cannot be removed by any perturbations of the Hamiltonian. In the typical situation, two gaps of close energies will hybridise and, due to the band repulsion mechanism, create the gap

in-between. But the occurrence of symmetries such as crystalline symmetry or time-reversal symmetry can close this gap. This is because symmetries cause the crossing bands to have different quantum numbers and cannot hybridise. That is why these materials are called symmetry protected⁵⁷.

Due to the similarity of the topological Dirac semimetal phase and topological insulator phases, it seems a natural approach to try to transform one into the other through a quantum phase transition. In this case, topological Dirac semimetal can be achieved at the critical point. This method requires fine-tuning of the chemical composition, and the Dirac fermions produced in this way are usually unstable. This is possible by using the symmetry of the crystals through which Dirac's 3D fermions can be stabilized. The consequence of the unique electronic structure of the topological Dirac semimetals is very high bulk carrier mobility, oscillating quantum spin Hall effect high-temperature linear quantum magnetoresistance, and giant diamagnetism⁵¹.

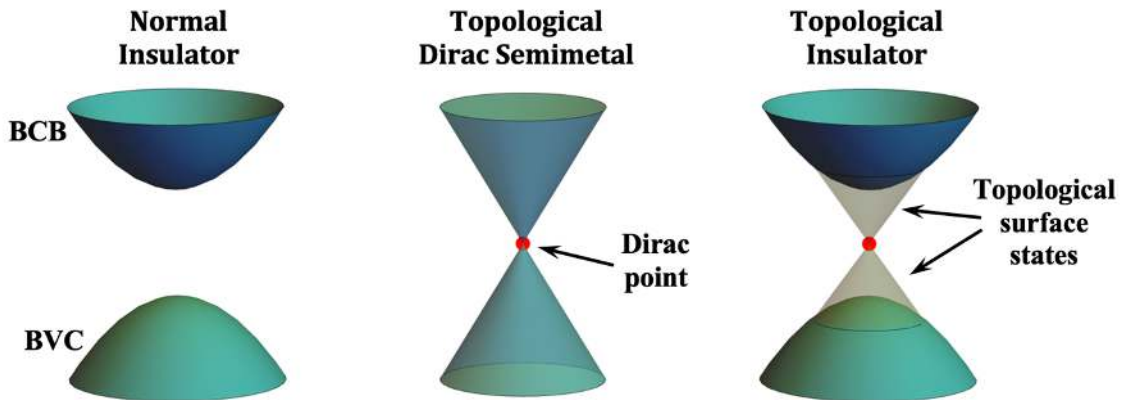


Figure 2.10. Comparison of the band structure of normal insulator, the topological Dirac semimetal, and topological insulator with surface states. The topological Dirac semimetal can be considered as the critical phase between the TI and the normal insulator.

The first experimentally discovered three-dimensional topological Dirac semimetal (TDS) Na_3Bi , for which stabilization occurs thanks to the three-fold rotational symmetry of the crystal structure⁵⁸. Another example of such a compound is a Cd_3As_2 with four-fold rotational symmetry⁵⁹.

2.2.5. Topological Weyl Semimetals

In the 1930s, Hermann Weyl simplified the Dirac equation by setting the mass equal to zero. In this way, he described the existence of massless fermions with definite chirality. For many years it was believed that neutrinos are an example of the physical realisation of Weyl fermions; unfortunately, the discovery of their mass proved that to date this elementary fermion has not yet been observed in high-energy physics. However,

the fermions described by the Weyl equation could be realized in condensed matter systems, leading to a new type of topological material called a topological Weyl semimetal. The characteristic feature of these materials is linear dispersion of the bulk and topological surface state on the surface that forms the so-called Fermi arcs that connect a pair of Weyl points with a Chern number equal to 1.

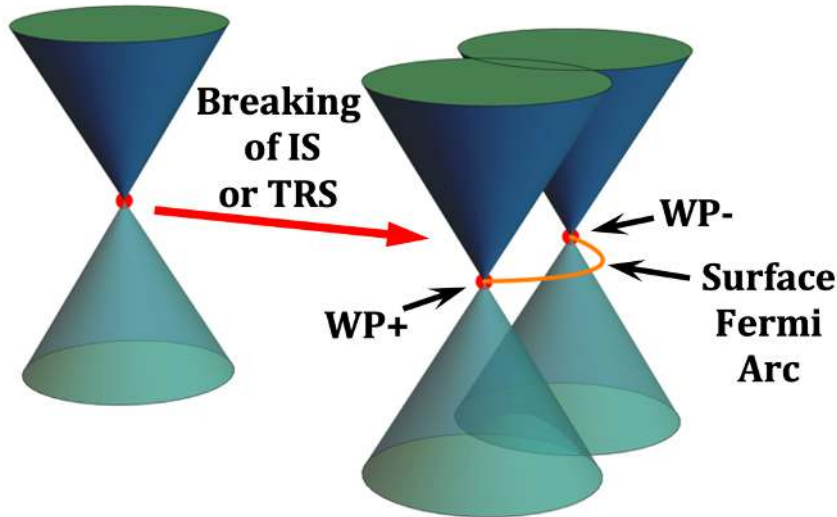


Figure 2.11. Cartoon illustration of the splitting of a Dirac point into a pair of Weyl points with a surface Fermi arc connecting them.
WP+/-, Weyl points with opposite chirality,
IS – inversion symmetry, TRS – time-reversal symmetry.

A key phenomenon necessary for the physical realization of a topological Weyl semimetal is the breaking of either time-reversal symmetry or inversion symmetry. There are known compounds in which these symmetries break spontaneously. As a result, the bulk Dirac points, like the one observed in the topological Dirac semi-metals, are split into a pair of Weyl points, as schematically illustrated in Figure 2.11. To date, the existence of Weyl states has been successfully confirmed in compounds such as NbAs, NbP, TaP and TaAs by the ARPES method^{58,60–63}. There is also a proposition of different methods that could lead to the creation of the topological Weyl semimetal. One of them is based on the breaking of either time-reversal symmetry or inversion symmetry in a topological Dirac semimetal by applying the high magnetic field or mechanical strain. Another idea of creating these materials is to stack topological insulators and normal insulators, although due to their complexity, it remains a theoretical proposition⁵¹. There are two classes of Weyl semimetals (type I and type II), depending on whether the system preserves or violates Lorentz symmetry. In the case of type II, the Weyl cones are tilted, resulting in a complex FS of electron and hole nature⁶⁴.

2.2.6. Topological Nodal-Line Semimetals

In the next type of topological materials, the discrete nodes in the momentum space are replaced by the continuous curves called the nodal lines that are formed at the linearly dispersive conduction and valence bands⁶⁵. The nodal lines can take the form of a line through the Brillouin zone whose ends meet at the Brillouin zone boundary⁶⁶ or fold into a closed loop inside the Brillouin zone⁶⁷, or even create a chain consisting of several connected loops⁶⁸. The schematic illustration for the Dirac line nodes is shown in Figure 2.12.

Like other topological materials, the full topological classification of nodal lines semimetals could be determined by the topological invariant, whose form depends on the symmetry group that protects the structure and dimension of the node. There are three types of nodal lines differing in symmetry protection: nodal lines protected by the mirror reflexion symmetry; protected by inversion, time-reversal, and SU(2) spin-rotation symmetry; and protected by twofold screw rotation, inversion, and time-reversal symmetry⁵⁷.

This type of structure was experimentally confirmed in several compounds, including PtSn₄⁶⁹, InBi⁷⁰, SrAs₃⁷¹, (Tl/Pb)TaSe₂⁷², (Hf/Zr)SiS⁷³.

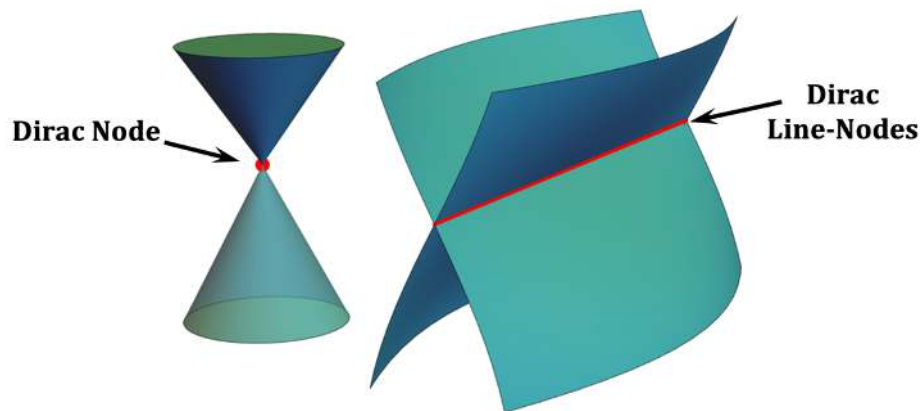


Figure 2.12. Schematic illustration for the Dirac line-nodes in Topological Nodal Line Semimetal.

The evolution of the nodal line with symmetry breaking (like mirror reflexion or nonsymmorphic symmetry) is important for the understanding and discovery of novel topological materials, as the nodal lines can be fully gapped or gapped into several nodal points; thus, topological nodal line can be considered as the parent compound of a topological insulator, topological Dirac semimetal, or topological Weyl semimetal⁵¹.

2.2.7. Topological Chiral Semimetals

Research on topological materials has opened the way to the discovery of new quasiparticles in solid-state physics that do not have analogies in particle physics⁷⁴. One of the proposed systems in which such states can be observed are crystals with a chiral structure. There are materials with a lattice structure in which the absence of inversion, mirror, or other roto-inversion symmetries results in a well-defined handedness⁷⁵. In such chiral crystals with neither mirror nor inversion symmetry, fermions with high Chern numbers (larger than in Weyl semimetals) and long Fermi arc states were observed. Examples of chiral crystals in which topological properties were observed by ARPES measurements are PtAl, PtGa, PdGa, RhSi, CoSi, and RhSn⁵¹.

2.3. Description of Investigated Systems

2.3.1. $\text{FeTe}_x\text{Se}_{1-x}$

The discovery of unconventional superconductivity in iron compounds is one of the early twentieth century's most important developments in solid state physics. The mechanism of pairing that takes place in these compounds is still a matter of debate. Doping these materials with transition metals can lead, depending on the system, to inducing or suppressing superconductivity. The study of the phase diagrams obtained in this way is one of the most important methods used to understand these compounds. An example of a compound particularly attractive in terms of doping studies is a representative of the family '11', the superconducting $\text{FeTe}_x\text{Se}_{1-x}$.

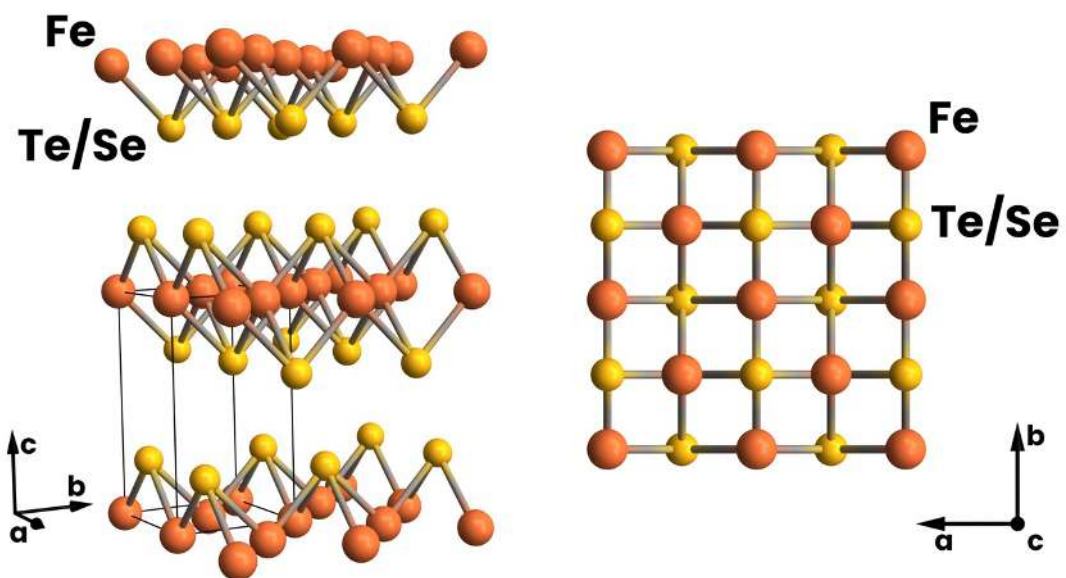


Figure 2.13. Crystal structure of $\text{FeTe}_x\text{Se}_{1-x}$.

$\text{FeTe}_x\text{Se}_{1-x}$ compounds are characterised by a relatively simple crystallographic structure and chemical formula. $\text{FeTe}_x\text{Se}_{1-x}$ crystallises in the tetragonal space group $P4/nmm$ ⁷⁶. The structure is two-dimensional and consists of sheets of $\text{FeTe}_x\text{Se}_{1-x}$, orientated in the (001) direction, in which iron atoms are surrounded by alternating Fe/Se atoms, forming a checkerboard pattern.

The phase diagram of $\text{FeTe}_x\text{Se}_{1-x}$ consists of three main regions: antiferromagnetic, appearing for low Se concentrations; superconducting, observed throughout the range, except for Te values above about 0.9; paramagnetic, occurring above T_c ⁷⁶⁻⁷⁹. The bulk superconductivity coexists with antiferromagnetic order in the crystals with Se concentration in the range of 0.05 to 0.18⁷⁸. The critical temperature changes from 8 K⁸⁰ to 14 K⁸¹. There are also reports of observations of spin density waves or spin glass⁸².

$\text{FeTe}_x\text{Se}_{1-x}$ also offers the opportunity to study the influence of substituting magnetic atoms in place of iron on the transport properties and electronic structure.

Replacement of iron with, for example, cobalt or nickel adds additional electrons to the system, which has several physical consequences. It has been shown that a small disorder introduced into the magnetic sublattice by partial replacement of Fe with a small number of atoms with spin values different from those of Fe completely suppresses superconductivity in this system, which can be explained by the magnetic scattering of the Cooper pair^{1,81,82}. An exemplary graph showing the change in critical temperature under the influence of substituting transition metals in place of iron in $\text{FeTe}_x\text{Se}_{1-x}$ is shown in Figure 2.14.

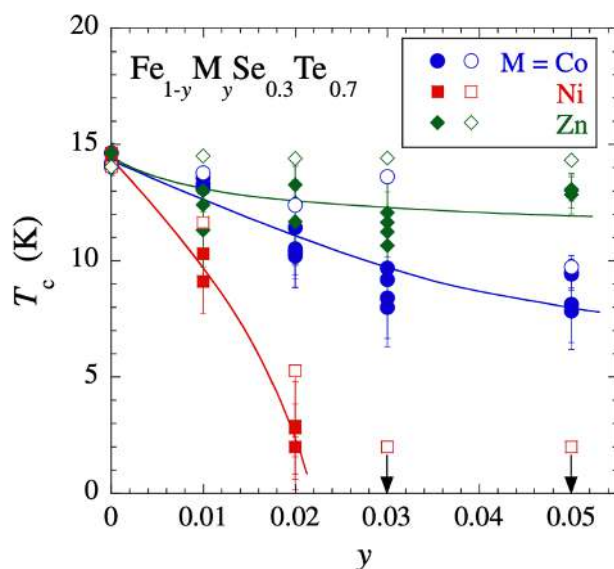


Figure 2.14. Change in critical temperature under the influence of substituting nickel, cobalt, and zinc in place of iron in $\text{Fe}_{1-y}\text{MySe}_{0.3}\text{Te}_{0.7}$. Taken from Ref. 83.

Furthermore, studies of single $\text{FeTe}_x\text{Se}_{1-x}$ crystals doped over a wide range of impurity levels with two transition metal elements, Co and Ni, reveal a change of sign of the Hall coefficient to negative at low temperatures. At high temperatures, it remains positive, which suggests that the remaining hole pockets survived doping, and holes are localized after the temperature is reduced. The behaviour of the Hall coefficient for different concentration of the dopant and several temperatures is shown in Figure 2.15. There are suggestions that the suppression of superconductivity is related to electron doping in the case of Co impurity, while Ni impurity most likely induces additional strong localisation of electrons.¹ Changes in the transport properties of these compounds are associated with changes in their electronic structure, and two main scenarios are distinguished: rigid^{84,85} and non-rigid band shift^{31,86}. The first is a simple band shift, which can alternatively be understood as a Fermi level shift. In the second case, the band structure is deformed as a result of more complex interactions. Before our research, the literature on $\text{FeTe}_x\text{Se}_{1-x}$ only showed the results of nickel doping indicating non-rigid band shift³¹.

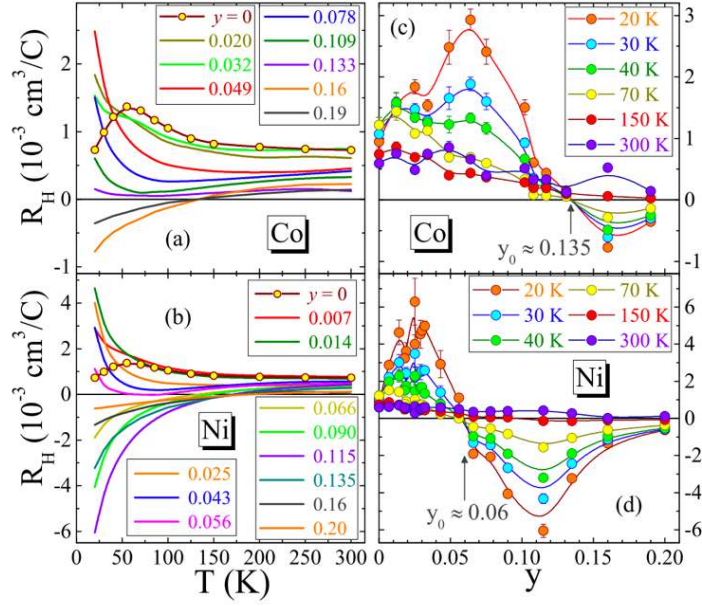


Figure 2.15. Hall coefficient R_H as a function of temperature for $\text{FeTe}_x\text{Se}_{1-x}$ crystals doped with (a) Co and (b) Ni, and as a function of dopant concentration y and for various temperatures for (c) Co and (d) Ni. Taken from Ref. 1.

The superconductivity in $\text{FeTe}_x\text{Se}_{1-x}$ compounds is of particular interest due to its reported probable topological nature. The iron-based superconductor $\text{FeTe}_{0.45}\text{Se}_{0.65}$ has been found to host Dirac-cone-type spin-helical surface states at the Fermi level and the surface states of $\text{FeTe}_{0.45}\text{Se}_{0.65}$ are topologically superconducting and provide the platform for the realisation of Majorana states⁹.

2.3.2. $\text{CaFe}_{2-x}\text{Co}_x\text{As}_2$

Another interesting family of iron-based superconductors is the so-called 122 family with the structure type AFe_2As_2 . The representative of these compounds is the CaFeAs_2 , the parent compound in which superconductivity appears with the doping. It is a layered compound; Ca atom is bonded in a body-centred cubic geometry to eight equivalent As atoms. Fe is bonded to four equivalent As atoms to form FeAs_4 tetrahedra. As is bonded in an 8-coordinate geometry to four Ba and four Fe atoms. The structure of CaFe_2As_2 in the tetragonal phase is shown in Figure 2.16.

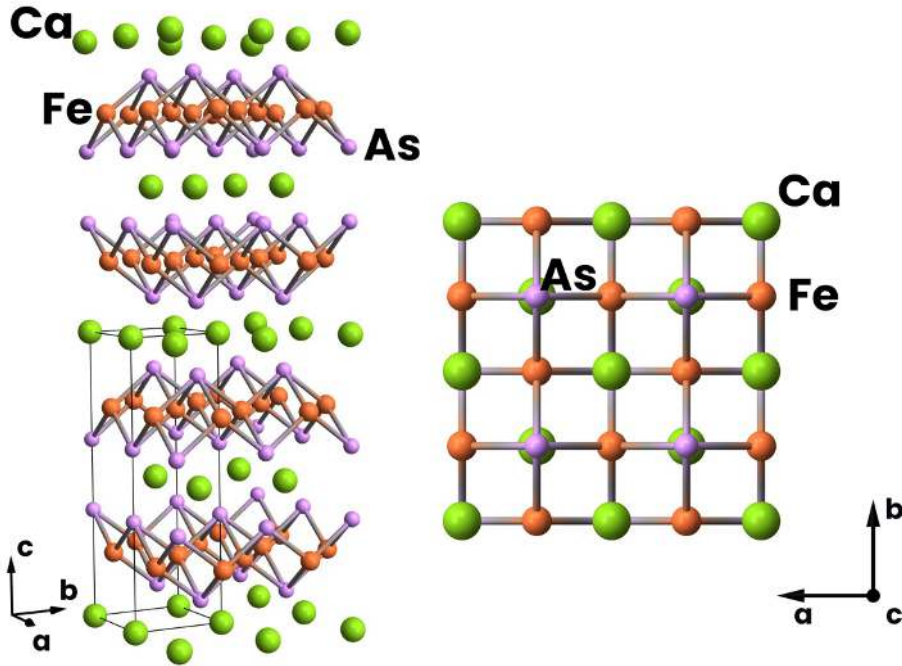


Figure 2.16. Crystal structure of CaFe_2As_2 in the tetragonal phase.

The rich phase diagram of this compound is its distinguishing feature^{2,34,36}. It contains paramagnetic phase (P), orthorhombic antiferromagnetic phase (AFM), spin-density waves and superconductivity. Substitution of cobalt for iron in this compound induces superconductivity, and it is observed in a wide range of diagrams that cross through both the AFM and P regions. The maximum critical temperature of $\text{CaFe}_{2-x}\text{Co}_x\text{As}_2$ is about 20 K². Similar effects are also observed when external pressure is applied, in which case superconductivity is observed from 6 kbar³. Phase diagrams for a Co-doped and pressurised compound are shown in Figure 2.17.

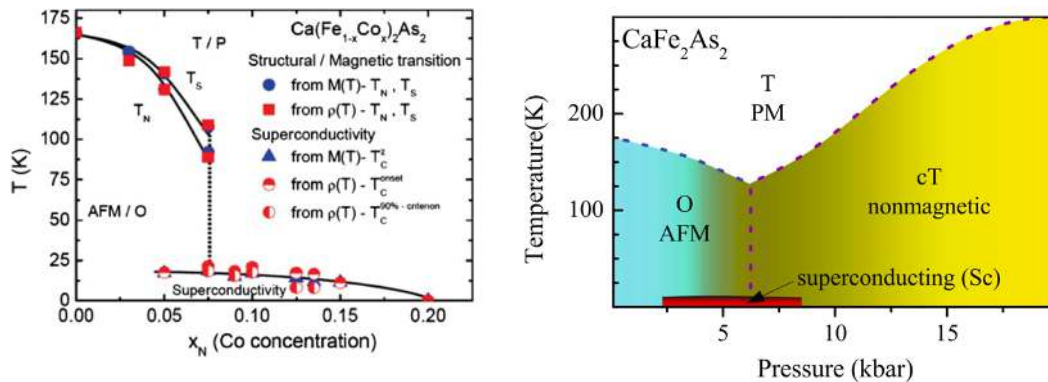


Figure 2.17. Electronic phase diagram of $\text{CaFe}_{2-x}\text{Co}_x\text{As}_2$, left: temperature- Co concentration diagram, right: temperature - pressure diagram. Taken from Ref. 2 (left) and 3 (right).

CaFe_2As_2 crystallizes in the $I4/mmm$ tetragonal space group with lattice parameters $a = 3.883 \text{ \AA}$ and $c = 11.750 \text{ \AA}$. Below 170 K first-order structural phase transition to a low-temperature orthorhombic phase is observed³⁷. This structure is described by the $Fmmm$ space group with the lattice parameters $a = 5.506(2)$, $b = 5.450(2)$, $c = 11.664(6)$ ³. The phase diagram also contains a collapsed tetragonal structure observed under the application of pressure. For a collapsed tetragonal structure, the constant c contracts by 9%⁸⁷. The differences between the crystal structures in each of the phases are shown in Figure 2.18.

The electronic structure of CaFe_2As_2 in the tetragonal phase is analogous to that of other iron superconductors and consists of two-dimensional cylinders intersecting the Fermi level in the center and corners of the BZ. The band crossing the Fermi level near Γ point forms hole-like pockets and the electron pockets at M points³. Changes in the band structure caused by the substitution of cobalt for iron are the subject of Chapter 2 of this thesis, however, there are many reports in the literature on the observation of the structure of a similar compound, BaFe_2As_2 . It has been shown that in the case of BaFe_2As_2 , cobalt doping causes a band shift that can be described as a rigid band shift³. In the orthorhombic phase, a structure associated with the spin density waves is observed, which manifests itself in characteristic petal-like shapes on the Fermi surface^{5,88}.

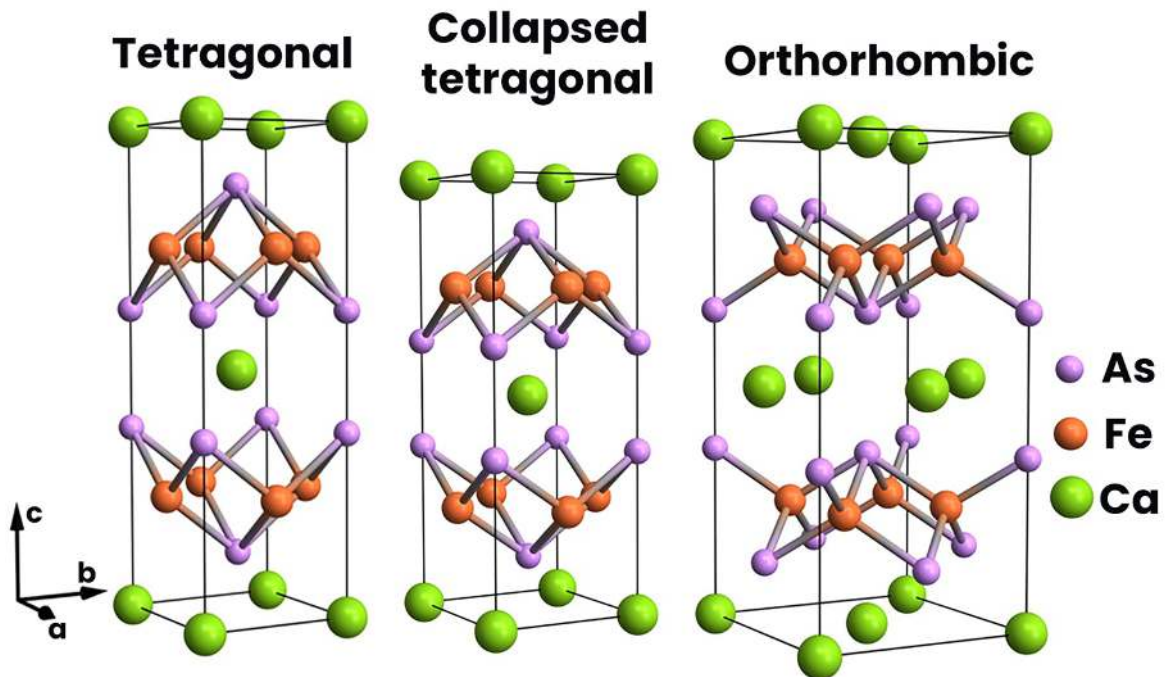


Figure 2.18. Crystal structure of CaFe_2As_2 in tetragonal, collapsed tetragonal and orthorhombic phase.

The existence of nontrivial topology has been observed^{11,89–95} and theoretical predictions are suggesting the existence of Dirac cones with the same chirality at the border of the Brillouin zone. The occurrence of Dirac states in this family is related to the physical symmetry and topology of the band structure, which stabilizes the ground state of the gapless spin density waves phase^{12,13}. There are experimental reports of observations of the Dirac cone in BaFe_2As_2 ⁹⁶.

2.3.3. LaTSb₂ (T=Ag, Cu)

In recent years, properties that develop the idea of a classical topological insulator have been predicted in various materials, including layered heavy metal square-lattice compounds (A/RE)T(Sb/Bi)₂, where A/RE is an alkali metal or a rare earth element and T denotes the d-electron transition metal⁹⁷. Examples of such compounds are LaAgSb₂ and LaCuSb₂, for which theoretical calculations predict the existence of Dirac-like structures^{16,98}. These compounds are particularly interesting because LaAgSb₂ is a charge density waves (CDW) material⁸ and both LaAgSb₂ and LaCuSb₂ are superconductors^{6,7} so there is a possibility of coexistence of these phases with hypothetical Dirac fermions.

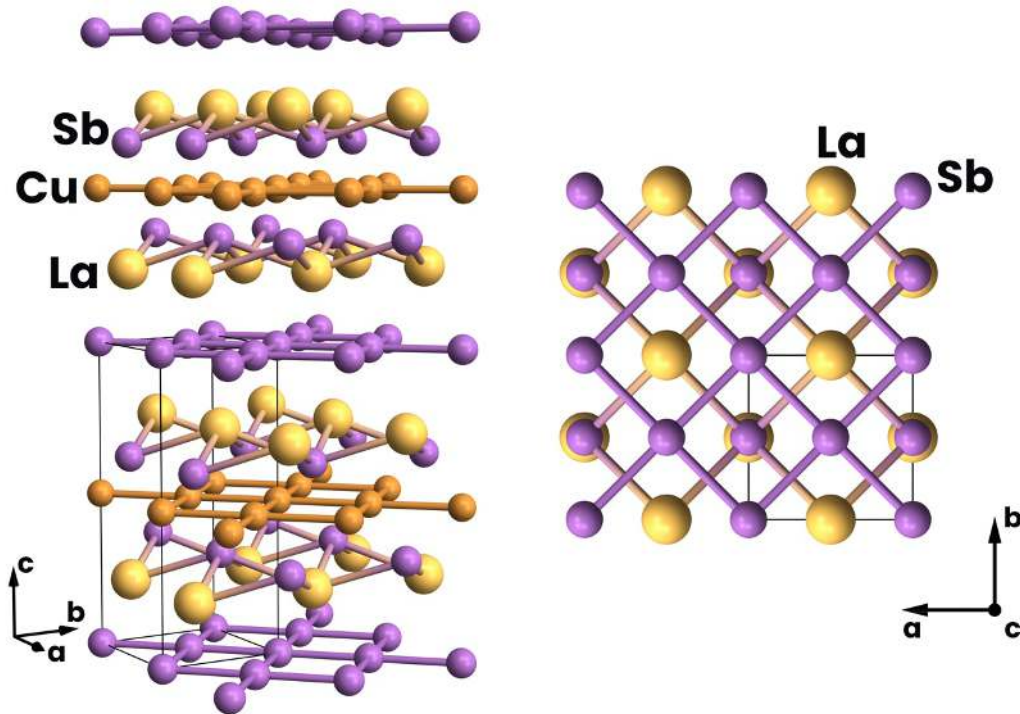


Figure 2.19. Crystal structure of LaCuSb₂.

LaCuSb₂ and LaAgSb₂ crystallize in the tetragonal P4/nmm space group. The lattice constants of LaCuSb₂ are reported as $a = b = 4.382 \text{ \AA}$ and $c = 10.209 \text{ \AA}$ ⁹⁹ and for LaAgSb₂ it is $a = b = 4.359 \text{ \AA}$, and $c = 10.787 \text{ \AA}$ ¹⁰⁰. Crystal structure of LaCuSb₂ is shown in the Figure 2.16.

In the case of LaAgSb₂, a charge density wave phase was determined using the X-ray scattering study, and two different CDW orderings were observed. The first one was observed below 207 K and developed with wave vector $q_1 \sim 0.026 \times (2\pi/a)$ in a-b plane. The second appears below 186 K, with $q_2 \sim 0.16 \times (2\pi/c)$, and along the c direction⁸. The realisation of the CDW phase can be associated with the nesting of the Fermi surface¹⁰¹. The ARPES measurement performed on this material revealed the diamond-shaped Fermi surface and linear bands, which have been described as Dirac-like structures¹⁴. Furthermore, transport and magnetic properties indicate the existence of a topological

phase in LaAgSb_2 ^{102–104}. The signature of Dirac fermions is seen in magnetoresistance, Hall resistivity and magneto thermopower. The opposite sign between the Hall resistivity and the Seebeck coefficient is observed, indicating a possible multiband effect. Hall resistivity analysis suggests that Dirac holes, which dominate electron transport, have higher density and higher mobility than conventional electrons¹⁰⁴. LaAgSb_2 as a host of Dirac states is also supported by the first-principles electronic structure study¹⁰⁴. Chapter 3 of this work presents a detailed study of the electronic structure of this compound and an explanation of the nature of the observed states.

LaCuSb_2 is a superconductor with the transition temperature $T_C = 0.9 \text{ K}$.⁶ Its Fermi surface is similar to that observed for LaAgSb_2 , and consists of several pockets forming the diamond-like shape^{15,98}. It has also been shown that there are several linear bands, which are interpreted as a sign of the presence of Dirac fermions in this material. Additionally, this thesis was confirmed by observation of the Shubnikov-de Haas (SdH) oscillations¹⁵. The systematic analysis of the electronic structure of this compound is the subject of Chapter 4.

3. Experimental Technique

3.1. Angle-Resolved Photoemission Spectroscopy

Angle-resolved photoemission spectroscopy (ARPES) is an experimental technique that is used to study the electronic structures of the solids. The idea of the method is based on the photoelectric effect, a physical phenomenon involving the emission of an electron from the surface of a material under the influence of an electromagnetic wave. It was originally observed by Heinrich Hertz in 1887 and explained by Albert Einstein in 1905. The energy of light is absorbed in the form of quanta. Einstein assumed that removing an electron from a metal surface requires some work called a work function, which is a material quantity. The remaining energy is carried by the emitted electron. From these considerations, the formula follows:

$$E_{kin,max} = h\nu - \phi, \quad (3.1)$$

where $E_{kin,max}$ – maximal kinetic energy of the emitted electron, h – Planck constant, ν – photon frequency, ϕ – work function. The energy of photoelectrons depends on the frequency of light, and below a certain frequency, no photoelectric effect occurs.

In the ARPES experiment, a crystalline sample is illuminated with monochromatic light, which results in the emission of photoelectrons. The geometry of the system is designed to detect the polar (θ) and the azimuthal (φ) angle at which the electrons escaped the sample surface (Figure 3.1). The kinetic energy of photoelectrons is measured using a hemispherical electron energy analyzer. Information about emission angles and kinetic energy allows us to reconstruct the electronic structure in the k-space.

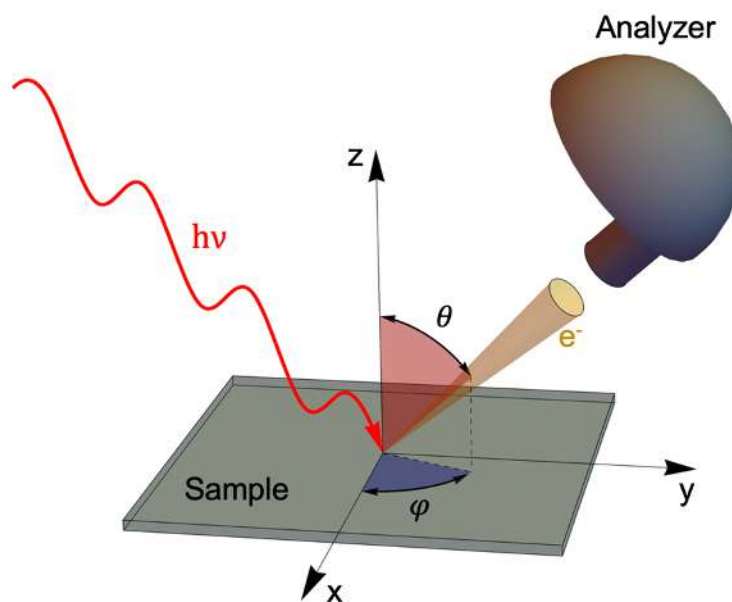


Figure 3.1. Schematic presentation of the geometry of the ARPES experiment.

The photoemission process could be described by two models. The first one is called the three-step model, and the photoemission process is divided into three independent stages:

- electron excitation in the bulk,
- transport of the excited electron to the surface,
- transition to vacuum through the surface.

The first step is to excite an electron in the crystal. The electron is in the initial Bloch state; due to photon absorption, it is excited to its final state (E_f) with an energy equal to the sum of the initial energy (E_i) and the energy of electromagnetic radiation ($h\nu$):

$$E_f = E_i + h\nu. \quad (3.2)$$

The kinetic energy of a photoelectron E_{kin} can be related to the binding energy E_B of the electronic state inside a solid by using the law of conservation of energy:

$$E_{kin} = h\nu - \phi - |E_B|. \quad (3.3)$$

This idea is explained graphically in Figure 3.2.

For the free electron gas there are no final states because of the single parabolic dispersion relation; therefore, simple transitions are possible only with the participation of the crystal lattice, which provides the electron final states. Thus, for the optical transition between the bulk initial (\mathbf{k}_i) and final state (\mathbf{k}_f) described in the extended-zone scheme, the following vector is conserved:

$$\mathbf{k}_f - \mathbf{k}_i = \mathbf{G}. \quad (3.4)$$

It should be noted that these considerations were made with the assumption that the momentum of the photon is negligible in relation to the momentum of the electron.

The translational symmetry of the surface in the x-y plane causes the perpendicular component of the wave vector is conserved (k_{\parallel}) in the photoemission process:

$$k_S^{\parallel} = k_V^{\parallel} = \frac{1}{\hbar} \sqrt{2m E_{kin}^V} \sin\theta_V \quad (3.5)$$

The index S represents the bulk of the crystal, and V represents the vacuum.

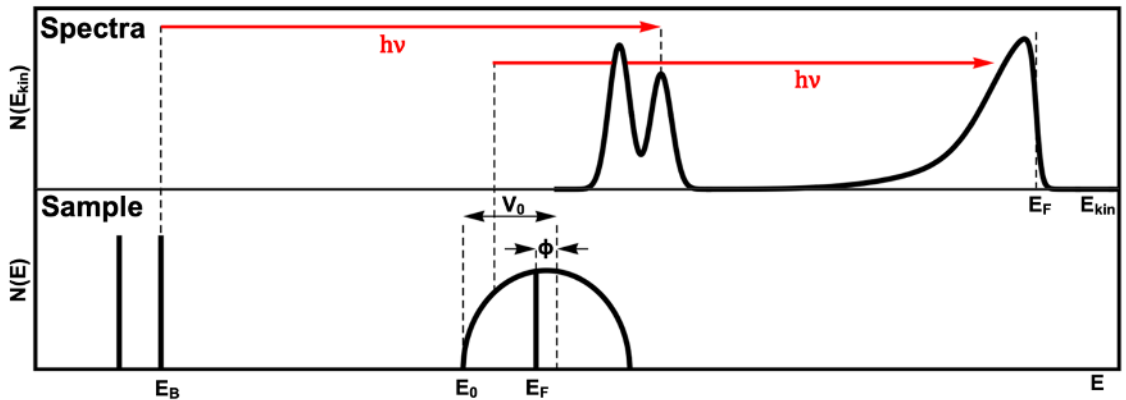


Figure 3.2. The diagram of the photoemission process.

E_B – binding energy, E_F – Fermi energy, E_0 – bottom of the valence band, E_{kin} – kinetic energy, $h\nu$ – photon energy, V_0 – inner potential, ϕ – work function, $N(E)$ – density of states.

The perpendicular component of the wave vector (k^\perp) is not conserved due to the existence of a potential barrier that breaks the translational symmetry in the direction perpendicular to the sample surface (Figure 3.3). It is assumed that the electron in its final state is described by the parabolical dispersion both inside the crystal and after it has passed into a vacuum. This model introduces the V_0 parameter, called the inner potential. It is a parameter of a free electron final state model, which can be interpreted as a potential barrier related to surface¹⁰⁵, and its value must be determined experimentally. The diagram of the model is presented in Figure 3.3. One could use this assumption and the near-free-electron description of the final bulk Bloch state to find k^\perp :

$$E_f(\mathbf{k}) = \frac{\hbar^2 \mathbf{k}^2}{2m} - |E_0| = \frac{\hbar^2 (k_\parallel^2 + k^\perp{}^2)}{2m} - |E_0|, \quad (3.6)$$

where the electron momenta are defined in the extended-zone scheme and E_0 corresponds to the bottom of the valence band. Now, using (3.2) and (3.5) we can write:

$$k^\perp = \frac{1}{\hbar} \sqrt{2m(E_{kin} \cos^2 \theta + V_0)}. \quad (3.7)$$

The inner potential is given by $V_0 = |E_0| + \phi$ and corresponds to the bottom of the valence band referenced to the vacuum level E_v .

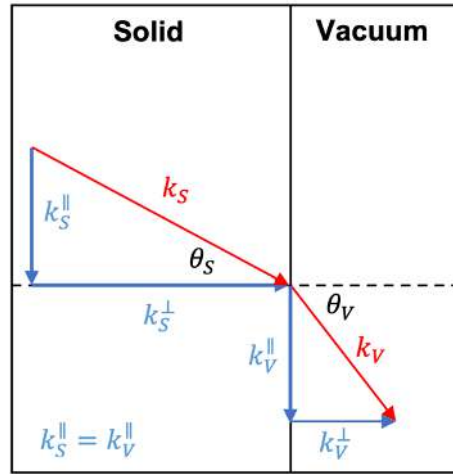


Figure 3.3. Refraction of the wave vector on the crystal surface.

The more advanced one-step model uses a quantum mechanics approach to consider the initial state of a system in which the electron is in a ground state. This state is denoted by ψ_i^N , it is the N-electron crystal eigenstate. As a result of the interaction with electromagnetic radiation, the electron shifts to the final vacuum state ψ_f^N , which is the (N-1)-electron state of the system. The probability of the transition w_{fi} between the initial ($E_i^N = E_i^{N-1} - E_B^k$, E_B^k - the binding energy of the photoelectron) state and the final ($E_f^N = E_f^{N-1} - E_{kin}$) state is given by the Fermi golden rule:

$$w_{fi} = \frac{2\pi}{\hbar} \langle \phi_f^k | H | \phi_i^k \rangle \delta(E_f^N - E_i^N - h\nu), \quad (3.8)$$

The matrix elements $M_{fi}^{\vec{k}} \equiv \langle \phi_f^{\vec{k}} | H | \phi_i^{\vec{k}} \rangle$ representing the relationship between the N-electron state and the (N-1) -electron state. The interaction with the photon is given by the following Hamiltonian:

$$H = \frac{e}{2mc} (\mathbf{A} \cdot \mathbf{p} + \mathbf{p} \cdot \mathbf{A}) = \frac{e}{mc} \mathbf{A} \cdot \mathbf{p} \quad (3.9)$$

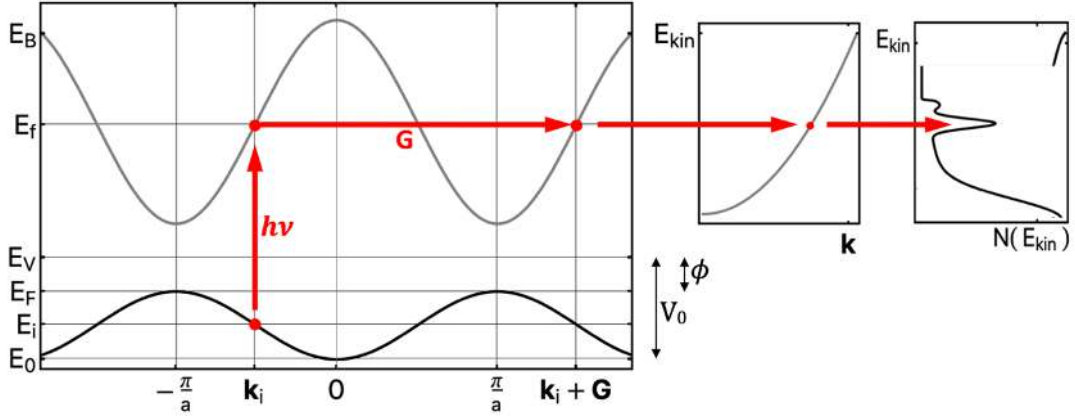


Figure 3.4. Diagram of the act of photoemission described with three-step nearly free electron model. (a) optical transition in the solid, (b) parabolical final state in the vacuum, (c) corresponding photoelectron spectrum.

and it is treated as a perturbation. The \mathbf{A} denotes the electromagnetic vector potential and the \mathbf{p} is the electromagnetic momentum operator. To simplify the problem, it is assumed that the photoelectron does not interact with the rest of the electrons. This assumption comes down to the fact that the act of photoemission is sudden, the electron is removed immediately, and the effective potential of the system changes discontinuously. The electron is excited from the orbital $\phi_i^{\vec{k}}$, with the wave vector \mathbf{k} . The wave function of the initial state ψ_i^N then takes the form:

$$\psi_i^N = \mathcal{A} \phi_i^{\vec{k}} \psi_i^{N-1}, \quad (3.10)$$

where \mathcal{A} is an antisymmetric operator and is necessary to satisfy the Pauli principle, and ψ_i^{N-1} could be understood as the remains of the N-particle wavefunction after one electron was removed. In the same way, we can decompose the wave function corresponding to the final (ψ_f^N) state:

$$\psi_f^N = \mathcal{A} \phi_f^{\vec{k}} \psi_f^{N-1}. \quad (3.11)$$

Using equations (3.10) and (3.11) one can write the matrix elements from (3.8) as:

$$M_{fi}^{\vec{k}} = \langle \psi_f^N | H | \psi_i^N \rangle = \langle \phi_f^{\vec{k}} | H | \phi_i^{\vec{k}} \rangle \langle \psi_m^{N-1} | \psi_i^{N-1} \rangle \quad (3.12)$$

where $\langle \phi_f^{\vec{k}} | H | \phi_i^{\vec{k}} \rangle$ is one electron dipole matrix element and $\langle \psi_m^{N-1} | \psi_i^{N-1} \rangle$ is (N-1)electron overlap integral. Hence, using (3.8) one can find the probability of the electron's transition from the initial state i to the excited state m :

$$w_{fi} = \frac{2\pi}{\hbar} \sum_{f,i} \left| M_{f,i}^{\vec{k}} \right|^2 \sum_m |c_{m,i}|^2 \delta(E_k + E_m^{N-1} - E_i^N - hv), \quad (3.13)$$

where $|c_{m,i}|^2 = |\langle \psi_m^{N-1} | \psi_i^{N-1} \rangle|^2$. The total photoemission intensity is proportional to w_{fi} :

$$I(\mathbf{k}, E_{kin}) = \sum_{i,j} w_{fi}, \quad (3.14)$$

For weakly interacting systems, it is assumed that the initial state of the remaining electrons is the same as their final state: $c_{m,i} = \delta_{m,0}$. This simplification is justified when there is no strong correlation between electrons in the system and allows us to reduce formula (3.13) to the form:

$$w_{fi} = \frac{2\pi}{\hbar} \sum_{f,i} \left| M_{f,i}^{\vec{k}} \right|^2 \delta(E_k - (E_i + hv)), \quad (3.15)$$

The emission spectrum of the weakly correlated system consists of several individual peaks, the intensity of which depends on the values of the elements of the \mathbf{M}_{if} matrix.^{105,106}

In the case where $|c_{m,i}|^2 \neq 0$, i.e. for correlated systems, the typical approach is to use the formalism of the Green function. Such a function $\mathcal{G}(t - t')$ is interpreted as the probability amplitude that the electron added to the system in a Bloch state with momentum \mathbf{k} at a time $t = 0$ will still be in the same state after time $|t - t'|$. The total photoemission intensity (3.14) could be written as:

$$I(\mathbf{k}, E_{kin}) = \frac{2\pi}{\hbar} \sum_{f,i} \left| M_{f,i}^{\vec{k}} \right|^2 A(\mathbf{k}, \omega), \quad (3.16)$$

where $A(\mathbf{k}, \omega)$ is one particle spectral function and $\omega = E_k - hv$. The function $\mathcal{G}(t - t')$ could be used to define the retarded Green's $G(\mathbf{k}, \omega)$ function, which is related to the full spectral function $A(\mathbf{k}, \omega)$ via:

$$A(\mathbf{k}, \omega) = -\frac{1}{\pi} \text{Im} G(\mathbf{k}, \omega), \quad (3.17)$$

The photoemission probes only the occupied states, so to complete the description Fermi-Dirac distribution is necessary:

$$f(\omega) = \frac{1}{e^{\omega/k_b T} + 1}, \quad (3.18)$$

T is temperature and k_b Boltzmann's constant. Taking everything into account, photocurrent is proportional to:

$$I(\mathbf{k}, \omega) \sim \left| M_{f,i}^{\vec{k}} \right|^2 A(\mathbf{k}, \omega) f(\omega). \quad (3.19)$$

3.2. Measurement Systems

The ARPES measurements included in this doctoral dissertation were performed using the two experimental setups. The first one is located in the Laboratory of Photoelectron Spectroscopy in the Department of Solid-State Physics (Institute of Physics, Jagiellonian University in Krakow) and was bought due to the financial support from ATOMIN project. The experimental setup is equipped with a Scienta R4000 hemispherical photoelectron energy analyzer with a maximal resolution of 1.8 meV and 0.1° for energy and angles, respectively. Radiation for UPS measurements is provided by the helium lamp, $h\nu = 21.2$ eV and $h\nu = 40.8$ eV for the He I and He II spectral lines, respectively. The source of the high-energy photons used in XPS measurements is the X-ray tube ($h\nu = 1253.6$ eV and $h\nu = 1486.6$ eV). The slit of the analyzer is vertical, and the detailed geometry of the system is shown in Figure 3.5. The samples are cooled with a helium system operating in a closed circuit, which allows one to achieve a temperature of about 12 K. The movement of the sample is accomplished using a cryogenic manipulator that provides five axes of freedom. The system maintains an ultra-high vacuum of the order of 10^{-11} mbar. The system is equipped with a preparation chamber that is used to bombard a sample with argon ions and a heating chamber for sample annealing. The photo of the system is presented in Figure 3.6.

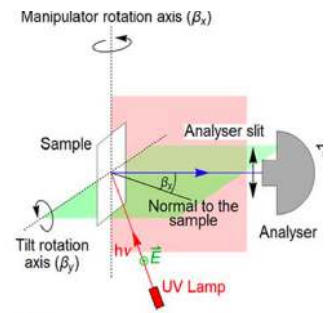


Figure 3.5. Geometry of the ARPES system in the Department of Solid State Physics (Jagiellonian University).

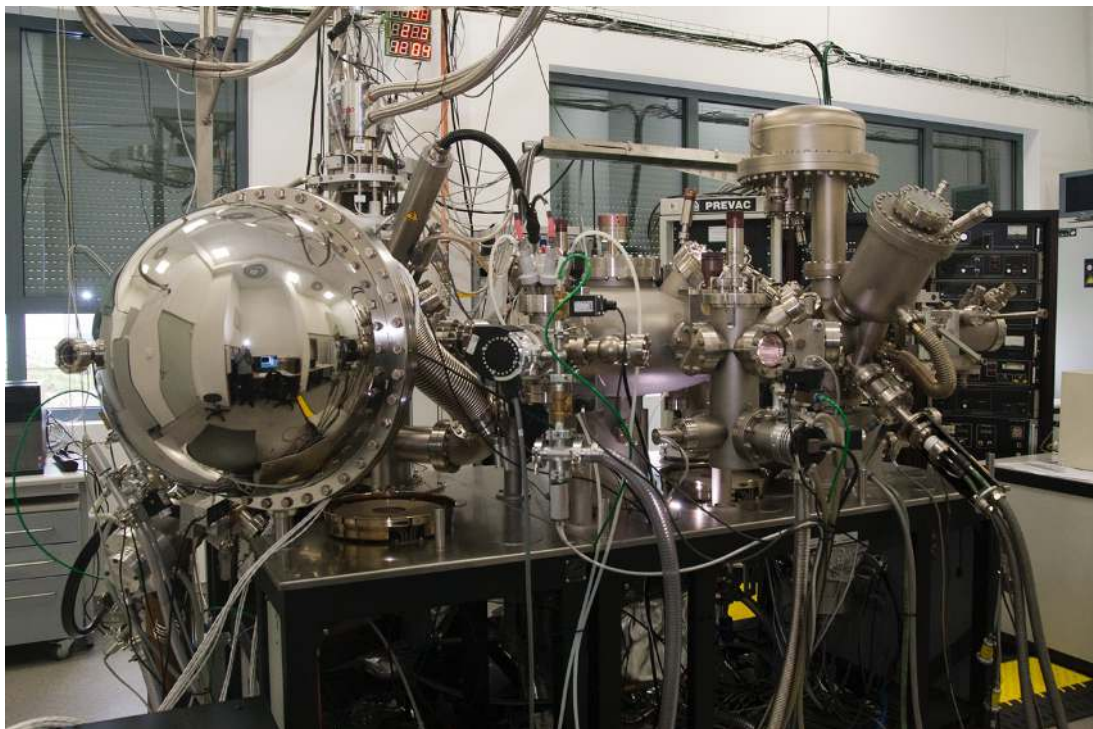


Figure 3.6. The ARPES measurement system is available in the Laboratory of Photoelectron Spectroscopy in the Department of Solid State Physics (Jagiellonian University).

The second experimental setup is the URANOS beamline at the National Synchrotron Radiation Centre SOLARIS in Krakow (Poland)¹⁰⁷. The light source is an elliptically polarizing Apple II quasiperiodic undulator that provides radiation in the range of ultraviolet to soft X with linear vertical, linear horizontal, circular, or elliptical polarization. Monochromatic light in the range from 12 to 400 eV is obtained using the plane grating monochromator (PGM), while for the low energy range (8-30 eV), a normal incident monochromator (NIM) is used. Photoelectrons are detected by a Scienta DA30L hemispherical analyzer with deflection mapping mode. The slit of the analyzer is vertical, the geometry is shown in Figure 3.7. The spectrometer's maximal energy and angular resolution are 1.8 meV and 0.1°, respectively, while the real maximal energy resolution of the beamline is about 4.5 meV. The samples are mounted to the cryogenic manipulator with five degrees of freedom and could be cooled to 6 K with the use of liquid helium. The photo of the URANOS beamline is presented in Figure 3.8.

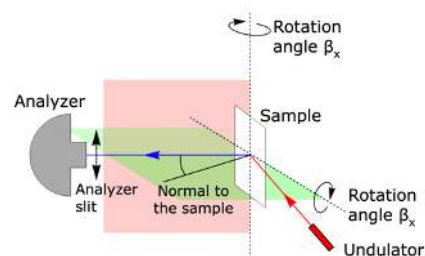


Figure 3.7. The geometry of the URANOS end station.

The end station is equipped with a preparation chamber enabling thermal annealing of the sample up to 1800 K, bombardment with argon ions, and vapor deposition of elements using two sources. The surface quality could be confirmed with the low-energy electron diffraction method (MCP-LEED)¹⁰⁸.



Figure 3.8. URANOS beamline in the National Synchrotron Radiation Centre SOLARIS in Kraków.

Using the Laue method, the single crystals used in the ARPES studies were oriented along highly symmetrical directions. A Laue camera working in the geometry of backscattered radiation was used. The X-ray radiation source was an X-ray tube with a Mo anode.

4. Effect of Electron Doping in $\text{FeTe}_{1-y}\text{Se}_y$ Realized by Co and Ni Substitution

M. Rosmus, R. Kurlito, D. J. Gawryluk, J. Goraus, M. Z. Cieplak, P. Starowicz

I am the first author of the paper, and my participation consisted of performing measurements using angle-resolved photoelectron spectroscopy (ARPES), analysing the obtained data and the results of theoretical calculations received by the theoretician (J.G.), writing code for visualisation and data analysis, preparing figures, discussions, and working on the first version of the manuscript together with the supervisor (P.S.). I prepared samples for measurements by orientation using the Laue diffraction method together with R.K. My contribution to the publication was 55%.

Effect of electron doping in $\text{FeTe}_{1-y}\text{Se}_y$ realized by Co and Ni substitution

M Rosmus¹, R Kurlito¹, D J Gawryluk^{2,3,5}, J Gorau⁴,
M Z Cieplak³ and P Starowicz^{1,5}

¹ M. Smoluchowski Institute of Physics, Jagiellonian University, Łojasiewicza 11, 30-348, Kraków, Poland

² Laboratory for Multiscale Materials Experiments, Paul Scherrer Institut, 5232 Villigen PSI, Switzerland

³ Institute of Physics, Polish Academy of Sciences, Lotników 32/46, 02-668 Warszawa, Poland

⁴ Institute of Physics, University of Silesia, ul. 75 Pułku Piechoty 1A, 41-500 Chorzów, Poland

E-mail: gawryluk@ifpan.edu.pl and pawel.starowicz@uj.edu.pl

Received 5 March 2019, revised 25 June 2019

Accepted for publication 15 July 2019

Published 27 August 2019



CrossMark

Abstract

Angle-resolved photoemission spectroscopy reveals the effects of electron doping, which is realized by Co and Ni substitution for Fe in a $\text{FeTe}_{1-y}\text{Se}_y$ ($y \sim 0.35$) superconductor. The data show consistent band shifts as well as expansion and shrinking of the electron and hole Fermi surface, respectively. Doping of either element leads to a Lifshitz transition realized as a removal of one or two hole pockets. This qualitatively explains the complex behavior of the Hall coefficient observed previously (Bezusyy *et al*, 2015 *Phys. Rev. B* **91**, 100502), including the change of sign with doping, which takes place only below room temperature. Assuming that Ni substitution should deliver twice as many electrons to the valence band as Co, it appears that such transfer is slightly more effective in the case of Co. Therefore, charge doping cannot account for a much stronger effect of Ni on the superconducting and transport properties (Bezusyy *et al*, 2015 *Phys. Rev. B* **91**, 100502). Although overall band shifts are roughly proportional to the amount of dopant, clear deviations from the rigid band shift scenario are found. The shape of the electron pockets becomes elliptical only for Ni doping, the effective mass of electron bands increases with doping, and a strong reduction of effective mass is observed for one of the hole bands of the undoped system. The topology of hole and electron pockets for superconducting $\text{Fe}_{1.01}\text{Te}_{0.67}\text{Se}_{0.33}$ with a critical temperature of 13.6 K indicates a deviation from nesting. Co and Ni doping causes further departure from nesting, which accompanies the reduction of critical temperature.

Supplementary material for this article is available [online](#)

Keywords: iron chalcogenides, chemical doping, band structure, Fermi surface, superconductivity, angle-resolved photoemission spectroscopy

(Some figures may appear in colour only in the online journal)

1. Introduction

The high critical temperature and evidence of an unconventional pairing mechanism in iron-based superconductors has attracted the attention of many researchers [1–4]. Although spin fluctuations are considered to be responsible for this mechanism, an important goal is to settle the physical properties of a given compound, which are real prerequisites of

superconductivity. For example, the topology of a Fermi surface (FS) corresponding to optimal doping does not seem to be universal for different superconducting families [5]. Nevertheless, marginal breakdown of nesting between hole and electron pockets may be advantageous for superconductivity, as this was proposed to support the spin fluctuation mechanism [6].

Chemical doping remains the key method to reveal phase diagrams of these systems with the superconducting phase located typically in the vicinity of magnetic order. A

⁵ Authors to whom any correspondence should be addressed.

realization of this can be accomplished e.g. by a substitution of transition metals for iron. Among the different elements, Co and Ni as dopants lead to a quite successful suppression of magnetic order and induction of superconductivity in 122 [7–9] and 1111 [10–12] iron pnictides. In contrast, these elements suppress superconductivity in highly correlated 11 iron chalcogenides [13–19]. The real effect of substituted Co or Ni in both iron pnictides and chalcogenides is a subject of debate. According to a number of theoretical predictions [20–22] and experimental results [18, 23, 24], these mainly act as scattering centers, which broaden bands and destroy magnetic order, allowing superconductivity. In this scenario the effect of charge doping might be secondary or even quite negligible. On the other hand, angle-resolved photoemission spectroscopy (ARPES) studies [25–34] indicate the effect of electron doping, which is more efficient in the case of Co as compared to Ni [30]. Quite ambivalent conclusions support scenarios of either a rigid [29, 30] or non-rigid [31, 34] band shift, and in the latter case dopants influence correlations. A non-rigid band shift is reported in the first paper devoted to ARPES studies of Ni-doped $\text{FeTe}_{1-y}\text{Se}_y$, [34] ARPES data for Co-doped $\text{FeTe}_{1-y}\text{Se}_y$ have not been published so far. It should be mentioned that $\text{FeTe}_{1-y}\text{Se}_y$ is of particular interest since the discovery of topologically non-trivial states in this system [35].

It is known that both Ni and Co doping suppress superconductivity in $\text{FeTe}_{1-y}\text{Se}_y$ chalcogenides [13–19]. Systematic investigations of transport and magnetic properties were performed for Co- and Ni-substituted $\text{FeTe}_{1-y}\text{Se}_y$ ($y \sim 0.35$) [15]. It was found that the superconducting critical temperature, which equals 14 K for the undoped material, is reduced with both dopants. The reduction rate per doped electron appears to be much faster in the case of Ni, considering that this element supplies twice as many electrons as Co. Moreover, Ni increases the electrical resistivity considerably and is considered to be a source of more efficient impurity scattering and correlations. Finally, the Hall coefficient (R_H) exhibits complex behavior analogical for both dopants. At high temperature it remains positive for all dopant concentrations, whereas at low temperature it increases first and then becomes negative showing another non-monotonic behavior with a minimum. These are symptoms of the interesting modifications of the band structure and FS.

The complex behavior found in the transport studies [15] motivated us to investigate the influence of Co and Ni doping on the electronic structure of $\text{FeTe}_{1-y}\text{Se}_y$ ($y \sim 0.35$) by means of ARPES. The data indicate a clear effect of electron doping on both electron and hole pockets with Lifshitz transition observed in the hole FS. Although energy shifts of different bands are comparable, some details indicate deviations from the rigid band shift scenario. The data are able to explain the peculiar behavior of R_H .

2. Experiment

Single crystals of $\text{Fe}_{1-x}\text{M}_x\text{Te}_{1-y}\text{Se}_y$ ($\text{M}=\text{Co}$ or Ni , $y \sim 0.35$) were grown using Bridgman's method [14]. They were characterized by means of scanning electron microscopy with energy-dispersive x-ray spectroscopy, x-ray diffraction, AC

magnetic susceptibility, measurements of electrical resistivity and R_H as described in the supplementary material [14, 15]. The electronic structure was investigated for superconducting $\text{Fe}_{1.01}\text{Te}_{0.67}\text{Se}_{0.33}$ with a critical temperature of $T_c = 13.6$ K as well as for one Co-doped ($\text{Fe}_{0.94}\text{Co}_{0.09}\text{Te}_{0.67}\text{Se}_{0.33}$) and two Ni-doped ($\text{Fe}_{0.97}\text{Ni}_{0.05}\text{Te}_{0.65}\text{Se}_{0.35}$ and $\text{Fe}_{0.91}\text{Ni}_{0.11}\text{Te}_{0.65}\text{Se}_{0.35}$) systems. The Co-doped crystal exhibited only an onset of the transition to superconductivity in resistivity ($T_{c,\text{onset}} = 4.6$ K) and magnetic susceptibility ($T_{c,\text{onset}} = 9.5$ K) without reaching zero resistivity down to 2 K (supplementary material). The Ni-doped crystals were non-superconducting⁶.

ARPES studies were performed with a Scienta R4000 hemispherical analyzer and He-I radiation ($h\nu = 21.218$ eV). The energy resolution was set to 15 meV. The experimental setup is presented in figure 1(a). Partially polarized light from the monochromator (85% of polarization) assures domination of σ -polarization for normal emission, where the sample surface is perpendicular to a mirror plane. The measurements were conducted typically at the temperature of 18 K, which corresponds to the non-superconducting state.

Density functional theory (DFT) calculations were performed with the APW+lo method using ELK-LAPW code (version 4.3.06) [36]. A full relativistic approach and the Perdew–Wang exchange–correlation potential were employed. The accuracy of calculations was set to high-quality preset (rgkmax = 8) and the number of k-points in the irreducible wedge of the Brillouin zone was 50 ($7 \times 7 \times 5$ k-grid), or 10⁶ ($100 \times 100 \times 100$ k-grid for FS), which was found sufficient to give appropriate results.

3. Results and discussion

FS mapping was performed for $\text{Fe}_{1.01}\text{Te}_{0.67}\text{Se}_{0.33}$ (referred to as 'undoped' in the following), $\text{Fe}_{0.94}\text{Co}_{0.09}\text{Te}_{0.67}\text{Se}_{0.33}$, $\text{Fe}_{0.97}\text{Ni}_{0.05}\text{Te}_{0.65}\text{Se}_{0.35}$ and $\text{Fe}_{0.91}\text{Ni}_{0.11}\text{Te}_{0.65}\text{Se}_{0.35}$ systems by means of ARPES with the geometry shown in figure 1(a). We use a notation of the two-dimensional (2D) surface Brillouin zone (figure 1(b)) and a convention of two Fe atoms in the Brillouin zone. Hole and electron pockets are found for all the studied compositions near the $\bar{\Gamma}$ and \bar{M} points, respectively (figures 1(c)–(f)). The expansion of electron pockets and the shrinking of hole pockets (discussed further in the text) with Co and Ni doping is observed. Electron pockets reached from $\bar{\Gamma}$ by lowering k_x (figures 1(c)–(f)) have a circular shape for the undoped or Co-doped system, whereas they become elliptical as a result of Ni doping. MDC fitting allowed us to determine the shape of these pockets and the fits are drawn with solid lines at $k_x \sim -1.2 \text{ \AA}^{-1}$. We neglected the dispersion along c^* and used the area of the elliptical fits to determine electron band filling, which was estimated as 2.3%, 4.2%, 3.8% and 7.2% for the undoped sample, $\text{Fe}_{0.94}\text{Co}_{0.09}\text{Te}_{0.67}\text{Se}_{0.33}$,

⁶ ARPES measurements were performed for $\text{Fe}_{1-x}\text{M}_x\text{Te}_{1-y}\text{Se}_y$ ($\text{M}=\text{Co}$ or Ni , $y \sim 0.35$) crystals obtained with a slow cooling method. In contrast, the data presented by Bezusyy *et al* [15] were obtained for fast-cooled crystals, which exhibited weaker crystal quality but better superconducting properties. Nevertheless, the effect of doping on the electronic structure is comparable for different final stages of the preparation process.

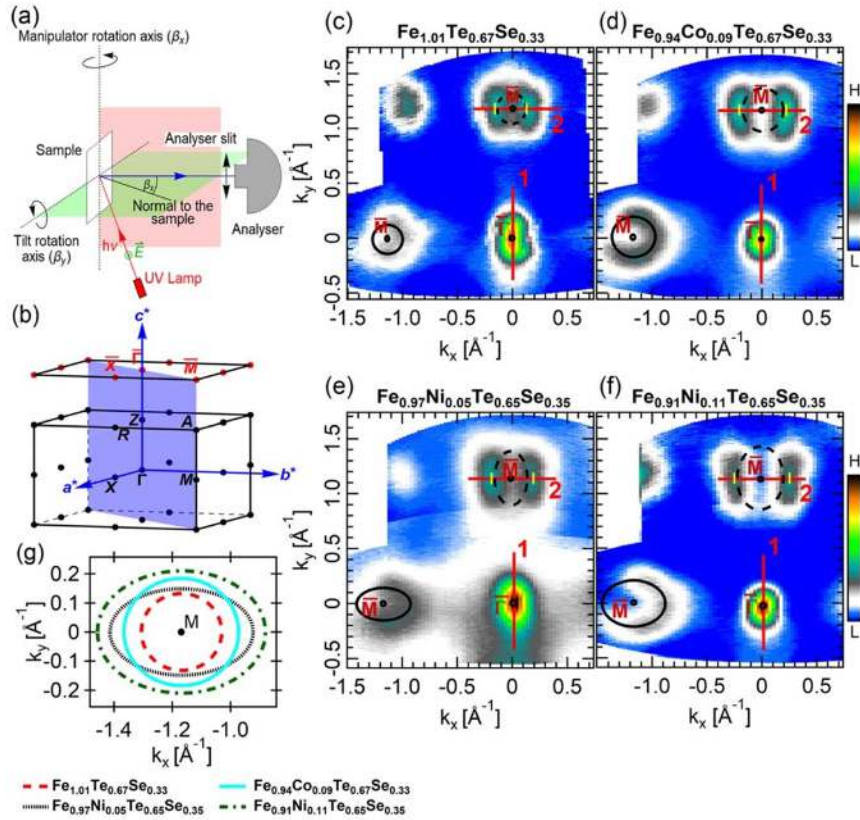


Figure 1. FS mapping of $\text{Fe}_{1-x}\text{M}_x\text{Te}_{1-y}\text{Se}_y$ ($\text{M}=\text{Co}, \text{Ni}$, $y \sim 0.35$) systems performed by means of ARPES using He-I ($h\nu = 21.218$ eV) radiation at a temperature of 18 K. Convention of two Fe atoms in the elementary unit cell is used. (a) Experimental geometry, (b) first Brillouin zone for tetragonal FeTe structure and surface Brillouin zone with high symmetry points. FS scans are performed for (c) $\text{Fe}_{1.01}\text{Te}_{0.67}\text{Se}_{0.33}$, (d) $\text{Fe}_{0.94}\text{Co}_{0.09}\text{Te}_{0.67}\text{Se}_{0.33}$, (e) $\text{Fe}_{0.97}\text{Ni}_{0.05}\text{Te}_{0.65}\text{Se}_{0.35}$, (f) $\text{Fe}_{0.91}\text{Ni}_{0.11}\text{Te}_{0.65}\text{Se}_{0.35}$. Solid black ovals represent fitted electron pockets and dashed black lines are their replicas obtained by symmetry operation. Solid red lines marked as ‘1’ and ‘2’ denote paths along which ARPES spectra were taken for further analysis. Yellow markers drawn on both sides of M points at $k_x = 0$ indicate Fermi vectors for the dispersion obtained along line 2. (g) Contours of electron pockets obtained from momentum distribution curve (MDC) fitting.

$\text{Fe}_{0.97}\text{Ni}_{0.05}\text{Te}_{0.65}\text{Se}_{0.35}$ and $\text{Fe}_{0.91}\text{Ni}_{0.11}\text{Te}_{0.65}\text{Se}_{0.35}$, respectively. Hence, the effect of electron doping is clearly visible for the electron part of FS. The presence of two electron pockets is not resolved and the given band filling corresponds to one of them. At this stage it is difficult to discuss the absence of the second pocket at $k_x \sim -1.2 \text{ \AA}^{-1}$. Possibly, it is not seen due to unfavorable photoemission matrix elements.

The pockets reached with increasing k_y have a different shape. They exhibit a loss of intensity along $k_x = 0$, which is due to a matrix element effect suppressing the spectral intensity in this region of a k -space [37]. It becomes evident that the dashed lines located around the M point at $k_y \sim 1.2 \text{ \AA}^{-1}$, which represent replicas of the pockets fitted at $k_x \sim -1.2 \text{ \AA}^{-1}$, do not follow the spectra. There may be different explanations for this fact. First of all, a depletion of spectral weight at $k_x = 0$ might influence the shape of the pockets determined from the ARPES experiment. However, dispersion obtained along line 2 by MDC fitting does not converge with the dashed FS for the dispersion along line 2

the Fermi vectors are marked with yellow dashes in figure 1(c)–(f). This indicates that the pocket observed at $k_y \sim 1.2 \text{ \AA}^{-1}$ is different than that at $k_x \sim -1.2 \text{ \AA}^{-1}$. This is not surprising, as it is known from DFT calculations and other ARPES results [34] that two electron pockets are present at M. Thus, the different shape of the spectra at $k_y \sim 1.2 \text{ \AA}^{-1}$ and $k_x \sim -1.2 \text{ \AA}^{-1}$ is related to the different contributions from two electron pockets in these regions, which occurs due to the different measurement geometry at $k_y \sim 1.2 \text{ \AA}^{-1}$ and $k_x \sim -1.2 \text{ \AA}^{-1}$. We do not support the hypothesis of non-equivalence of band structure along the x and y directions or the presence of orthorhombic distortion. First of all, the orthorhombic phase was not reported for $\text{FeTe}_{1-y}\text{Se}_y$ ($y \sim 0.33$) [38, 39]. Moreover, the same FS was recorded for different specimens (for a number of measured samples two possible orientations would be observed if orthorhombic distortion took place). Finally, in the case of orthorhombic distortion the signal would usually originate from two domain

orientations in a usually twinned crystal, and ARPES spectra would be a superposition of these.

The ARPES data are in qualitative agreement with the results of DFT calculations, which predicted that Co or Ni doping in FeSe results in considerable expansion of the electron FS volume and a reduction of the hole FS volume [40]. The different shape of electron pockets at \bar{M} for Ni and Co doping is a symptom of the non-rigid band shift in the studied system. The nature of this difference is not understood so far.

The effect of doping on the region of the $\bar{\Gamma}$ point is visualized in figure 2, which presents ARPES spectra taken along line 1 ($\bar{M} - \bar{\Gamma} - \bar{M}$ direction) shown in figures 1(c)–(f). The band structure along $\bar{M} - \bar{\Gamma} - \bar{M}$ for $\text{Fe}_{1.01}\text{Te}_{0.67}\text{Se}_{0.33}$ reveals three hole pockets at $\bar{\Gamma}$ (figure 2(a)), which agrees with the previous ARPES results for this system [41–44]. However, we have detected neither an electron band nor Dirac cones, which have been observed in a system with higher Se content ($\text{FeTe}_{0.55}\text{Se}_{0.45}$) in a laser ARPES study [35]. These features were well resolved in the experimental geometry corresponding to π polarization [35]. The raw ARPES data for Co- and Ni-doped samples (figures 2(b)–(d)) show only two inner hole pockets. Fermi–Dirac normalized spectra (figures 2(e)–(h)) reveal the same pockets as the raw data. However, the calculated 2D curvature [45] (figures 2(i)–(l)) recovers three hole bands for all the investigated systems. Dispersions of β pockets were estimated by means of fitting the Gauss function to both MDCs and energy distribution curves (EDCs) from the data normalized by the Fermi–Dirac distribution (figures 2(e)–(h)). In the case of the doped samples, parabolas were fitted to β pockets (figures 2(b)–(d), (f)–(h)). Dispersions of α and γ pockets are presented as indicative lines corresponding to the maxima in the 2D curvature plots.

It is clear that the β band, which forms part of the FS of the undoped system, is shifted below the Fermi energy (E_F) for all the doped samples (figure 2(m)). The situation of the α pocket is less clear. However, it is visible that electron doping moves this band down and changes the slope. For the undoped sample the α band may participate in FS but according to the found dispersions it should also be removed by doping. The data indicate that the γ pocket survives the electron doping. The removal of β and probably α pockets changes the topology of FS, which is interpreted as a Lifshitz transition. This sheds new light on the peculiar behavior of R_H [15], which first increases with Ni or Co doping and then becomes negative for low-temperature data. The disappearance of β and probably α hole pockets decreases the hole FS volume and reduces the number of holes in the system. In parallel, the volume of electron pockets, which is proportional to electron band filling, grows with doping. Such evolution of the FS leads to a negative R_H . In fact, R_H for $\text{Fe}_{0.94}\text{Co}_{0.09}\text{Te}_{0.67}\text{Se}_{0.33}$ and $\text{Fe}_{0.97}\text{Ni}_{0.05}\text{Te}_{0.65}\text{Se}_{0.35}$ is still positive for all temperatures but these systems are located close to the dopant concentration, for which low-temperature R_H changes sign. It is already negative for $\text{Fe}_{0.91}\text{Ni}_{0.11}\text{Te}_{0.65}\text{Se}_{0.35}$ at low temperature. ARPES data also explain the fact that R_H remains positive for all doping levels at room temperature. The tops of the β pocket are located at 26, 29 and 37 meV binding energy for $\text{Fe}_{0.94}\text{Co}_{0.09}\text{Te}_{0.67}\text{Se}_{0.33}$, $\text{Fe}_{0.97}\text{Ni}_{0.05}\text{Te}_{0.65}\text{Se}_{0.35}$ and

$\text{Fe}_{0.91}\text{Ni}_{0.11}\text{Te}_{0.65}\text{Se}_{0.35}$, respectively. At room temperature such binding energies are accessible for thermal scattering, which includes the β band in FS effectively, delivering more hole carriers.

It is noteworthy that the β band has a parabolic shape when it does not participate in FS. For $\text{Fe}_{1.01}\text{Te}_{0.67}\text{Se}_{0.33}$ its dispersion near E_F is strongly modified. The effective mass calculated with formula $m(E) = \hbar^2 k(E) dk/dE$ (figure 2(n)) appears to be strongly reduced with lowering energy, whereas it is constant for parabolic dispersions of the doped systems. This visualizes correlation effects, which strongly influence the dispersion near E_F . Previously, a qualitatively similar effect was observed for $\text{NaFe}_{0.978}\text{Co}_{0.022}\text{As}$ [46], and it was attributed to orbital mixing caused by strong spin–orbit coupling.

The electron pockets observed along lines 2 from figure 1 are shown in figure 3. Only one pocket is resolved in both the raw data (figures 3(a)–(d)) and 2D curvature plots (figures 3(e)–(h)). The dispersion was determined by fitting MDCs, and it also agrees with the maxima in the 2D curvature plots. Electron bands follow the parabolas well with no considerable correlation effects, which would be reflected in a more complex shape. The changes in the binding energies for both electron and β hole bands as well as the corresponding effective masses are presented in table 1. The binding energy shifts of hole and electron pockets are similar for $\text{Fe}_{0.94}\text{Co}_{0.09}\text{Te}_{0.67}\text{Se}_{0.33}$ and $\text{Fe}_{0.91}\text{Ni}_{0.11}\text{Te}_{0.65}\text{Se}_{0.35}$, which would roughly indicate a rigid band shift. The shifts determined for $\text{Fe}_{0.97}\text{Ni}_{0.05}\text{Te}_{0.65}\text{Se}_{0.35}$ contradict this thesis.

Effective masses (m^*) can be easily estimated for bands with a parabolic shape (table 1). The β band at the $\bar{\Gamma}$ point allows us to determine the effective mass to be between $3.2 m_e$ and $2.5 m_e$. We do not show m^* for the undoped sample, which is not constant but decreases with energy. For the electron band at the \bar{M} point, m^* grows with the amount of electrons delivered by Co or Ni, which means that correlations are enhanced there with electron doping.

Co and Ni doping has a direct effect on band filling. The increase of FS volume for the electron pocket is given in figure 4(a). The results in this figure are normalized per doped electron, i.e. we assume that Co donates one extra electron and Ni delivers two. If we postulate linear trends to compare the effects of doping quantitatively, the increase in the number of states filled by electrons is 5% higher for Co substitution. Band shifts (figure 4(b)) resulting from doping seem to be larger for Co and by assuming linear dependencies we can estimate that the efficiency of transferring electrons is about 40% higher when compared to Ni. However, this is FS volume, which is more directly related to the number of doped carriers. The shape of the electron pocket, which is circular or elliptical depending on the dopant, points to a non-rigid band shift in the system. In such a case it is more difficult to compare band shifts for Ni- and Co-doped compounds. Despite a relatively lower effect of doping Ni causes stronger suppression of superconductivity and a more pronounced effect on transport properties [15]. First of all, more efficient impurity scattering was predicted for Ni [47]. Moreover, it is known that Co and Ni doping may have a

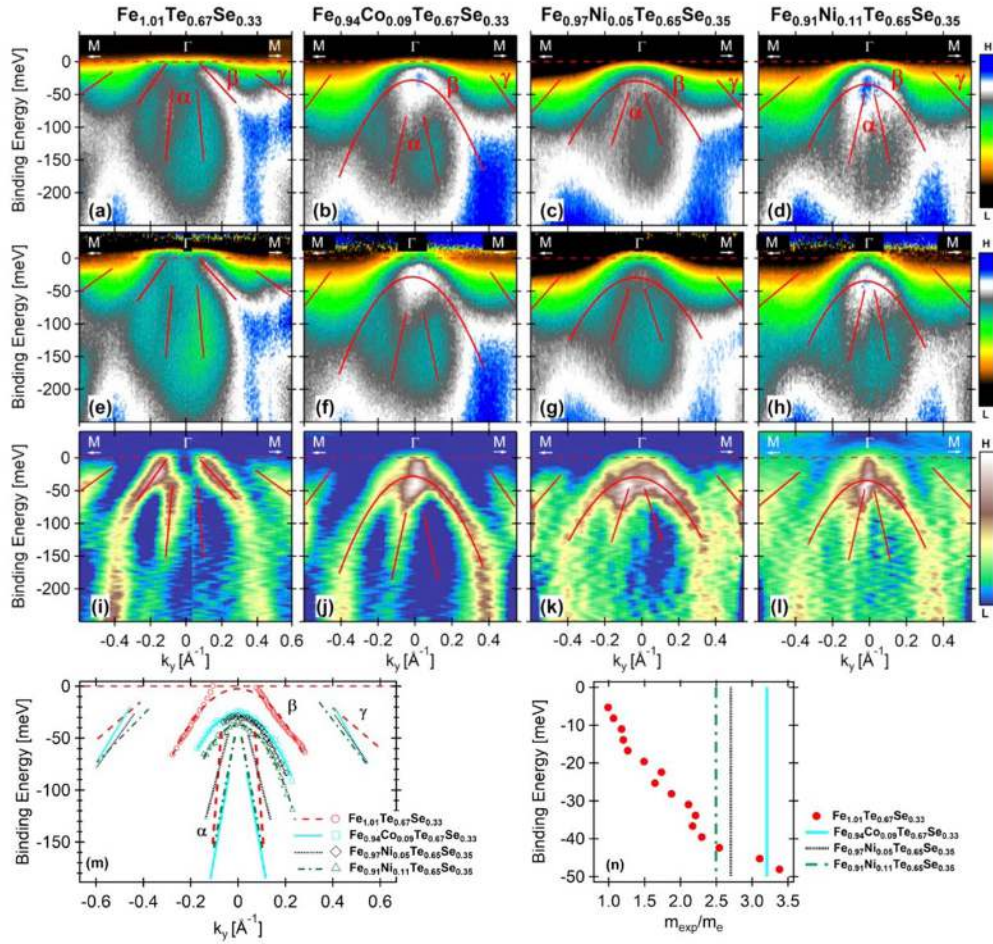


Figure 2. Band structure of $\text{Fe}_{1-x}\text{M}_x\text{Te}_{1-y}\text{Se}_y$ ($\text{M}=\text{Co}, \text{Ni}$, $y \sim 0.35$) systems in the region of the Γ point obtained by ARPES at $T = 18$ K. The measurements were performed in $\bar{M} - \Gamma - \bar{M}$ direction along paths marked with 1 in figures 1(c)–(f). Raw data: (a) $\text{Fe}_{1.01}\text{Te}_{0.67}\text{Se}_{0.33}$, (b) $\text{Fe}_{0.94}\text{Co}_{0.09}\text{Te}_{0.67}\text{Se}_{0.33}$, (c) $\text{Fe}_{0.97}\text{Ni}_{0.05}\text{Te}_{0.65}\text{Se}_{0.35}$, (d) $\text{Fe}_{0.91}\text{Ni}_{0.11}\text{Te}_{0.65}\text{Se}_{0.35}$. (e)–(h) Spectra from (a)–(d) normalized by the Fermi-Dirac distribution. (i)–(l) 2D curvature plots [45] obtained for the spectra shown in (a)–(d). (m) Hole band dispersions, experimental points were estimated from MDC and EDC fitting to the spectra. Parabolas obtained from MDC and EDC maxima fitting are shown. Dispersions of α and γ bands are indicated by maxima in the 2D curvature plots. (n) Effective mass for β band expressed in free electron masses. In the case of $\text{Fe}_{1.01}\text{Te}_{0.67}\text{Se}_{0.33}$ the effective mass appears to be energy-dependent, and for the doped systems parabolic dispersion yields constant m^* .

different influence on the correlations in the system [31, 34], which have an impact on superconductivity as well. Our data, which reveal less effective electron doping of Ni, confirm that stronger correlation effects must take place in samples with this element. $\text{Fe}_{1-x}\text{M}_x\text{Te}_{1-y}\text{Se}_y$ ($y \sim 0.35$) may be considered as a 2D system to some extent. For a purely 2D system with weak correlations, i.e. with parabolic dispersions in two dimensions, a rigid band shift should result in a proportional increase of band filling and band shift. This assumption is not convergent with our results. Finally, a rigid band shift predicted by DFT calculations for 10% of Co or 5% of Ni in FeSe [40] should amount to 70 meV, which is much larger than the value of ~ 25 meV found in our experiment.

The experimental data for the undoped $\text{Fe}_{1.01}\text{Te}_{0.67}\text{Se}_{0.33}$ can be compared to APW+lo calculations performed for stoichiometric FeTe (figure 5). The calculated FSs are shown along the Γ -M-X or Z-A-R planes. In both cases theoretical FSs have much larger volume as compared to experimental ones. In other words the results indicate shrinking of the FS (figures 5(a) and (b)), which was explained previously as originating from interband scattering [48]. It appears that calculations performed along \bar{M} - Γ - \bar{M} are more consistent with experimental data for $\bar{M} - \Gamma - \bar{M}$ than those obtained along A-Z-A. This indicates that the experimental band structure collected at $h\nu = 21.218$ eV corresponds rather to the Γ point crossing (or its vicinity) at normal emission.

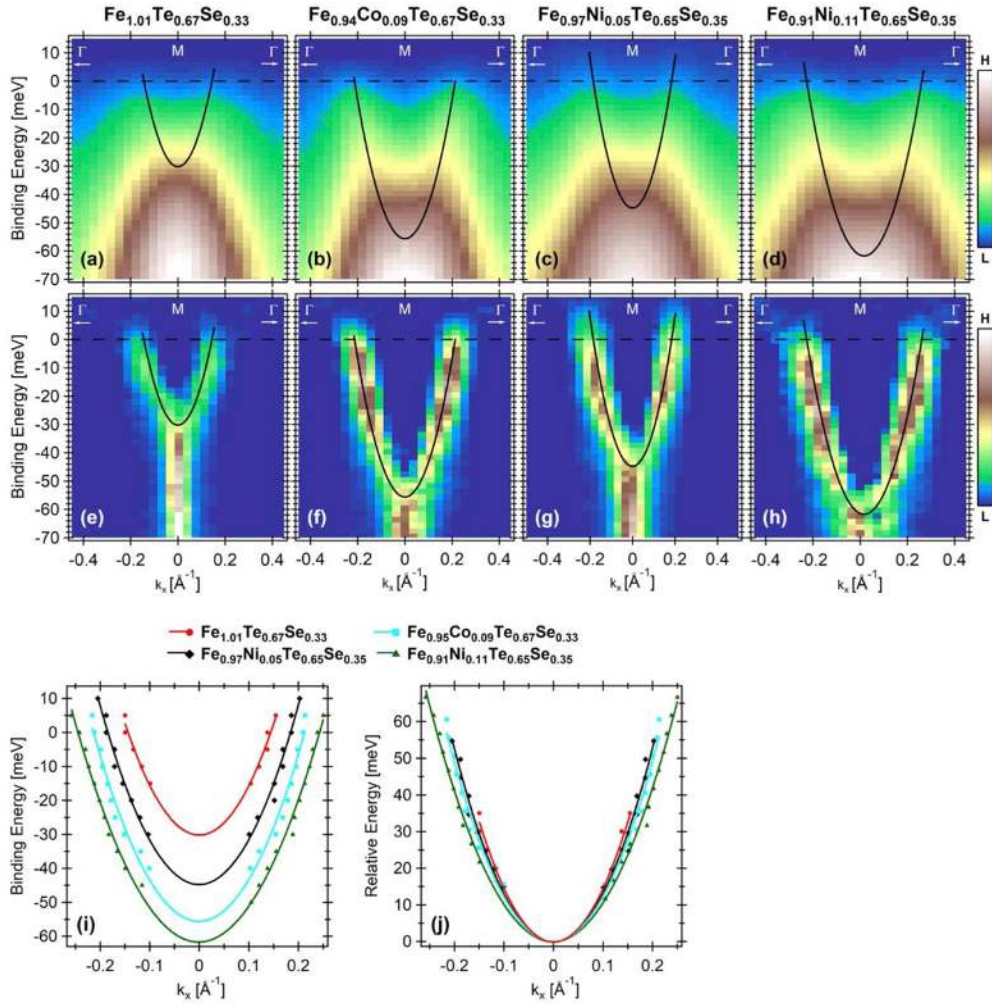


Figure 3. Band structure of $\text{Fe}_{1-x}\text{M}_x\text{Te}_{1-y}\text{Se}_y$ ($M=\text{Co}, \text{Ni}$, $y\sim 0.35$) systems in the region of the \bar{M} point obtained by ARPES at $T = 18$ K. The measurements were performed along paths marked with '2' in figure 1(c)–(f). Raw data are shown for (a) $\text{Fe}_{1.01}\text{Te}_{0.67}\text{Se}_{0.33}$, (b) $\text{Fe}_{0.94}\text{Co}_{0.09}\text{Te}_{0.67}\text{Se}_{0.33}$, (c) $\text{Fe}_{0.97}\text{Ni}_{0.05}\text{Te}_{0.65}\text{Se}_{0.35}$, (d) $\text{Fe}_{0.91}\text{Ni}_{0.11}\text{Te}_{0.65}\text{Se}_{0.35}$. (e)–(h) present 2D curvature plots [45] corresponding to data from (a)–(d). Black solid lines represent parabolas fitted to maxima of MDCs. The fitted parabolic dispersions with MDC maxima are shown in (i). The same dispersions with shifts in energy leading to an overlap of the bottom of the band (j).

Table 1. Energy shifts of β hole pockets and the electron pockets at $k_y = 1.2 \text{ \AA}^{-1}$ and corresponding effective masses expressed in free electron mass.

Compound	β hole pocket		Electron pocket	
	Band shift [meV]	Effective mass [m_e]	Band shift [meV]	Effective mass [m_e]
$\text{Fe}_{1.01}\text{Te}_{0.67}\text{Se}_{0.33}$	0	—	0	2.6(3)
$\text{Fe}_{0.94}\text{Co}_{0.09}\text{Te}_{0.67}\text{Se}_{0.33}$	23(1)	3.2(2)	25(3)	3.1(2)
$\text{Fe}_{0.97}\text{Ni}_{0.05}\text{Te}_{0.65}\text{Se}_{0.35}$	26(1)	2.7(1)	14(3)	2.8(2)
$\text{Fe}_{0.91}\text{Ni}_{0.11}\text{Te}_{0.65}\text{Se}_{0.35}$	35(1)	2.5(1)	32(3)	3.7(1)

Theoretical dispersions are compared with the experimental ones, with a renormalization factor of 1, 1 and 5, as well as energy shifts of 70 meV, 92 meV and -110 meV for α , β and γ pockets, respectively. These results are in qualitative agreement with a previous study for $\text{FeTe}_{0.5}\text{Se}_{0.5}$ [34], where the γ pocket also appeared to be highly renormalized. The electron pocket observed at the \bar{M} point agrees with theory for the renormalization factor of 1.6 with energy shift of 0.08 eV (figure 5(d)).

The FS topology should be analyzed in terms of possible scattering between hole and electron pockets. For the superconducting $\text{Fe}_{1.01}\text{Te}_{0.67}\text{Se}_{0.33}$ system the radius of β and γ

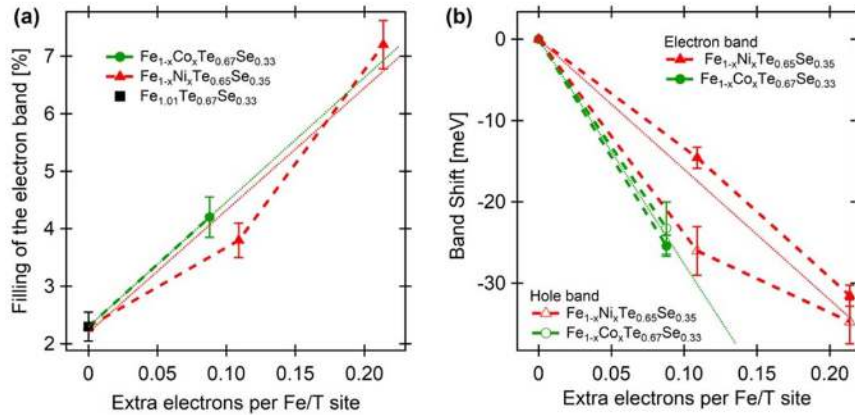


Figure 4. Effect of doping on band structure of $\text{Fe}_{1-x}\text{M}_x\text{Te}_{1-y}\text{Se}_y$ ($\text{M}=\text{Co}, \text{Ni}$, $y \sim 0.35$) estimated from ARPES as a function of a nominal amount of doped electrons assuming that Co and Ni donate one and two extra electrons, respectively. (a) Filling of the electron band determined from the area of solid black ovals in figures 1(c)–(f). (b) Band shifts estimated from the electron band (figure 3) and β hole band (figure 2) dispersions. The dotted lines show average effect of doping (fitted line), the dashed lines connect points.

hole pockets expressed in Γ – \bar{M} distance is roughly estimated as 0.075 and 0.23, respectively. The α pocket is somewhat smaller than β . On the other hand the radius of the estimated electron pocket at \bar{M} amounts to 0.11 in the same units. Hence, the difference in radii between the electron pocket and either β or γ hole pockets is ~ 0.037 and 0.12, respectively. As a result of Co/Ni doping these values will grow. Then, it is concluded that for superconducting $\text{Fe}_{1.01}\text{Te}_{0.67}\text{Se}_{0.33}$ there is a considerable deviation from perfect nesting due to the mismatch between electron and hole pockets. Earlier, it was proposed that such a marginal breakdown of nesting would support the appearance of spin fluctuations as perfect nesting would rather induce a spin density wave [6]. Here, we can compare our results to corresponding mismatch in nesting obtained by DMFT and ARPES for $(\text{Li},\text{Na})\text{FeAs}$ [6]. The digitalization of the data from figure 2(c) from [6] yielded that the average difference in radii between a hole and corresponding (i.e. with the lowest mismatch) electron pocket is 0.08 and 0.10 Γ – \bar{M} distance for β and γ , respectively. The first value is much larger than in the case of $\text{Fe}_{1.01}\text{Te}_{0.67}\text{Se}_{0.33}$. However, a general rule that imperfect nesting supports superconductivity should also hold for Fe-11 systems.

It is interesting to compare the effect of Co doping on the band structure of a superconductor from the Fe-122 family, namely $\text{Ba}(\text{Fe}_{1-x}\text{Co}_x)_2\text{As}_2$ [26–28, 31] and $\text{Fe}_{1-x}\text{Co}_x\text{Te}_{0.67}\text{Se}_{0.33}$ from this study, which represents Fe-11 systems. The increasing amount of Co in $\text{Ba}(\text{Fe}_{1-x}\text{Co}_x)_2\text{As}_2$ first destroys the magnetic order, and then induces superconductivity, which is further suppressed in the overdoped region. In contrast, the only role of Co in $\text{Fe}_{1-x}\text{Co}_x\text{Te}_{0.67}\text{Se}_{0.33}$ is the suppression of superconductivity. The FS of underdoped $\text{Ba}(\text{Fe}_{1-x}\text{Co}_x)_2\text{As}_2$ contains characteristic ‘flower petals’ around the M point (according to convention in the quoted paper it is denoted as X) in the antiferromagnetic phase. These structures are absent for $\text{Fe}_{1-x}\text{Co}_x\text{Te}_{0.67}\text{Se}_{0.33}$. However, for higher Co content in Fe-122 the analogy to Fe-11 is found. The FS of the optimally doped $\text{Ba}(\text{Fe}_{1-x}\text{Co}_x)_2\text{As}_2$ is analogous to $\text{FeTe}_{1-y}\text{Se}_y$ ($y \sim 0.35$). In both

cases, hole and electron pockets have similar volumes and a situation close to nesting takes place for these parts of the FS. This imperfect nesting is removed with further Co doping in Fe-122 and Fe-11. In both highly doped systems the FS with large electron pockets at \bar{M} and small or removed pockets at Γ has no more nesting properties. It should be stressed that nesting is removed faster in Ni-doped $\text{Fe}_{1-x}\text{Ni}_x\text{Te}_{0.65}\text{Se}_{0.35}$ samples, where electron pockets become elliptical. It is noteworthy that we did not observe electron pockets, which appear at Γ in highly doped $\text{Ba}(\text{Fe}_{1-x}\text{Co}_x)_2\text{As}_2$ [27, 28].

4. Conclusions

ARPES studies revealed clear evidence of electron doping on the band structure of the $\text{FeTe}_{1-y}\text{Se}_y$ ($y \sim 0.35$) superconductor, which is an effect of Co or Ni substitution for iron. This is reflected in the comparable shifts of both hole and electron pockets. The electron FS volume increases, while a part of the hole FS disappears, which is a realization of Lifshitz transition. The efficiency of electron doping is higher for Co, with a 5% higher rate of filling electron pocket and 40% larger band shifts, if one assumes that Ni should yield twice as many carriers as Co. Therefore, the more remarkable influence of Ni on transport properties and significant suppression of superconductivity observed before [15] must definitely be attributed to the more effective impurity scattering for Ni and strong correlation effects but not the contribution of carrier doping. The elliptical shape of electron pockets appears as an effect of Ni doping, while it is not observed for Co substitution. This fact, together with the effective mass growth at the \bar{M} point with doping, the considerable reduction of m^* in the undoped β hole pocket near E_F , and the large difference in band shifts for the comparable increase of band fillings for Co and Ni dopants, indicates that there are deviations from the rigid band shift scenario. While a clear departure from perfect FS nesting

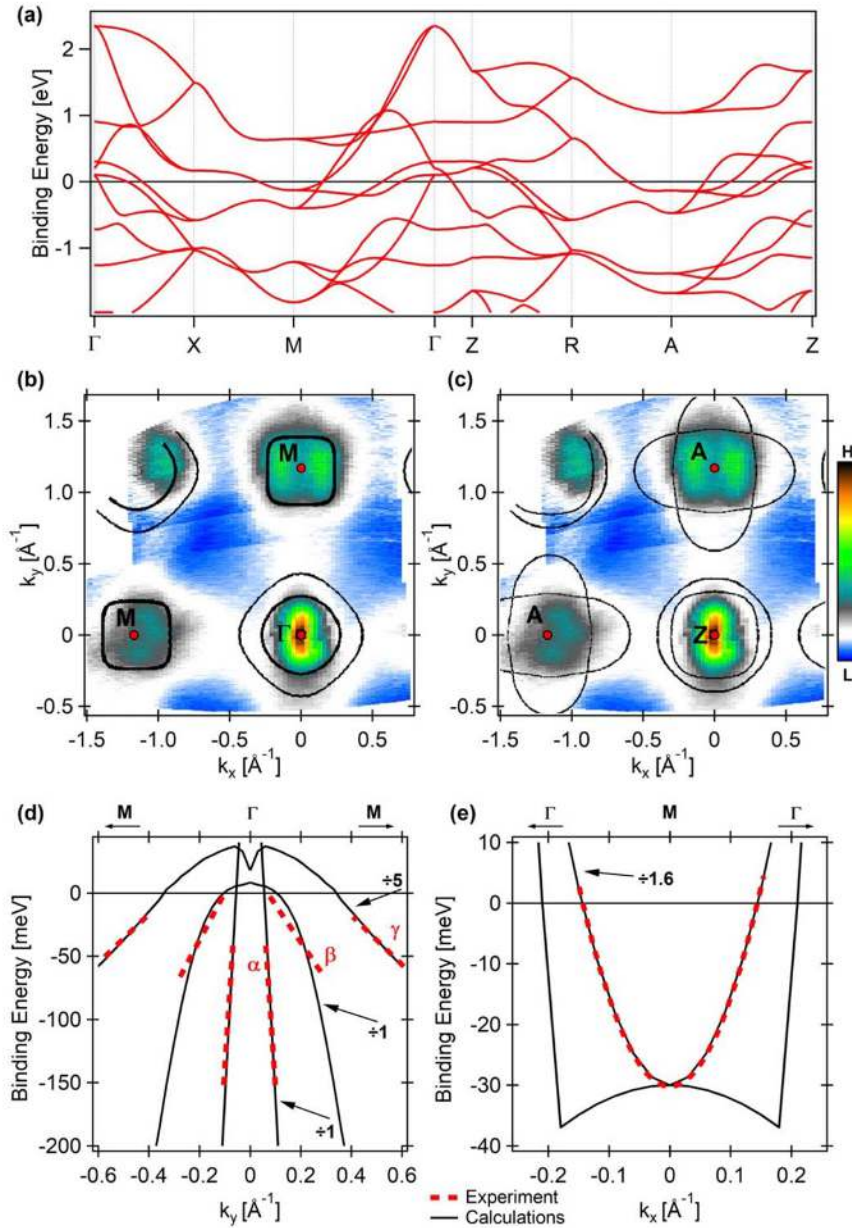


Figure 5. (a) Band structure of FeTe obtained with APW-*lo* calculations. The theoretical FS (black solid lines) along (b) Γ -M-X plane and (c) Z-A-R plane is superimposed on experimental FS map for $\text{Fe}_{1.01}\text{Te}_{0.67}\text{Se}_{0.33}$. (d,e) Comparison between theoretical (black solid lines) and experimental (red dotted lines) dispersions along M- Γ -M direction at (d) Γ and (e) M point. Theoretical binding energies for α , β and γ bands were shifted by 70 meV, 92 meV and -110 meV and divided by 1, 1 and 5, respectively. The theoretical binding energy for electron pocket (e) had to be divided by 1.6 after being shifted by 80 meV.

between hole and electron pockets is observed for the $\text{FeTe}_{1-y}\text{Se}_y$ ($y \sim 0.35$) superconductor, the sizes of these pockets diverge further with Co or Ni doping. Such FS evolution is analogous to overdoped $\text{Ba}(\text{Fe}_{1-x}\text{Co}_x)_2\text{As}_2$, which may indicate that Co/Ni-doped Fe-11 should be considered as an overdoped system.

Acknowledgments

Support of the Polish Ministry of Science and Higher Education under grant 7150/E-338/M/2018 is acknowledged. The work was supported by Polish NSC Grant No. 2014/15/B/ST3/03889.

ORCID iDs

M Rosmus  <https://orcid.org/0000-0002-4314-9601>
 R Kurlito  <https://orcid.org/0000-0002-4749-1084>
 D J Gawryluk  <https://orcid.org/0000-0003-4460-7106>
 J Goraus  <https://orcid.org/0000-0002-7711-727X>
 M Z Cieplak  <https://orcid.org/0000-0001-7513-3973>
 P Starowicz  <https://orcid.org/0000-0002-9514-0254>

References

- [1] Kamihara Y, Watanabe T, Hirano M and Hosono H 2008 *JACS* **130** 3296
- [2] Stewart G R 2011 *Rev. Mod. Phys.* **83** 1589
- [3] Chen X, Dai P, Feng D, Xiang T and Zhang F-C 2014 *NSR* **1** 371
- [4] Si Q, Yu R and Abrahams E 2016 *Nat. Rev. Mater.* **1** 16017
- [5] Ye Z R et al 2014 *Phys. Rev. X* **4** 031041
- [6] Lee G et al 2012 *Phys. Rev. Lett.* **109** 177001
- [7] Sefat A S, Jin R, McGuire M A, Sales B C, Singh D J and Mandrus D 2008 *Phys. Rev. Lett.* **101** 117004
- [8] Leithe-Jasper A, Schnelle W, Geibel C and Rosner H 2008 *Phys. Rev. Lett.* **101** 207004
- [9] Li J et al 2009 *New J. Phys.* **11** 025008
- [10] Sefat A S, Huq A, McGuire M A, Jin R, Sales B C, Mandrus D, Cranswick L M D, Stephens P W and Stone K H 2008 *Phys. Rev. B* **78** 104505
- [11] Wang C et al 2009 *Phys. Rev. B* **79** 054521
- [12] Cao G et al 2009 *Phys. Rev. B* **79** 174505
- [13] Shipra R, Takeyab H, Hiratab K and Sundaresan A 2010 *Physica C* **470** 528
- [14] Gawryluk D J, Fink-Finowicki J, Wiśniewski A, Puźniak R, Domukhovski V, Diduszko R, Kozłowski M and Berkowski M 2011 *Supercond. Sci. Technol.* **24** 065011
- [15] Bezusyy V L, Gawryluk D J, Malinowski A and Cieplak M Z 2015 *Phys. Rev. B* **91** 100502
- [16] Kumar A, Tandon R P and Awana V P S 2012 *IEEE T. Magn.* **48** 4239
- [17] Nabeshima F, Kobayashi Y, Imai Y, Tsukada I and Maeda A 2012 *Jpn. J. Appl. Phys.* **51** 010102
- [18] Zhang Z T, Yang Z R, Li L, Ling L S, Zhang C J, Pi L and Zhang Y H 2013 *J. Phys.: Condens. Matter* **25** 035702
- [19] Inabe T, Kawamata T, Noji T, Adachi T and Koike Y 2013 *J. Phys. Soc. Jpn.* **82** 044712
- [20] Wadati H, Elfimov I and Sawatzky G A 2010 *Phys. Rev. Lett.* **105** 157004
- [21] Kemper A F, Cao C, Hirschfeld P J and Cheng H-P 2009 *Phys. Rev. B* **80** 104511
- [22] Berlijn T, Lin C-H, Garber W and Ku W 2012 *Phys. Rev. Lett.* **108** 207003
- [23] Bittar E M, Adriano C, Garitezi T M, Rosa P F S, Mendonça-Ferreira L, Garcia F, de M Azevedo G, Pagliuso P G and Granado E 2011 *Phys. Rev. Lett.* **107** 267402
- [24] Levy G et al 2012 *Phys. Rev. Lett.* **109** 077001
- [25] Sekiba Y et al 2009 *New J. Phys.* **11** 025020
- [26] Brouet V, Marsi M, Mansart B, Nicolaou A, Taleb-Ibrahimi A, Le Fèvre P, Bertran F, Rullier-Albenque F, Forget A and Colson D 2009 *Phys. Rev. B* **80** 165115
- [27] Liu C et al 2010 *Nat. Phys.* **6** 419
- [28] Liu C et al 2011 *Phys. Rev. B* **84** 020509(R)
- [29] Neupane M et al 2011 *Phys. Rev. B* **83** 094522
- [30] Ideta S et al 2013 *Phys. Rev. Lett.* **110** 107007
- [31] Vilmercati P et al 2016 *Phys. Rev. B* **94** 195147
- [32] Malaeb W et al 2009 *J. Phys. Soc. Jpn.* **78** 123706
- [33] Miao H et al 2015 *Nat. Commun.* **6** 6056
- [34] Thirupathiah S, Fink J, Maheshwari P K, Ravi Kishore V V, Liu Z-H, Rienks E D L, Büchner B, Awana V P S and Sarma D D 2016 *Phys. Rev. B* **93** 205143
- [35] Zhang P et al 2018 *Science* **360** 182
- [36] Results obtained using the Elk code: <http://elk.sourceforge.net/>
- [37] Brouet V, Jensen M F, Lin P-H, Taleb-Ibrahimi A, Le Fèvre P, Bertran F, Lin C-H, Ku W, Forget A and Colson D 2012 *Phys. Rev. B* **86** 075123
- [38] Horigane K, Hiraka H and Ohoyama K 2009 *J. Phys. Soc. Jpn.* **78** 074718
- [39] Prokeš K et al 2015 *J. Cryst. Growth* **432** 95
- [40] Ciechan A, Winiarski M J and Samsel-Czekala M 2013 *Intermetallics* **41** 44
- [41] Chen F et al 2010 *Phys. Rev. B* **81** 014526
- [42] Tamai A et al 2010 *Phys. Rev. Lett.* **104** 097002
- [43] Nakayama K et al 2010 *Phys. Rev. Lett.* **105** 197001
- [44] Ieki E et al 2014 *Phys. Rev. B* **89** 140506
- [45] Zhang P, Richard P, Qian T, Xu Y-M, Dai X and Ding H 2011 *Rev. Sci. Instruments* **82** 043712
- [46] Charnukha A et al 2016 *Sci. Rep.* **6** 18620
- [47] Herbig A, Heid R and Schmalian J 2016 *Phys. Rev. B* **94** 094512
- [48] Ortenzi L, Cappelluti E, Benfatto L and Pietronero L 2009 *Phys. Rev. Lett.* **103** 046404

Effect of electron doping in $\text{FeTe}_{1-y}\text{Se}_y$ realized by Co and Ni substitution

Supplementary material; Sample preparation and characterisation

M. Rosmus¹, R. Kurlito¹, D. J. Gawryluk^{2,3}, J. Goraus⁴, M. Z. Cieplak³, and P. Starowicz¹

¹ *M. Smoluchowski Institute of Physics, Jagiellonian University, Łojasiewicza 11, 30-348, Kraków, Poland*

² *Laboratory for Multiscale Materials Experiments, Paul Scherrer Institut, 5232 Villigen PSI, Switzerland*

³ *Institute of Physics, Polish Academy of Sciences, Lotników 32/46, 02-668 Warszawa, Poland*

⁴ *Institute of Physics, University of Silesia, Uniwersytecka 4, 40-007 Katowice, Poland*

Single crystal growth

Growth conditions of $\text{Fe}_{1-x}\text{ME}_x\text{Te}_{1-y}\text{Se}_y$ single crystals can be found elsewhere [1]. The single crystals with composition $\text{Fe}_{1.01}\text{Te}_{0.67}\text{Se}_{0.33}$, $\text{Fe}_{0.94}\text{Co}_{0.09}\text{Te}_{0.67}\text{Se}_{0.33}$, $\text{Fe}_{0.97}\text{Ni}_{0.05}\text{Te}_{0.65}\text{Se}_{0.35}$ and $\text{Fe}_{0.91}\text{Ni}_{0.11}\text{Te}_{0.65}\text{Se}_{0.35}$ (nominal composition were $\text{FeTe}_{0.65}\text{Se}_{0.35}$, $\text{Fe}_{0.90}\text{Co}_{0.1}\text{Te}_{0.65}\text{Se}_{0.35}$, $\text{Fe}_{0.95}\text{Ni}_{0.05}\text{Te}_{0.65}\text{Se}_{0.35}$, and $\text{Fe}_{0.91}\text{Ni}_{0.11}\text{Te}_{0.65}\text{Se}_{0.35}$) were grown by applying Bridgman's method. Stoichiometric amounts of appropriate starting reagents (Fe_3N_5 , $\text{NiSe } 2\text{N}^+$, $\text{Co } 5\text{N}$, $\text{Te } 4\text{N}$, and $\text{Se } 2\text{N}$) were placed into a double wall quartz ampule, evacuated ($9.32 \cdot 10^{-5}$ Pa) and sealed. Inner diameter of the Bridgman ampule was equal to 6 mm. To avoid any contamination from the environment the starting elements were handled in an argon-filled glove-box. The sealed ampoules were placed in a furnace with an average vertical gradient of temperature of about 1.1 °C/mm. After melting at 865-880°C (depending on the composition) the temperature was held for 3 h, then reduced slowly to 490-450°C at a rate of 1-1.5°C/h and finally cooled down with a rate 60°C/h to room temperature.

Physical properties characterisation

Phase purity was checked at room temperature by powder x-ray diffraction (PXRD) using Ni-filtered $\text{Cu K}\alpha$ radiation with a Bruker D8 or Siemens D5000 (nickel-doped samples). The reflections of a main $\text{Fe}_{1-x}\text{ME}_x\text{Te}_{1-y}\text{Se}_y$ (ME = Ni, Co) phase were indexed with a tetragonal cell in the space group $P4/nmm$ (No. 129). The whole-pattern decomposition (Profile Matching) analysis [2-4] of the diffraction patterns was performed by the FULLPROF SUITE package [4, 5] (version March-2019). Refined parameters were: scale factor, zero displacement, lattice parameters, and peak shape as a Thompson-Cox-Hastings pseudo-Voigt function. Due to the property of powdered crystals to have preferred orientation the correction in a form of a modified March's function ($\text{Fe}_{0.97}\text{Ni}_{0.05}\text{Te}_{0.65}\text{Se}_{0.35}$ and $\text{Fe}_{0.91}\text{Ni}_{0.11}\text{Te}_{0.65}\text{Se}_{0.35}$) or a March-Dollase multi-axial phenomenological model ($\text{Fe}_{1.01}\text{Te}_{0.67}\text{Se}_{0.33}$ and $\text{Fe}_{0.94}\text{Co}_{0.09}\text{Te}_{0.67}\text{Se}_{0.33}$) [6] were applied. Beside the formation of tetragonal $\text{Fe}_{0.94}\text{Co}_{0.09}\text{Te}_{0.67}\text{Se}_{0.33}$, we noticed a presence of a small amount of impurity phase (marked by * in the Fig. S1) after having the crystals pulverized. The Ni-doped crystal was crashed in a liquid nitrogen what caused poor crystallographic quality of the specimen. Each sample was oriented with Laue camera (Fig. S2). This confirmed good quality of the crystal used for the investigation by angle-resolved photoemission spectroscopy.

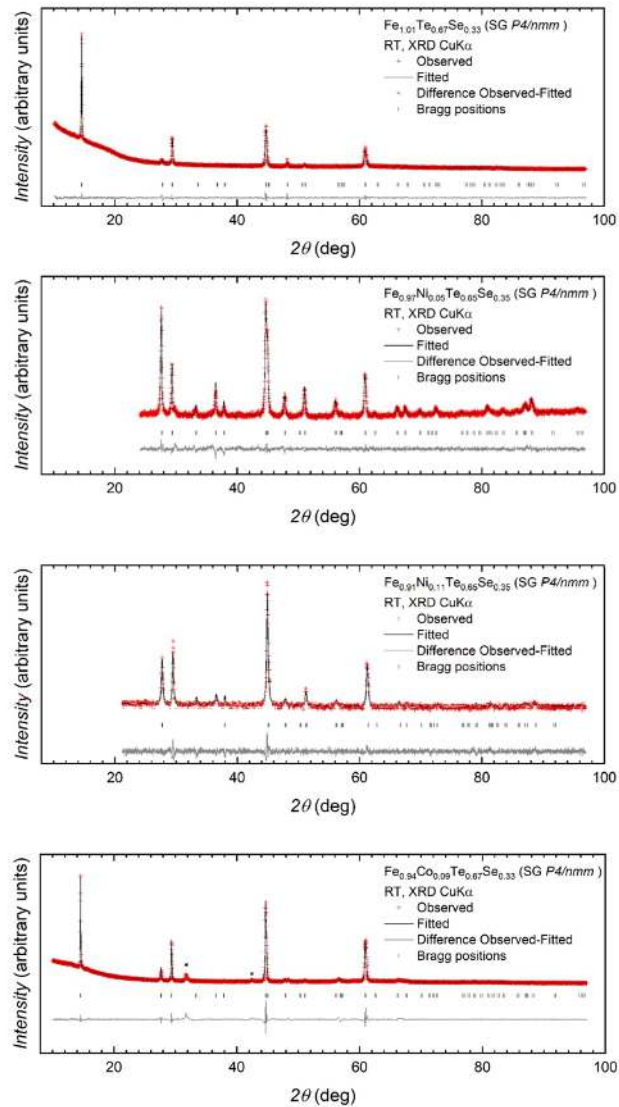


Fig. S1 X-Ray Diffraction ($Cu K\alpha$ radiation) pattern (red crosses) of $Fe_{1.01}Te_{0.67}Se_{0.33}$, $Fe_{0.97}Ni_{0.05}Te_{0.65}Se_{0.35}$, $Fe_{0.91}Ni_{0.11}Te_{0.65}Se_{0.35}$, and $Fe_{0.94}Co_{0.09}Te_{0.67}Se_{0.33}$ (SG $P4/nmm$ – No 129) obtained at room temperature. The black line corresponds to the best fit from the whole-pattern decomposition analysis. Lower vertical marks denote the Bragg peak positions for tetragonal phase of $Fe_{1-x}M_xTe_{1-y}Se_y$ (SG $P4/nmm$ – No 129). The bottom, gray line represents the difference between experimental and calculated points. Notice that due to the strong texture, spectrum for $Fe_{1.01}Te_{0.67}Se_{0.33}$ is mainly dominated by $(00l)$ and $(h0l)$ reflections family. Nevertheless, it shows that this is a pure phase specimen.

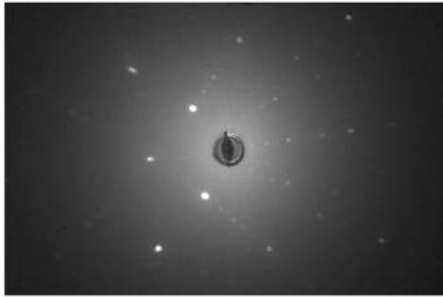


Fig. S2 Typical X-ray back-scattering Laue-reflection pattern for $Fe_{1.01}Te_{0.67}Se_{0.33}$ reveals good quality of the single crystal. A slight tilt of the c-axis is observed.

The quantitative point chemical composition analyses at the (001) cleavage plane of the crystal ingot were performed by Oxford INCA 250 energy dispersive X-ray spectroscopy (EDX) coupled with the JEOL JSM-7600F field emission (Schottky type) scanning electron microscope (FESEM), operating at 20 kV incident energy. EDX spectra, which are available in the supplement, have been used to determine precisely chemical content of the investigated $Fe_{1-x}ME_xTe_{1-y}Se_y$ single crystals (see Fig. S2).

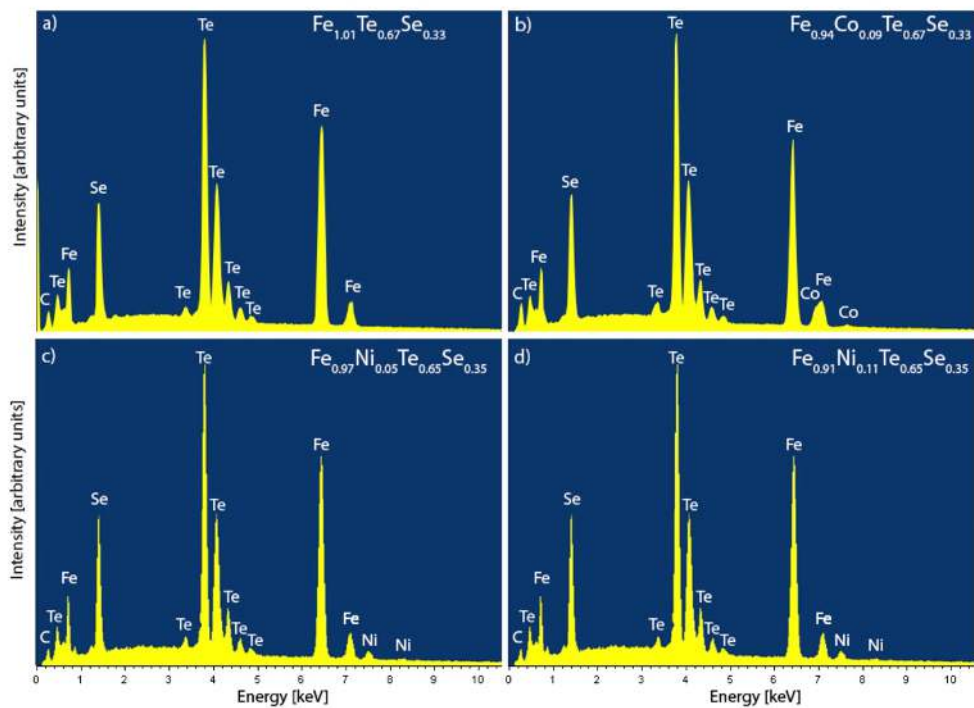


Fig. S3 Energy dispersive X-ray spectroscopy (EDX) collected on the cleavage planes of a) $Fe_{1.01}Te_{0.67}Se_{0.33}$, b) $Fe_{0.94}Co_{0.09}Te_{0.67}Se_{0.33}$, c) $Fe_{0.97}Ni_{0.05}Te_{0.65}Se_{0.35}$ and d) $Fe_{0.91}Ni_{0.11}Te_{0.65}Se_{0.35}$ single crystals.

The resistivity was measured in the *ab*-plane by a DC four-probe method with a physical property measurement system (PPMS) from Quantum Design (Fig. S4). Undoped crystal, $\text{Fe}_{1.01}\text{Te}_{0.67}\text{Se}_{0.33}$, shows the onset of the superconducting transition at $T_{c,\text{onset}} = 13.8$ K, the mid-point of the transition at $T_{c,\text{mid}} = 13.4$ K, and zero resistivity at $T_{R=0} = 12.7$ K. In case of the Co-doped crystal, $\text{Fe}_{0.94}\text{Co}_{0.09}\text{Te}_{0.67}\text{Se}_{0.33}$, the two higher transition points are at $T_{c,\text{onset}} = 4.6$ K, and $T_{c,\text{mid}} = 2.2$ K, respectively, while the zero resistivity is not observed above 2 K. The two Ni-doped samples: $\text{Fe}_{0.97}\text{Ni}_{0.05}\text{Te}_{0.65}\text{Se}_{0.35}$ and $\text{Fe}_{0.91}\text{Ni}_{0.11}\text{Te}_{0.65}\text{Se}_{0.35}$ are non-superconducting (above 2 K).

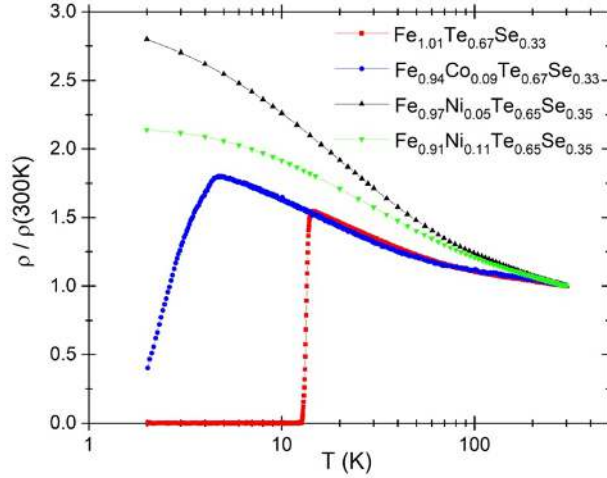


Fig. S4 Temperature dependence of the *ab*-plane resistivity normalized to the room temperature value, measured at zero magnetic field, for $\text{Fe}_{1.01}\text{Te}_{0.67}\text{Se}_{0.33}$, $\text{Fe}_{0.97}\text{Ni}_{0.05}\text{Te}_{0.65}\text{Se}_{0.35}$, $\text{Fe}_{0.91}\text{Ni}_{0.11}\text{Te}_{0.65}\text{Se}_{0.35}$, and $\text{Fe}_{0.94}\text{Co}_{0.09}\text{Te}_{0.67}\text{Se}_{0.33}$ single crystals.

The AC magnetic susceptibility was measured in 1 Oe of AC magnetic field with 10 kHz in a warming mode using PPMS (Fig. S5) for $\text{Fe}_{1.01}\text{Te}_{0.67}\text{Se}_{0.33}$, $\text{Fe}_{0.94}\text{Co}_{0.09}\text{Te}_{0.67}\text{Se}_{0.33}$, and $\text{Fe}_{0.97}\text{Ni}_{0.05}\text{Te}_{0.65}\text{Se}_{0.35}$ and systems. We define the temperature of the onset of superconductivity measured magnetically, $T_{c,\text{susc}}$, as the temperature at which the real component of the AC susceptibility starts to deviate from the high-temperature level, what indicates the beginning of the flux expulsion from the crystal. As shown by arrows in the figure, $T_{c,\text{susc}}$ is equal to 13.3 K and 9.5 K for $\text{Fe}_{1.01}\text{Te}_{0.67}\text{Se}_{0.33}$ and $\text{Fe}_{0.94}\text{Co}_{0.09}\text{Te}_{0.67}\text{Se}_{0.33}$ crystals, respectively, while no flux expulsion is observed in the $\text{Fe}_{0.97}\text{Ni}_{0.05}\text{Te}_{0.65}\text{Se}_{0.35}$ down to 2 K (crystals with larger Ni doping have not been studied since they show no signs of superconductivity in resistive measurements). We note that in the undoped crystal the $T_{c,\text{onset}}$ measured resistively is slightly higher than $T_{c,\text{susc}}$ measured magnetically. This is because the resistive measurement is sensitive to a first percolating path with zero resistance, which occurs at slightly higher temperature than the flux expulsion from the volume of the sample. On the other hand, in the Co-doped crystal $T_{c,\text{susc}}$ is twice as large as the $T_{c,\text{onset}}$. This may be explained by large inhomogeneity of doped crystal induced by impurity doping. In such inhomogeneous crystal the flux is expelled from locally superconducting volumes, but the percolating path with zero resistance is not created until much lower temperature.

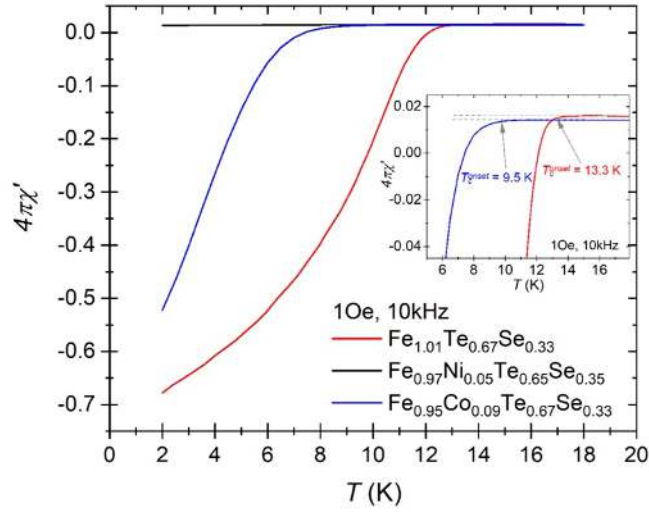


Fig. S5 Temperature dependence of real part of AC magnetic susceptibility measured in 1 Oe of AC field with 10 kHz in a warming mode for $\text{Fe}_{1.01}\text{Te}_{0.67}\text{Se}_{0.33}$, $\text{Fe}_{0.97}\text{Ni}_{0.05}\text{Te}_{0.65}\text{Se}_{0.35}$, and $\text{Fe}_{0.94}\text{Co}_{0.09}\text{Te}_{0.67}\text{Se}_{0.33}$ single crystals.

The Hall effect was studied for a series of samples with different content of Co and Ni by AC four-probe method using PPMS (Fig. S7). The Hall coefficient R_H is positive for low concentration of dopant and it increases with lowering of temperature. It is observed that the increase of the dopant concentration reduces R_H . At the higher level of doping, what is visible for Ni substituted samples, R_H becomes negative. The behaviour of R_H is similar to the case of $\text{Fe}_{1-x}\text{ME}_x\text{Te}_{1-y}\text{Se}_y$ (ME=Co, Ni) systems [7] obtained with a different procedure, namely with the fast cooling applied at the end of the crystallization process.

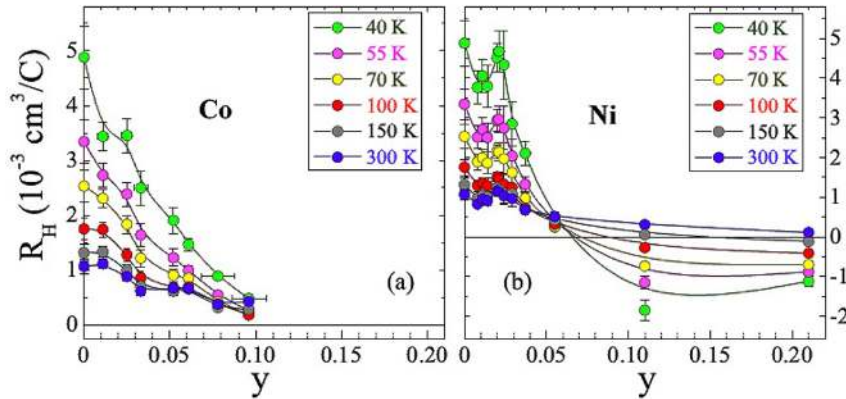


Fig. S6 Dopant concentration dependence of the Hall coefficient (R_H) for temperature points in range 40-300K for Co (a) and Ni (b) doped $\text{Fe}_{1.01}\text{Te}_{0.67}\text{Se}_{0.33}$ single crystals.

References

- [1] Gawryluk et al *Supercond. Sci. Technol.* 24 (2011) 065011
- [2] A. LeBail, H. Duroy and J.L. Fourquet, *Mat. Res. Bull.* 23, 447 (1988).
- [3] G.S. Pawley, *J. Applied Cryst.* 14, 357 (1981).
- [4] J. Rodríguez-Carvajal, *Physica B* 192, 55 (1993).
- [5] T. Roisnel, J. Rodríguez-Carvajal, *Proceedings of the Seventh European Powder Diffraction Conference (EPDIC 7)*, 2000, p.118-123.
- [6] N. G. Wright, R. J. Nelmes, S. A. Belmonte and M. I. McMahon, *J. Synchrotron Rad.* 3, 112 (1996).
- [7] V. L. Bezusyy, D. J. Gawryluk, A. Malinowski and M. Z. Cieplak, *Phys. Rev. B* 91, 100502(R) (2015).

5. Observation of Dirac Dispersions in Co-doped CaFe_2As_2

M. Rosmus, N. Olszowska, R. Kurlito, Z. Bukowski, P. Starowicz

I performed angle-resolved photoelectron spectroscopy (ARPES) measurements, with the help of N.O. and R.K. I prepared the samples for measurements by orientation using the Laue diffraction method. I analyzed the experimental data and developed the data processing code. I prepared the first draft of the manuscript and all the figures. I participated in the discussion and improvements of the manuscript together with P.S. My contribution to this work was 70%.

Observation of Dirac Dispersions in Co-doped CaFe_2As_2

Marcin Rosmus,^{1,2,*} Natalia Olszowska,² Rafał Kurlito,³ Zbigniew Bukowski,⁴ and Paweł Starowicz^{1,†}

¹*Marian Smoluchowski Institute of Physics, Jagiellonian University, Prof. S. Łojasiewicza 11, PL-30348 Kraków, Poland*

²*Solaris National Synchrotron Radiation Centre, Jagiellonian University, Czerwone Maki 98, 30-392 Kraków, Poland*

³*Department of Physics and Center for Experiments on Quantum Materials, University of Colorado, Boulder, Colorado 80309, USA*

⁴*Institute of Low Temperature and Structure Research, Polish Academy of Sciences, P.O. Box 1410, 50-950 Wrocław, Poland*

(Dated: June 4, 2023)

We performed an angle-resolved photoemission spectroscopy (ARPES) study of the electronic structure of CaFe_2As_2 , a parent compound, and two iron-based superconductors $\text{CaFe}_{2-x}\text{Co}_x\text{As}_2$ ($x=0.07$ and 0.15). We mapped the band structure of these compounds across the phase diagram with the transition from the orthorhombic antiferromagnetic phase to the tetragonal paramagnetic phase. We observed characteristic features of electronic structures corresponding to the spin density waves phase in the samples with low cobalt concentration and the concentric structure associated with superconducting iron-based compounds in highly doped samples. We reveal the existence of Dirac cones for the samples in the orthorhombic phase. According to the theoretical predictions [Ran, Y. et al, Physical Review 79, 1-9 (2009)] such cones are one of the characteristic features of the nodal spin density waves systems. However, other features, i.e., the existence of the energy gap and its modification due to cones, remain an open question.

I. INTRODUCTION

The discovery of superconductivity in iron-based compounds opened the way to a new chapter in superconductivity research. One of the most interesting families of these materials is so-called 122 family with the structure type of BaFe_2As_2 . It attracted the attention of researchers due to the rich phase diagram [1–3], the occurrence of structural transitions between the tetragonal paramagnetic phase (P) and the orthorhombic antiferromagnetic phase (AFM), and the possibility of studying the coexistence of spin-density waves and superconductivity. For a higher concentration of impurities (or a higher external pressure [4]), the AFM phase disappears, and the compound remains in the tetragonal phase for the entire temperature range; however, a significant shortening of the lattice constant c is observed, which is often called the transition to the collapsed tetragonal phase. The interesting thing is that superconductivity is observed in a wide range of diagram crossing through both the AFM and P regions. There are experimental works [5–12] reporting the existence of nontrivial topological states in the family of 122 compounds. The theoretical predictions suggest the existence of Dirac cones with the same chirality [13], furthermore theoretical calculations for this family of compounds [13, 14] show that the occurrence of Dirac states in this family is related to the physical symmetry and topology of the band structure, which stabilizes the ground state of the gapless spin density waves (SDWs) phase. To this day, to the best of the authors' knowledge, there are no reports on the observation of Dirac states in CaFe_2As_2 compound.

The main aim of this work was to study the electronic structure of the cobalt doped CaFe_2As_2 compound in

both antiferromagnetic and paramagnetic regions of the phase diagram. The measurements were performed for the samples with three different compositions: parent compound CaFe_2As_2 , lightly doped $\text{CaFe}_{1.93}\text{Co}_{0.07}\text{As}_2$ and heavily doped $\text{CaFe}_{1.85}\text{Co}_{0.15}\text{As}_2$. The lightly doped sample corresponds to the Co concentration for which the superconducting phase appears, while the heavily doped sample is in the paramagnetic superconducting phase. (Figure 1a). The parent compound crystallizes in the tetragonal $I4/mmm$ space group (No. 139) with lattice parameters $a = 3.89245(8)$ Å and $c = 11.6403(7)$ Å [15, 16]. In the cooling process, there is a structural transition to the orthorhombic phase (Fmmm space group) at approximately 170 K [17–20]. Highly doped samples do not show this transition, they remain in the tetragonal phase for each cobalt concentration. BZs for tetragonal and orthorhombic phases are shown in Figure 1b. For the content of the cobalt dopant above $x = 0.07$, a superconducting phase appears with the critical temperature $T_c \sim 20$ K [21].

The paper is organized as follows. Details of the techniques used are provided in Sec II. Next, in Sec. III we

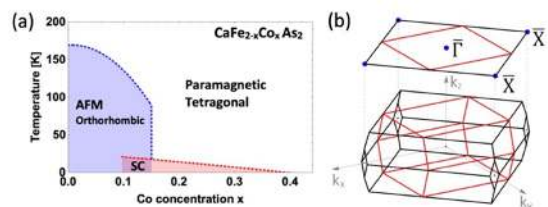


FIG. 1. The tetragonal crystal structure of LaCuSb_2 (a) and the corresponding first (a) Schematic phase diagram of the cobalt doped CaFe_2As_2 . (b) Brillouin zone of CaFe_2As_2 in tetragonal (black) and orthorhombic (red) phase.

* e-mail: marcin.rosmus@uj.edu.pl

† e-mail: pawel.starowicz@uj.edu.pl

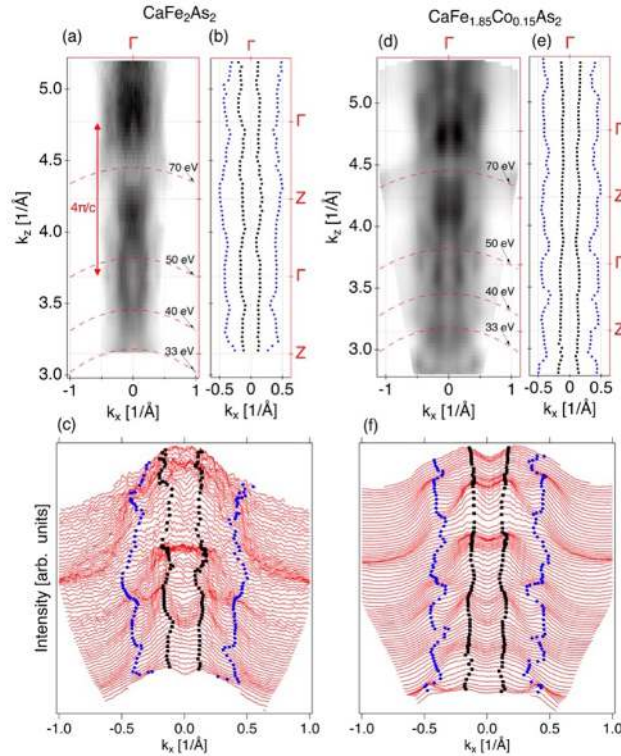


FIG. 2. FS map along kz and kx direction for CaFe_2As_2 and $\text{CaFe}_{1.85}\text{Co}_{0.15}\text{As}_2$. (a) Fermi Surface map for CaFe_2As_2 , (b) the positions of the two visible bands with the Fermi Surface determined based on MDC curves, (c) MDC curve. (d) Fermi Surface map for $\text{CaFe}_{1.85}\text{Co}_{0.15}\text{As}_2$, (e) the positions of the two visible bands with the Fermi Surface determined based on MDC curves, (f) MDC curves.

present and discuss our results. Finally, a summary is provided in Sect. IV.

II. METHODS AND TECHNIQUES

Single crystals of $\text{CaFe}_{2-x}\text{Co}_x\text{As}_2$ were grown using Sn flux method. The components were loaded into alumina crucibles and placed in quartz ampoules that were evacuated and filled with Ar gas under a pressure of 0.3 bar and sealed. The ampoules were heated to 600°C for 4 h, kept there for 1 h, then heated in 5 h to 1050°C , and kept at that temperature for 5 h so that all components are dissolved in the Sn flux. Next, the ampoules were cooled slowly at 2 K/h down to 600°C and subsequently cooled to room temperature. The flux was removed by a treatment with dilute hydrochloric acid. Phase purity was checked by powder XRD, and the chemical composition of the doped crystals was determined by energy dispersive XRD analysis. The transport properties of the $\text{CaFe}_{2-x}\text{Co}_x\text{As}_2$ single crystals have been character-

ized by measuring the resistivity and AC susceptibility as a function of temperature. For the heavily doped sample $\text{CaFe}_{1.85}\text{Co}_{0.15}\text{As}_2$, the transition to SC is observed at the temperature $T_{C,onset} = 18.7$ K, while for the lightly doped sample $\text{CaFe}_{1.93}\text{Co}_{0.07}\text{As}_2$ the onset temperature: $T_{C,onset} = 18$ K, and no flattening of resistance is observed. However, for a lightly doped sample, resistance measurements revealed a transition to the SDW state at $T_{SDW} = 135 - 140$ K. ARPES measurements were performed at URANOS beamline in the Solaris synchrotron [22] in Kraków, Poland. The endstation was equipped with the Scienta Omicron DA30L photoelectron spectrometer and the radiation source was a quasi-periodic APPLE II undulator. The samples were cleaved in situ under ultra-high vacuum at room temperature and the measurements were made at the temperature of 12 K. Base pressure was below 5×10^{-11} mbar. The desired orientation of single crystals was obtained using the Laue diffraction method.

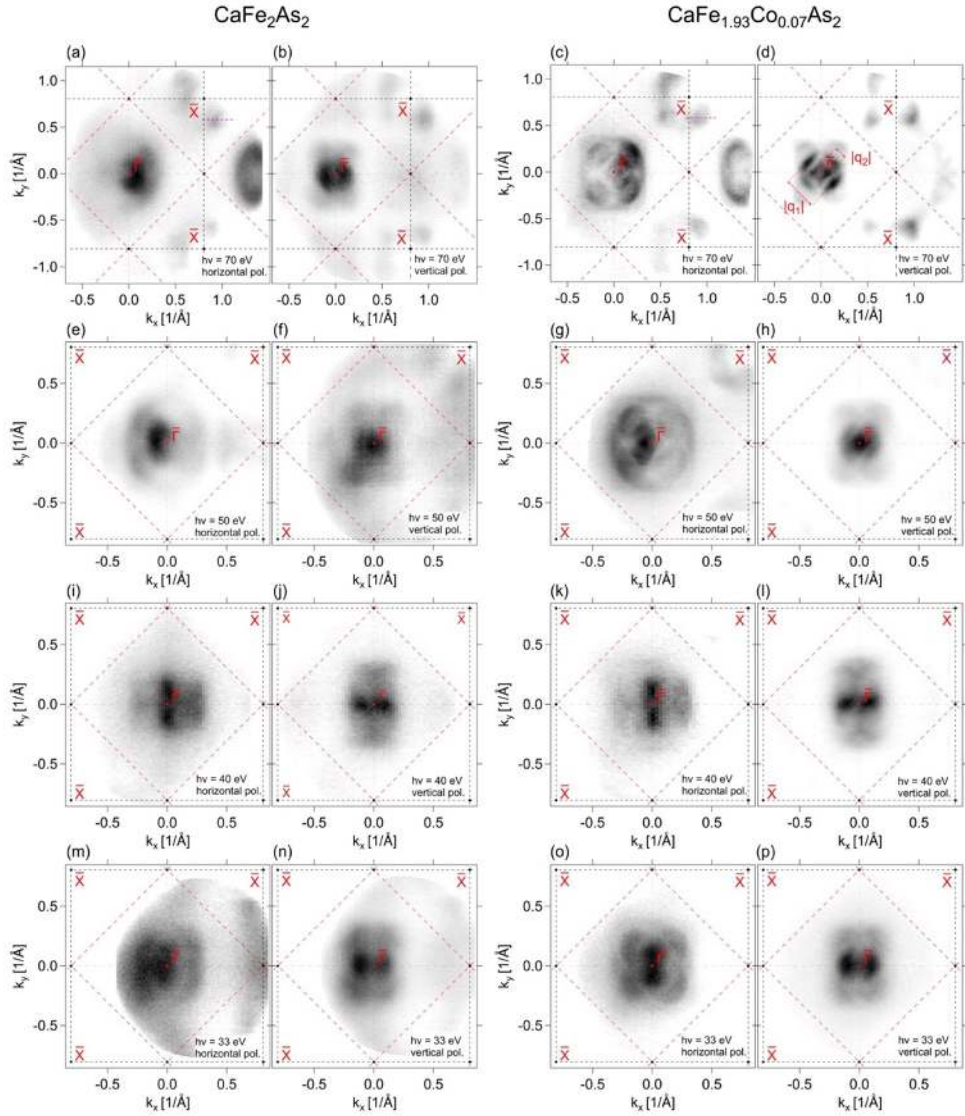


FIG. 3. Fermi surfaces collected at several photon energies and for different polarizations for CaFe_2As_2 (left) and $\text{CaFe}_{1.93}\text{Co}_{0.07}\text{As}_2$ (right). Details concerning energy and polarization are given in the figures. The paths, for which Dirac cones have been observed are marked with pink dashed lines in (a) and (c).

III. RESULTS AND DISCUSSION

Fermi Surface (FS) maps of undoped CaFe_2As_2 in the orthorhombic AFM phase and heavily doped $\text{CaFe}_{1.85}\text{Co}_{0.15}\text{As}_2$ in the tetragonal paramagnetic phase, obtained in the $k_z - k_x$ plane are shown in Figure 2. The observed structure is dominated by two bands, external and internal, which intersect the Fermi surface around

the direction determined by the Γ and Z points. To fully unravel the band structure in this direction, the four Gaussian distributions were fitted together with the polynomial background to each of the MDC curves. The positions of the maxima obtained in this way are shown in Figure 2 with black and blue squares. For both samples, the obtained structure is similar, with a practically two-dimensional inner pocket and a periodic outer pocket

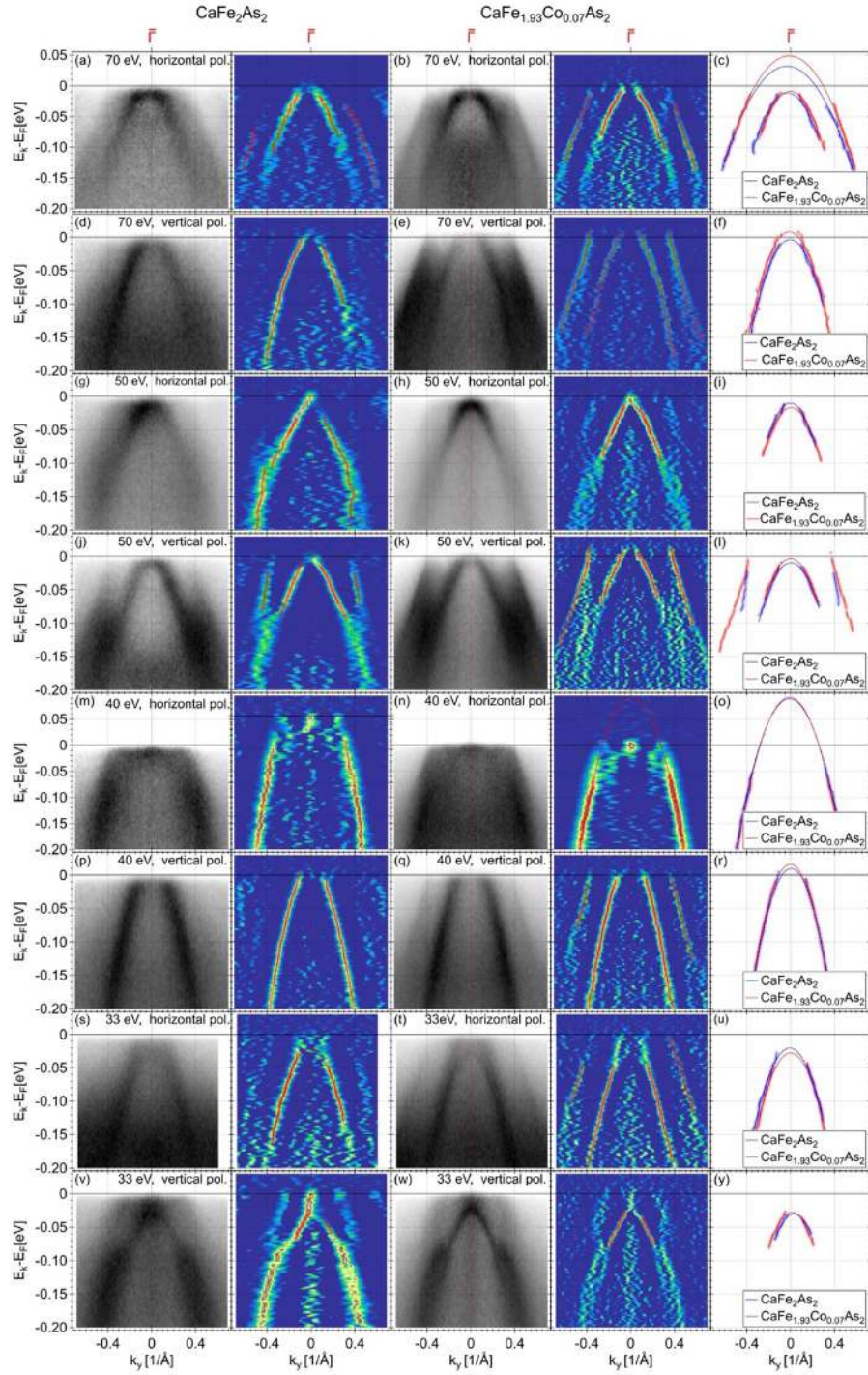


FIG. 4. ARPES measurements for the heavily doped sample $\text{CeFe}_{1.85}\text{Co}_{0.15}\text{As}_2$. (a-h) Fermi surface maps collected using different energies and for different polarizations. (i-j) Spectra collected along the high symmetry direction and the corresponding curvatures. Presented $\bar{\Gamma}-\bar{\Gamma}$ path corresponds to $k_x = 0$ in Figure 3.

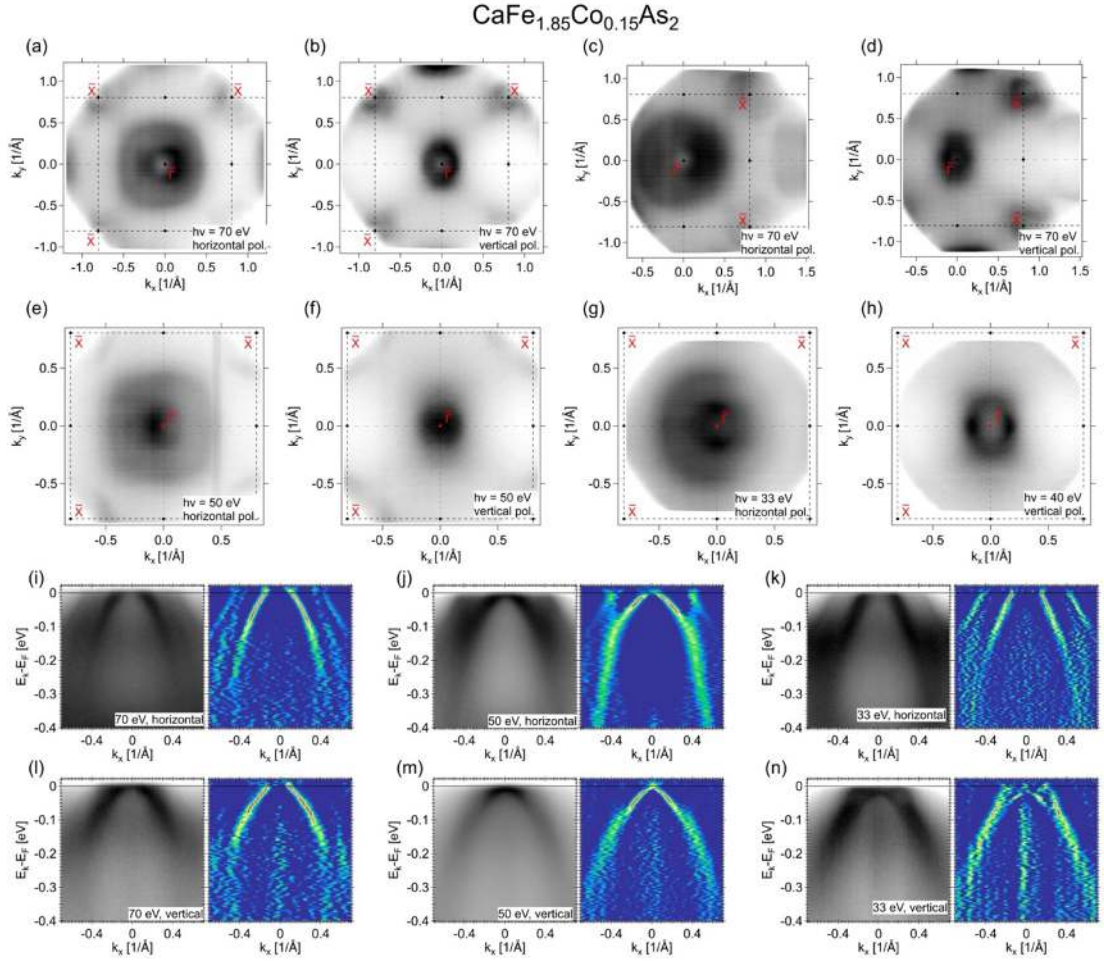


FIG. 5. ARPES measurements for the heavily doped sample $\text{CeFe}_{1.85}\text{Co}_{0.15}\text{As}_2$. (a-h) Fermi surface maps collected using different energies and for different polarizations. (i-j) Spectra collected along the high symmetry direction and the corresponding curvatures.

with the period equal to $4\pi/c$ corresponding to the distance between Γ points in neighbouring Brillouin zones. Based on the obtained data, it was possible to find the location of the high symmetry points. For Γ point $k_z = 3.15 \text{ \AA}^{-1}$ and $k_z = 4.23 \text{ \AA}^{-1}$, which corresponds to the photon energies $h\nu = 32$ eV and $h\nu = 68$ eV respectively. Similarly, the position of the Z points equals $k_z = 3.69 \text{ \AA}^{-1}$ and $k_z = 4.77 \text{ \AA}^{-1}$ and the photon energies: $h\nu = 44$ eV and $h\nu = 80$ eV respectively. All obtained FSs are in line with previous research on this topic for undoped samples [23, 24]. It is worth mentioning that there are no significant qualitative differences between the maps for both samples. Surprisingly, a significantly better quality of the spectra was obtained for

the doped samples.

The Fermi surface maps of the parent compound CaFe_2As_2 and sample highly doped sample $\text{CaFe}_{1.85}\text{Co}_{0.15}\text{As}_2$ in $k_x - k_y$ plane were collected for horizontal and vertical polarization and several photon energies (33 eV, 40 eV, 50 eV, 70 eV). Obtained results are shown in Figure 3. The bands crossing the Fermi energy (E_F) around the point $\bar{\Gamma}$ create a characteristic petal-like shape, while around point \bar{X} , a four-dot structure can be observed. The petal-like shape is associated with the occurrence of the SDW phase [20, 24, 25], and the large part of the FS that could be reconstructed with the nesting vectors. The length of these vectors has been estimated to $q_1 \sim 0.31 \cdot (\pi/a, \pi/a)$ and $q_2 \sim 0.11 \cdot (\pi/a, \pi/a)$ (Fig-

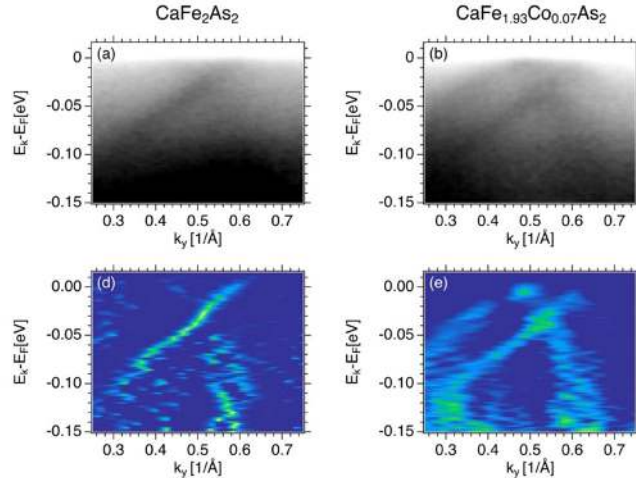


FIG. 6. Dirac cones observed near the point \bar{X} . ARPES spectra of (a) CaFe_2As_2 and (b) $\text{CaFe}_{1.93}\text{Co}_{0.07}\text{As}_2$; (c) and (d) corresponding curvature.

ure 3d) based on the map collected for the energy of 70 eV. The obtained value of the q_1 vector is in good agreement with Ref. [24] for BaFe_2As_2 and Ref. [20] for CaFe_2As_2 , being $0.33 \cdot (\pi/a, \pi/a)$. However, in Ref. [20] there is also the value determined for cobalt doped CaFe_2As_2 , equal to $0.24 \cdot (\pi/a, \pi/a)$, which is significantly different from the obtained value. The same article suggests that this value does not change in the whole momentum space. However, our results, as well as the map in the photon energy function in Ref. [24], suggest a strong dependence of the Fermi surface on the k_z value, which explains the observed differences.

Two BZs are marked in Figure 3, the first one represents the tetragonal AFM phase (black dashed lines), and the second one is connected to the orthorhombic SDW phase (red dashed lines). The BZ folding is not clearly visible on the presented maps, since the measurements were made on twinned samples. The effect of breaking the rotational symmetry, reported earlier [26], would be obtained if the experiment was performed on a detwinned sample or domains that were significantly smaller than the size of the beam. As with the maps collected for several photon energies, there are no discernible differences between the undoped and lightly doped sample. Let us discuss in more detail the expected differences between the band structures of the tested compounds caused by doping. The rigid band-shifting scenario assumes a constant shift of the bands under the influence of doping, which does not result in the deformation of the structure. In other words, doping in this simplification only results in a shift of the Fermi energy [27–30]. In Figure 4 we present a detailed analysis of the band dispersion across the $\bar{\Gamma}$ – $\bar{\Gamma}$ direction. The first column shows the measured band dispersion collected for the

undoped sample, the second shows their curvature [31], and then analogously for the doped sample. Based on the calculated curvatures, the Gauss function was fit to consecutive MDC curves, thus obtaining a mapping of the bands. The results are shown in Figure 4 (last column). It is clearly visible that for neither energy nor any polarization, a noticeable shift was obtained within the measurement resolution limits. However, based on our previous work [32], the number of electrons added to the system with 3.5% cobalt doping per iron atom corresponds to a band shift of about 10 meV. Assuming that, in the case of the $\text{CaFe}_{2-x}\text{Co}_x\text{As}_2$ compounds, one can expect shifts of a similar order, these values are below or at the limit of the resolution of the measuring system for the energies used, so the results are not inconsistent with the aforementioned model. The measurements collected for the sample, which was highly doped with cobalt ($\text{CaFe}_{1.85}\text{Co}_{0.15}\text{As}_2$), in the tetragonal paramagnetic phase are shown in Figure 5. The mapping of the Fermi surface was carried out for the three different photon energies (33 eV, 50 eV, 70 eV) using horizontal and vertical polarization analogous to the maps for the samples described in the previous section of the paper. The obtained maps are presented in Figure 5(a-h). The band structure along the $\bar{\Gamma}$ – $\bar{\Gamma}$ direction is presented in Figure 5i-n. The Fermi surfaces consist of concentric cylindrical hole pockets around the $\bar{\Gamma}$ point and electron pockets around the \bar{X} point. This structure is significantly different from that observed for the parent compound and the sample with low cobalt content ($\text{CaFe}_{1.93}\text{Co}_{0.07}\text{As}_2$). It is related to the tetragonal phase and the appearance of superconductivity in the system related to the tetragonal phase in $\text{CaFe}_{2-x}\text{Co}_x\text{As}_2$ system (Figure 1). Maps of the Fermi surface for different locations in the k_z di-

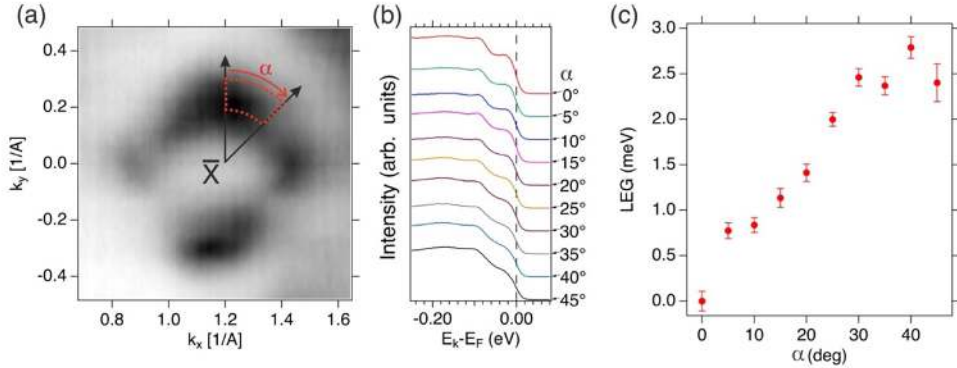


FIG. 7. (a) The region of the Fermi surface of an undoped CaFe_2As_2 around the \bar{X} point, collected with $h\nu = 70$ eV. The red area indicates the region from which the EDC curves have been extracted and α defines the position of each curve. (b) EDC curves are shown along intersections defined by angle α in (a). (c) LEG as a function of α .

rection revealed the changes of the external band around the Γ point. Based on the collected data, the energy of the maximum of this band is displaced from above the Fermi energy (e.g. Figure 5k) to the situation in which it touches E_F (e.g. Figure 5m). This proves the three-dimensional nature of this band. However, the rest of the observed structure, qualitatively, does not change significantly with the change of position in the k_z direction, which proves the quasi-two-dimensional nature of these bands. This is a typical structure of iron superconductors in the antiferromagnetic phase [33, 34].

In the case of the parent compound and the lightly doped sample, careful analysis of the signal creating two bright spots around the \bar{X} point (exact position is marked by the pink dashed line in Figure 3) revealed the existence of a Dirac-like dispersion. The intensity plots of the ARPES spectra collected along that direction and the corresponding 3D curvatures are shown in Figure 6. The apex of the cone is located about 30 meV beneath the E_F , making it much deeper than previously reported for the BaFe_2As_2 , where the apex of the cone lays above E_F [5]. The observation of these structures suggested that CaFe_2As_2 could be classified as the nodal SDW system [13, 35]. The second characteristic feature of the nodal SDW, proposed by Ran et al., is the existence of gapless nodes, which are forced by symmetry degeneracy at the $\bar{\Gamma}$ and \bar{X} points. The nodes should appear in the same region as the cones, and the gap width should vary between the cones. To investigate this scenario, we performed the leading gap edge (LEG) analysis on EDCs around the \bar{X} point. The EDC curves were extracted from the collected spectrum along intersections made every 5 degrees with the center of \bar{X} point. An α angle (Figure 7) was defined to indicate the position of each curve. Integration was carried out within the limits marked by the red area in Figure 7a and the angular width of 1 degree. For each curve collected in this way (shown in Figure 7b), a Fermi-Dirac distribution was fit-

ted with the background. Based on this, the location of LEG was determined as shown in Figure 7c. For the entire range examined, no real LEG shift was observed. The fit showed changes in the order of single millielectron volts, which is below the resolution of the system and cannot be considered as a significant result. The expected gap obtained in the course of the analogous analysis on the BaFe_2As_2 compound by Richard et al. was about 20 meV. Our data show the absence of the postulated gap in the studied region and indicate significant differences in the character of the SDW between the BaFe_2As_2 and CaFe_2As_2 compounds. It is worth noting that the cones were observed for both samples from AFM region of the phase diagram, including the superconducting one. This may be the result of the coexistence of the superconducting phase and the Dirac-like dispersion. Another explanation is the heterogeneity of the samples; part of the volume was in the SDW phase and was the source of the signal with cones; another part of the sample was in a superconducting phase which was visible in transport measurements. Regardless of this, even in a two-phase sample, there is a possibility of the existence of Dirac cones in the superconducting region due to the proximity effect. No Dirac cone was observed for the strongly doped sample. This is consistent with the assumption that the occurrence of topological states in this system is related to the nature of SDW [5, 13], as the SDW is not accounted for high doped sample.

IV. SUMMARY

To conclude we have investigated the electronic structure of the cobalt-doped CaFe_2As_2 compound for the samples corresponding to all the states that form the phase diagram. We have observed two types of electron structures depending on the doping level. For the antiferromagnetic phase, a characteristic petal-like structure

related to SDW is found, while the structure in the paramagnetic phase consists of concentric hole bands around the Γ point and electron bands around the point \bar{X} . We did not observe a significant change in the band structure under the influence of cobalt doping within the orthorhombic phase. For a low doping level, the existence of Dirac cones was revealed, which is analogous to those

measured in the BaFe_2As_2 compound. These structures may be related to a nodal SDW system. What is particularly interesting, is the lack of observation of the energy gap in the region where the cones are found and where the characteristic features of the nodal SDW phase should be manifested.

-
- [1] N. Ni and S. L. Bud'ko, Tuning the ground state of BaFe_2As_2 : Phase diagrams and empirical trends, *MRS Bulletin* **36**, 620 (2011).
- [2] Y.-Y. Tai, J.-X. Zhu, M. J. Graf, and C. S. Ting, Calculated phase diagram of doped BaFe_2As_2 superconductor in a C_4 -symmetry breaking model, *EPL (Europhysics Letters)* **103**, 67001 (2013).
- [3] J.-H. Chu, J. G. Analytis, C. Kucharczyk, and I. R. Fisher, Determination of the phase diagram of the electron-doped superconductor $\text{Ba}(\text{Fe}_{1-x}\text{Co}_x)_2\text{As}_2$, *Physical Review B* **79**, 014506 (2009).
- [4] M. Widom and K. Quader, First-principles study of CaFe_2As_2 under pressure, *Physical Review B* **88**, 045117 (2013).
- [5] P. Richard, K. Nakayama, T. Sato, M. Neupane, Y.-M. Xu, J. H. Bowen, G. F. Chen, J. L. Luo, N. L. Wang, X. Dai, Z. Fang, H. Ding, and T. Takahashi, Observation of Dirac Cone Electronic Dispersion in BaFe_2As_2 , *Physical Review Letters* **104**, 137001 (2010).
- [6] M. Matusiak, Z. Bukowski, and J. Karpinski, Nernst effect in single crystals of the pnictide superconductor $\text{CaFe}_{1.92}\text{Co}_{0.08}\text{As}_2$ and parent compound CaFe_2As_2 , *Physical Review B* **81**, 020510 (2010).
- [7] B. Xu, H. Xiao, B. Gao, Y. H. Ma, G. Mu, P. Marsik, E. Sheveleva, F. Lyzwa, Y. M. Dai, R. P. S. M. Lobo, and C. Bernhard, Optical study of Dirac fermions and related phonon anomalies in the antiferromagnetic compound CaFeAsF , *Physical Review B* **97**, 195110 (2018).
- [8] T. Terashima, H. T. Hirose, D. Graf, Y. Ma, G. Mu, T. Hu, K. Suzuki, S. Uji, and H. Ikeda, Fermi Surface with Dirac Fermions in CaFeAsF Determined via Quantum Oscillation Measurements, *Physical Review X* **8**, 011014 (2018).
- [9] Z.-G. Chen, L. Wang, Y. Song, X. Lu, H. Luo, C. Zhang, P. Dai, Z. Yin, K. Haule, and G. Kotliar, Two-Dimensional Massless Dirac Fermions in Antiferromagnetic AFe_2As_2 ($\text{A} = \text{Ba}, \text{Sr}$), *Physical Review Letters* **119**, 096401 (2017).
- [10] M. Matusiak and T. Wolf, In-plane transport anisotropy in a $\text{Ba}_{1-x}\text{K}_x\text{Fe}_2\text{As}_2$ iron-based superconductor, *Superconductor Science and Technology* **32**, 105013 (2019).
- [11] K. K. Huynh, Y. Tanabe, and K. Tanigaki, Both Electron and Hole Dirac Cone States in BaFe_2As_2 Confirmed by Magnetoresistance, *Physical Review Letters* **106**, 217004 (2011).
- [12] M. Sutherland, D. J. Hills, B. S. Tan, M. M. Altarawneh, N. Harrison, J. Gillett, E. C. T. O'Farrell, T. M. Benseman, I. Kokanovic, P. Syers, J. R. Cooper, and S. E. Sebastian, Evidence for Dirac nodes from quantum oscillations in SrFe_2As_2 , *Physical Review B* **84**, 180506 (2011).
- [13] Y. Ran, F. Wang, H. Zhai, A. Vishwanath, and D.-H. Lee, Nodal spin density wave and band topology of the FeAs-based materials, *Physical Review B* **79**, 014505 (2009).
- [14] L. Pan, J. Li, Y.-Y. Tai, M. J. Graf, J.-X. Zhu, and C. S. Ting, Evolution of the Fermi surface topology in doped 122 iron pnictides, *Physical Review B* **88**, 214510 (2013).
- [15] B. Saparov, C. Cantoni, M. Pan, T. C. Hogan, W. R. Li, S. D. Wilson, K. Fritsch, M. Tachibana, B. D. Gaulin, and A. S. Sefat, Complex structures of different CaFe_2As_2 samples, *Scientific Reports* **4**, 4120 (2014).
- [16] N. Ni, S. Nandi, A. Kreyssig, A. I. Goldman, E. D. Mun, S. L. Bud'ko, and P. C. Canfield, First-order structural phase transition in CaFe_2As_2 , *Physical Review B* **78**, 014523 (2008).
- [17] K. Ali and K. Maiti, Emergent electronic structure of CaFe_2As_2 , *Scientific Reports* **7**, 6298 (2017).
- [18] D. Tompsett and G. Lonzarich, Dimensionality and magnetic interactions in CaFe_2As_2 : An ab initio study, *Physica B: Condensed Matter* **405**, 2440 (2010).
- [19] M. D. Watson, P. Dudin, L. C. Rhodes, D. V. Evtushinsky, H. Iwasawa, S. Aswartham, S. Wurmehl, B. Büchner, M. Hoesch, and T. K. Kim, Probing the reconstructed Fermi surface of antiferromagnetic BaFe_2As_2 in one domain, *npj Quantum Materials* **4**, 36 (2019).
- [20] Q. Wang, Z. Sun, E. Rotenberg, F. Ronning, E. D. Bauer, H. Lin, R. S. Markiewicz, M. Lindroos, B. Barbiellini, A. Bansil, and D. S. Dessau, Symmetry-broken electronic structure and uniaxial Fermi surface nesting of untwinned CaFe_2As_2 , *Physical Review B* **88**, 235125 (2013).
- [21] L. Harnagea, S. Singh, G. Friemel, N. Leps, D. Bombor, M. Abdel-Hafiez, A. U. B. Wolter, C. Hess, R. Klingeler, G. Behr, S. Wurmehl, and B. Büchner, Phase diagram of the iron arsenide superconductors $\text{Ca}(\text{Fe}_{1-x}\text{Co}_x)_2\text{As}_2$ ($0 \leq x \leq 0.2$), *Physical Review B* **83**, 094523 (2011).
- [22] J. Szlachetko, J. Szade, E. Beyer, W. Błachucki, P. Ciochoń, P. Dumas, K. Freindl, G. Gazdowicz, S. Glatt, K. Guła, J. Hormes, P. Indyka, A. Klonecka, J. Kołodziej, T. Kołodziej, J. Korecki, P. Korecki, F. Kosiorowski, K. Kosowska, G. Kowalski, M. Kozak, P. Koziol, W. Kwiatek, D. Liberda, H. Lichtenberg, E. Madej, A. Mandziak, A. Marendziak, K. Matlak, A. Maximenko, P. Nita, N. Olszowska, R. Panaś, E. Partyka-Jankowska, M. Piszak, A. Prange, M. Rawski, M. Roman, M. Rosmus, M. Sikora, J. Sławek, T. Sobol, K. Sowa, N. Spiridis, J. Stępień, M. Szczepanik, T. Ślęzak, T. Tyliszczak, G. Ważny, J. Wiechecki, D. Wilgocka-Ślęzak, B. Wolanin, P. Wróbel, T. Wróbel, M. Zając, A. Wawrzyniak, and M. Stankiewicz, SOLARIS National Synchrotron Radiation Centre in Krakow, Poland, *Eur. Phys. J. Plus* **138**, 10 (2023).
- [23] C. Liu, T. Kondo, N. Ni, A. D. Palczewski, A. Bostwick, G. D. Samolyuk, R. Khasanov, M. Shi, E. Rotenberg, S. L. Bud'ko, P. C. Canfield, and A. Kaminski,

- Three- to Two-Dimensional Transition of the Electronic Structure in CaFe_2As_2 : A Parent Compound for an Iron Arsenic High-Temperature Superconductor, *Physical Review Letters* **102**, 167004 (2009).
- [24] T. Kondo, R. M. Fernandes, R. Khasanov, C. Liu, A. D. Palczewski, N. Ni, M. Shi, A. Bostwick, E. Rotenberg, J. Schmalian, S. L. Bud'ko, P. C. Canfield, and A. Kaminski, Unexpected Fermi-surface nesting in the pnictide parent compounds BaFe_2As_2 and CaFe_2As_2 revealed by angle-resolved photoemission spectroscopy, *Physical Review B* **81**, 060507 (2010).
- [25] F. Chen, Y. Zhang, J. Wei, B. Zhou, L. Yang, F. Wu, G. Wu, X. Chen, and D. Feng, Electronic structure reconstruction of CaFe_2As_2 in the spin density wave state, *Journal of Physics and Chemistry of Solids* **72**, 469 (2011).
- [26] M. Yi, D. Lu, J.-H. Chu, J. G. Analytis, A. P. Sorini, A. F. Kemper, B. Moritz, S.-K. Mo, R. G. Moore, M. Hashimoto, W.-S. Lee, Z. Hussain, T. P. Devereaux, I. R. Fisher, and Z.-X. Shen, Symmetry-breaking orbital anisotropy observed for detwinned $\text{Ba}(\text{Fe}_{1-x}\text{Co}_x)_2\text{As}_2$ above the spin density wave transition, *Proceedings of the National Academy of Sciences* **108**, 6878 (2011).
- [27] S. Thirupathiah, J. Fink, P. K. Maheshwari, V. V. R. Kishore, Z.-H. Liu, E. D. L. Rienks, B. Büchner, V. P. S. Awana, and D. D. Sarma, Effect of impurity substitution on band structure and mass renormalization of the correlated $\text{FeTe}_{0.5}\text{Se}_{0.5}$ superconductor, *Physical Review B* **93**, 205143 (2016).
- [28] P. Vilmercati, S.-K. Mo, A. Fedorov, M. A. McGuire, A. Sefat, B. Sales, D. Mandrus, D. J. Singh, W. Ku, S. Johnston, and N. Mannella, Nonrigid band shift and nonmonotonic electronic structure changes upon doping in the normal state of the pnictide high-temperature superconductor $\text{Ba}(\text{Fe}_{1-x}\text{Co}_x)_2\text{As}_2$, *Physical Review B* **94**, 195147 (2016).
- [29] C. Liu, T. Kondo, R. M. Fernandes, A. D. Palczewski, E. D. Mun, N. Ni, A. N. Thaler, A. Bostwick, E. Rotenberg, J. Schmalian, S. L. Bud'ko, P. C. Canfield, and A. Kaminski, Evidence for a Lifshitz transition in electron-doped iron arsenic superconductors at the onset of superconductivity, *Nature Physics* **6**, 419 (2010).
- [30] C. Liu, A. D. Palczewski, R. S. Dhaka, T. Kondo, R. M. Fernandes, E. D. Mun, H. Hodovanets, A. N. Thaler, J. Schmalian, S. L. Bud'ko, P. C. Canfield, and A. Kaminski, Importance of the Fermi-surface topology to the superconducting state of the electron-doped pnictide $\text{Ba}(\text{Fe}_{1-x}\text{Co}_x)_2\text{As}_2$, *Physical Review B* **84**, 020509 (2011).
- [31] P. Zhang, P. Richard, T. Qian, Y.-M. Xu, X. Dai, and H. Ding, A precise method for visualizing dispersive features in image plots, *Review of Scientific Instruments* **82**, 043712 (2011).
- [32] M. Rosmus, R. Kurlito, D. J. Gawryluk, J. Goraus, M. Z. Cieplak, and P. Starowicz, Effect of electron doping in $\text{FeTe}_{1-y}\text{Se}_y$ realized by Co and Ni substitution, *Superconductor Science and Technology* **32**, 105009 (2019).
- [33] A. A. Kordyuk, Iron-based superconductors: Magnetism, superconductivity, and electronic structure, *Low Temperature Physics* **38**, 888 (2012).
- [34] X. Liu, L. Zhao, S. He, J. He, D. Liu, D. Mou, B. Shen, Y. Hu, J. Huang, and X. J. Zhou, Electronic structure and superconductivity of FeSe-related superconductors, *Journal of Physics: Condensed Matter* **27**, 183201 (2015).
- [35] S. Sugai, Y. Mizuno, R. Watanabe, T. Kawaguchi, K. Takenaka, H. Ikuta, K. Kiho, M. Nakajima, C. H. Lee, A. Iyo, H. Eisaki, and S. Uchida, The Nodal SDW Gap and the Superconducting Gap in $\text{BaFe}_{2x}\text{Co}_x\text{As}_2$, *Journal of Superconductivity and Novel Magnetism* **24**, 1185 (2011).


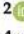




6. Electronic Band Structure and Surface States in Dirac Semimetal LaAgSb₂

M. Rosmus, N. Olszowska, Z. Bukowski, P. Starowicz, P. Piekarz, A. Ptok

I performed measurements of angle-resolved photoelectron spectroscopy (ARPES) together with N.O. I prepared the samples for measurements by orientation using the Laue diffraction method. I analyzed the experimental data, developed the code for the analysis, and attached the experimental drawings. Together with A.P. I compared the data with the theoretical results. I participated in work on the first draft of the manuscript. The manuscript was corrected and discussed by M.R., N.O., P.S., P.P. and A.P. My contribution to the publication was 40%.

Article

Electronic Band Structure and Surface States in Dirac Semimetal LaAgSb₂

Marcin Rosmus ^{1,2,*}, Natalia Olszowska ², Zbigniew Bukowski ³, Paweł Starowicz ¹, Przemysław Piekarczyk ⁴ and Andrzej Ptok ^{4,*}

¹ Marian Smoluchowski Institute of Physics, Jagiellonian University, Prof. S. Łojasiewicza 11, 30-348 Kraków, Poland

² Solaris National Synchrotron Radiation Centre, Jagiellonian University, Czerwone Maki 98, 30-392 Kraków, Poland

³ Institute of Low Temperature and Structure Research, Polish Academy of Sciences, Okólna 2, 50-422 Wrocław, Poland

⁴ Institute of Nuclear Physics, Polish Academy of Sciences, W. E. Radzikowskiego 152, 31-342 Kraków, Poland

* Correspondence: marcin.rosmus@uj.edu.pl (M.R.); aptok@mmj.pl (A.P.)

Abstract: LaAgSb₂ is a Dirac semimetal showing charge density wave (CDW) order. Previous angle-resolved photoemission spectroscopy (ARPES) results suggest the existence of the Dirac-cone-like structure in the vicinity of the Fermi level along the Γ -M direction. This paper is devoted to a complex analysis of the electronic band structure of LaAgSb₂ by means of ARPES and theoretical studies within the ab initio method as well as tight binding model formulation. To investigate the possible surface states, we performed the direct DFT slab calculation and the surface Green function calculation for the (001) surface. The appearance of the surface states, which depends strongly on the surface, points to the conclusion that LaSb termination is realized in the cleaved crystals. Moreover, the surface states predicted by our calculations at the Γ and X points are found by ARPES. Nodal lines, which exist along the X-R and M-A paths due to crystal symmetry, are also observed experimentally. The calculations reveal other nodal lines, which originate from the vanishing of spin-orbit splitting and are located at the X-M-A-R plane at the Brillouin zone boundary. In addition, we analyze the band structure along the Γ -M path to verify whether Dirac surface states can be expected. Their appearance in this region is not confirmed.

Keywords: Dirac semimetal; band structure; ARPES; DFT



Citation: Rosmus, M.; Olszowska, N.; Bukowski, Z.; Starowicz, P.; Piekarczyk, P.; Ptok, A. Electronic Band Structure and Surface States in Dirac Semimetal LaAgSb₂. *Materials* **2022**, *15*, 7168. <https://doi.org/10.3390/ma15207168>

Academic Editor: Antonio Politano

Received: 14 September 2022

Accepted: 11 October 2022

Published: 14 October 2022

Publisher's Note: MDPI stays neutral with regard to jurisdictional claims in published maps and institutional affiliations.



Copyright: © 2022 by the authors. Licensee MDPI, Basel, Switzerland. This article is an open access article distributed under the terms and conditions of the Creative Commons Attribution (CC BY) license (<https://creativecommons.org/licenses/by/4.0/>).

1. Introduction

The discovery of topological insulators with a large gap opened a period of intensive studies of this type of topological system [1–3]. Due to the intrinsic band inversion, it is possible to realize the topologically protected conducting surface states with linear dispersion, which is called Dirac cones [4–8]. Such surface states paved the way for studying a novel phase of matter [9–11].

In practice, Dirac cones are observed not only in topological insulators but also in other topological systems. One of the examples, where the existence of these surface states is expected, is the Dirac semimetal LaAgSb₂ (Figure 1). It is characterized by the rare and untypical coexistence of the topological phase and the charge density wave (CDW) order [12]. The CDW modulations in LaAgSb₂ were found by the X-ray scattering measurements [12] as well as using the pump-probe spectroscopy [13]. In addition, thermal conductivity and ¹³⁹La nuclear magnetic resonance (NMR) indicate the phase transition [14]. A periodic charge and lattice modulation with the wave vector $q_1 \sim 0.026 \times (2\pi/a)$ develops along the *a* direction below the temperature $T_{CDW}^1 = 207$ K. Further decreasing of the temperature results in an additional CDW ordering below $T_{CDW}^2 = 186$ K along the *c* direction with $q_2 \sim 0.16 \times (2\pi/c)$. The realization of CDW with tiny modulation

wave vectors can be associated with the Fermi surface (FS) nesting [15]. Application of the external hydrostatic pressure leads to the suppression of T_{CDW} and finally to the disappearance of the CDW phases (around 2–3 GPa) [16–18]. Similarly, the CDW phase can be destroyed by the chemical doping [17,18].

The existence of the topological phase is indicated by the interesting transport and magnetic properties of LaAgSb_2 . For example, a large linear magnetoresistance and a positive Hall resistivity were observed [19–21]. Similar behavior was also found in the compound with the same structure, namely the topological magnetic system SrMnBi_2 [22–24]. In that case, the transport behavior is related to the occurrence of the anisotropic Dirac states, where linear energy dispersion originates from the crossing of the p -orbital bands in the double-size Bi square net [22]. The first principles study indicated similar properties in the case of LaAgSb_2 , where the p orbitals of Sb atoms create the bands with a nearly linear dispersion [21]. More recently, the angle-resolved photoemission spectroscopy (ARPES) of LaAgSb_2 was performed [25].

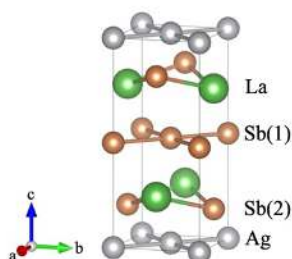


Figure 1. The tetragonal crystal structure of LaAgSb_2 .

Motivation—The aforementioned ARPES [25] study indicates the existence of several anomalies in the spectral function. In particular, the Dirac-cone-like structure, which originates from the band crossing, was found along the Γ –M direction. In this paper, we performed a systematic and complex study of the electronic band structure of LaAgSb_2 , using both high-quality ARPES measurements and theoretical analyses. The theoretical study of the electronic band structure was based on the density functional theory (DFT) calculations as well as on the tight binding model. Possible surface states were predicted within the direct DFT calculation for slab geometry and the surface Green function technique for the (001) surface. We show that the realized surface states strongly depend on the termination of the system. Theoretically predicted surface states at Γ and X were confirmed by the ARPES measurements. A presence of nodal lines, which originate either from lattice symmetry or vanishing of spin-orbit splitting, is discussed. Additionally, we analyze the possible Dirac surface states along the Γ –M direction [25]. Our theoretical and experimental study does not confirm the realization of such states along this direction.

This paper is organized as follows. Experimental and theoretical methods are briefly described in Section 2. Next, we presented and discuss our results in Section 3. Finally, Section 4 contains conclusions and a summary.

2. Techniques

2.1. Sample Preparation

Single crystals of LaAgSb_2 were grown by the self-flux technique similar to the method reported in Ref. [20] and also applied for the growth of UCoS_2 crystals [26]. Lanthanum (purity 99.9%), silver (purity 99.99%), and antimony (purity 99.999%) were used as starting materials. The components were weighed in the atomic ratio $\text{La}:\text{Ag}:\text{Sb} = 1:1.1:22$ and placed in an alumina crucible, which was then sealed in an evacuated silica tube. The ampoule was heated at 1100 °C for 5 h followed by slow cooling (2 °C/h) down to 680 °C. At this temperature, the ampoule was flipped upside down in order to decant still liquid Sb-Ag flux. Next, the ampule was fast cooled to room temperature, and the crucible was

transferred to another silica tube, where the rest of Sb was removed from crystals by means of sublimation in high vacuum at 600 °C. Finally, single crystals were mechanically isolated.

The obtained crystals were examined using a scanning electron microscope (SEM), and their chemical composition was determined with energy-dispersive X-ray spectroscopy (EDX) using a standardless procedure. The crystal structure and lattice parameters were determined using powder X-ray diffraction on a sample of the crushed single crystal.

2.2. Experimental Details

High-resolution angle-resolved photoemission studies were performed using two ARPES systems, one at Solaris Synchrotron, Kraków, Poland, at URANOS beamline, equipped with a Scienta-Omicron DA30-L electron analyzer (Scienta Omicron, Uppsala, Sweden), and the other at our in-house laboratory with a Scienta R4000 analyzer using He-I radiation ($h\nu = 21.218$ eV). Samples measured with use of the synchrotron radiation were cleaved in situ in ultrahigh vacuum at room temperature, and the measurements were performed at the temperature of 12 K, while in the in-house laboratory, the samples were cleaved and measured at a temperature of 20 K. The base pressure was below 5×10^{-11} mbar in both systems. In the case of measurements performed at the synchrotron, the spectra were collected in the vertical and horizontal polarization of the incident light. The ARPES results are presented as the sum of these two scans in order to reduce the matrix element contribution. In order to comprehensively analyze the obtained data, the 2D curvature method [27] was used.

2.3. Calculation Details

The DFT calculations were performed within the projector augmented-wave (PAW) method [28] using the Vienna Ab initio Simulation Package (VASP) [29–31]. The exchange–correlation potential was obtained by the generalized gradient approximation (GGA) in the form proposed by Perdew, Burke, and Enzerhof (PBE) [32]. We also investigated the impact of the spin–orbit coupling (SOC) [33] on the electronic structure.

The optimization of both the structural parameters and the electronic structure was performed using a $20 \times 20 \times 10$ Monkhorst–Pack k -grid [34]. The energy cut-off for the plane-wave expansion was equal to 520 eV. The structures were relaxed using the conjugate gradient technique with the energy convergence criteria set at 10^{-8} eV and 10^{-6} eV for the electronic and ionic iterations, respectively. Next, the optimized structure was used to construct the tight binding model in the maximally localized Wannier orbitals (cf. Appendix A). The surface Green function for a semi-infinite system [35] for study of the surface states was calculated using WANNIERTOOLS (version 2.5.1) [36].

3. Results and Discussion

3.1. Crystal Structure

LaAgSb₂ crystallizes in the tetragonal ZrCuSi₂-type lattice [37] with the layered structure $P4/nmm$ (space group 129) presented in Figure 1. The obtained experimental crystals are rectangular and plate-like with a crystallographic c axis perpendicular to the plane. The chemical composition of the crystals, determined from the EDX data, corresponded well to the ideal formula LaAgSb₂. The lattice parameters determined from XRD ($a = b = 4.390$ Å and $c = 10.84$ Å) are in good agreement with those reported in the literature ($a = b = 4.359$ Å, and $c = 10.787$ Å [38,39]). In our calculations, the lattice constants were found as $a = b = 4.43974$ Å, and $c = 10.89658$ Å, which are in good agreement with the experimental results. The Wyckoff positions of atoms are La: $2c$ ($1/4, 1/4, 0.73994$), Ag: $2a$ ($3/4, 1/4, 0$), Sb(1): $2b$ ($3/4, 1/4, 1/2$), and Sb(2): $2c$ ($1/4, 1/4, 0.17137$). The Sb(1) atoms form a two-dimensional square lattice, while the Sb(2) atoms coordinated by La atoms form a LaSb(2) double layer characterized by the glide symmetry. The Ag atoms reside between two LaSb(2) layers. The layered structure can be viewed as a sequential stacking of Sb(1)–LaSb(2)–Ag–LaSb(2)–Sb(1) layers along the c axis (cf. Figure 1).

3.2. Band Structure and Fermi Surface

The ab initio (DFT) calculated bulk band structure is presented in Figure 2, where we show the comparison of the results in the absence and presence of the spin–orbit coupling (orange and blue lines, respectively). They are in agreement with the previous study [21,40,41]. The unoccupied La 5*f* orbitals are located above the Fermi level (around 2 eV). The 5*p* orbitals are responsible for the emergence of the nearly linear band crossing the Fermi level [21,41]. These bands are associated with the several places where band crossing exists. These points arise due to the folding of the dispersion relation of the *p*-orbitals in Ag and Sb nets. Including the spin–orbit coupling removes the degeneracy of these points.

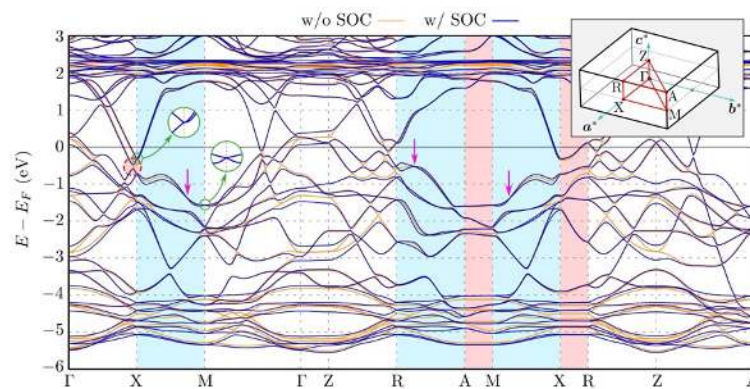


Figure 2. The bulk band structure in the absence and presence of the spin–orbit coupling (orange and blue lines, respectively). X–M and R–A paths, where nodal lines can be realized due to vanishing spin–orbit splitting, are marked with blue background. Similarly, X–R and A–M paths are highlighted with red background, where nodal lines with fourfold degeneracy exist due to the $P4/nmm$ symmetry. Two circular insets highlight the bulk Dirac cones at the X and M points. The top right inset presents the Brillouin zone of the tetragonal structure $P4/nmm$ and its high-symmetry points [42].

Around the X point, we can observe the influence of the SOC on the electronic band structure. Along the Γ –X direction without the SOC, there are four different irreducible representations of bands, and the crossing of bands exists [43]. The presence of the SOC allows for only one irreducible representation and causes band splitting as well as gap opening close to the X point (marked by the dashed red circle in Figure 2). Additionally, the energy difference between two Dirac-like cones at the X point (first zoom inside left inset in Figure 2 and second non-shown below them) typically strongly depends on c/a [43]. The described modification originates mostly from folding of the band structures of Ag and Sb square nets [44,45], which is due to the realization of their double unit cell, i.e., $\sqrt{2} \times \sqrt{2} \times 1$ cell, within the LaAgSb₂ cell (cf. Figure S1 in the Supplementary Material (SM), which contains more additional theoretical results).

Highly degenerated nodal lines—Including SOC leads to lifting of the band degeneracy, while the time reversal symmetry is still preserved due to the absence of the magnetic order.

Additionally, the space group $P4/nmm$ guarantees the existence of the nonsymmorphic glide symmetry [45,46]. Assembling these symmetries with the three-dimensional (3D) inversion symmetry has a consequence in the form of the bulk band structure [47]. Along the high symmetry directions, all the bands at the X and M points are doubly degenerated by the glide mirror symmetry, forming Dirac points (two left insets in Figure 2 and Figure S2 in the Supplementary Materials). Extending to 3D [47], all lines along k_z containing X and M points (i.e., X–R and M–A) form degenerated lines called nodal lines (NLs). For example, in Figure S3, in the Supplementary Materials, we show forming of the NL along the X–R direction by the crossing of two bands. NLs are formed from the crossing of two Dirac-like bands. A similar situation is observed in the other Dirac semimetals [43,46,48–58].

In a general case, NLs can be observed experimentally, in the form of the bands crossing [59]. Its binding energy varies with k_z , which can be visualized by changing photon energy. In our case, NLs should be visible in the form of the band crossing at the \bar{X} points, where the bulk NLs from the X–R path are projected (Figure 3). Theoretical investigation of the bulk NLs recovers the existence of several gaps between them (marked by red areas in Figure 3d). For instance, NLs inside the upper band fill approximately the energy range from -0.7 to -0.5 eV below the Fermi level. In this range of energies, several k_z -depending band crossings are visible (see Figure 3c). Unfortunately, the exact band crossing is not well resolved in the experiment (top panels on Figure 3). However, the depletion of spectral intensity in the experiment is observed for binding energies around ~ -0.4 eV corresponding to the gaps at \bar{X} . Additionally, we observed excellent agreement of the experimental results with the theoretical ones (cf. top and bottom bands in Figure 3). These nodal lines are shown as blue lines in Figure 4, which presents the location of the nodal lines in the k-space.

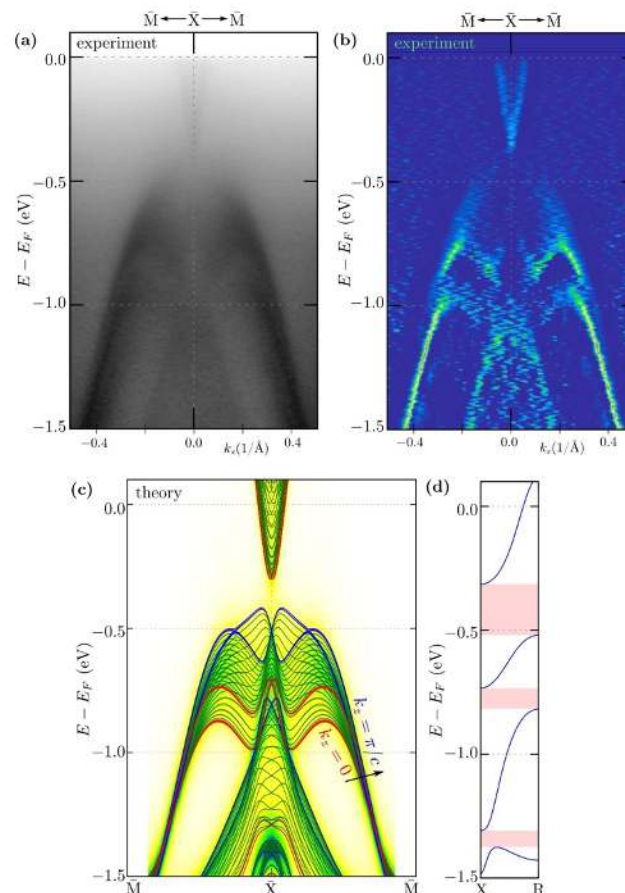


Figure 3. Comparison of the ARPES spectra (a) and corresponding 2D curvature (b) with the theoretical calculation: spectral function (background) and projected bulk bands (lines) (c). The results are presented along the \bar{X} – \bar{M} direction, around the \bar{X} point. The experimental data have been collected with photon energy $h\nu = 66$ eV at a temperature of 12 K. Panel (d) presents the energy range of the nodal lines in the bulk band structure along the X–R path (red areas mark the band gap between the nodal lines).

The SOC slightly lifts the degeneracy along the X–M and R–A lines. However, the highly degenerated nodal lines (e.g., places marked by pink arrows in Figure 2) also can be found in this direction, which is due to vanishing of the spin–orbit splitting for some k . These fourfold degenerated Dirac points lead to the emergence of an additional NL at the boundary of the Brillouin zone (in the X–M–A–R planes). The NLs are presented schematically in Figure 4 by green lines (we present NLs only for eight bands near the Fermi level). As we can see, some of the NLs create closed contours along k_z located near the A–M edge of the Brillouin zone. Contrary to this, other NLs form closed ellipsoidal contours around an R high-symmetry point.

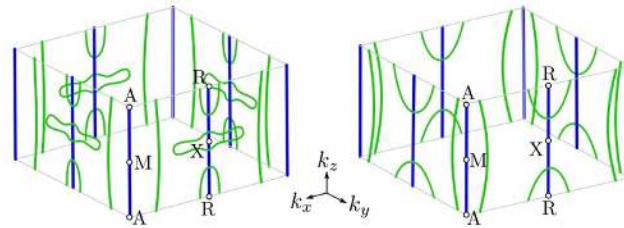


Figure 4. Location of nodal lines in k -space with respect to the first Brillouin zone (gray box). Actual, variable binding energy is not indicated. Blue solid lines are realized due to the system symmetry (sample range of energies are presented in Figure 3d). Similarly, green solid curves are realized as a consequence of the spin–orbit splitting vanishing at the Brillouin zone boundary (in X–R–A–M planes). Green lines are located at binding energies in ranges from -1 to -2 eV, and from -0.5 to -1.0 eV, for the left and right panels, respectively.

Fermi surface—The previous studies showed that the FS in the absence of the SOC (Figure 5) is composed of four bands [15,19,40,60]: two cylindrical-like pockets along the Γ –Z direction and two pockets with diamond-like shapes connecting the X points of the first Brillouin zone (separate pockets are shown in Figure S4 in the Supplementary Materials). Analyses of the band structure of the separate layers of LaAgSb₂, i.e., Sb and Ag square nets, and LaSb double-layer (cf. Figure S1 in the Supplementary Materials), clearly show that the pockets around the Γ –Z direction are associated with the LaSb double layer (mostly $5d$ orbitals of La and $5p$ orbitals of Sb). Similarly, the quasi-two dimensional Sb and Ag square nets create diamond-like pockets ($5s$ and $4d$ orbitals of Ag and $5p$ orbitals of Sb).

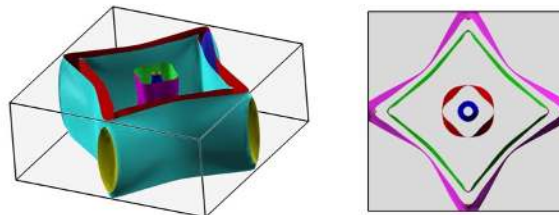


Figure 5. Three-dimensional and top view (left and right panels, respectively) of the Fermi surface of LaAgSb₂ in the absence of the spin–orbit coupling.

The isoenergetic study of the spectral function clearly shows that the characteristic shape of the FS is observed experimentally. A comparison of the experimental and theoretical results is presented in Figure 6 in the left and right panels, respectively. First, the ARPES result for the energy corresponding to the Fermi level E_F (Figure 6a) is clearly reproduced by the theoretical projected Fermi surface. Similarly as in the bulk system (Figure 5), we can find two pockets centered at the $\bar{\Gamma}$ point and two diamond-like pockets connecting the \bar{X} points. Our detection of the pocket around the $\bar{\Gamma}$ point is in agreement with the previous measurements for this material [61]. In both the experimental and theoretical results, we can find a few characteristic features. The internal $\bar{\Gamma}$ -centered pocket shows weak

k_z -dependence (theoretical spectral weight of this pocket has an approximately constant intensity). Contrary to this, the external $\bar{\Gamma}$ -centered pocket shows stronger k_z -dependence in the $\bar{\Gamma}$ - \bar{M} direction than in $\bar{\Gamma}$ - \bar{X} —this is well visible in the form of the increasing theoretical spectral weight along the second direction. The situation looks similar in the case of the diamond-like pockets. Here, we must mention that a similar diamond-like FS projection is observed also in the other Dirac semimetals within this family, e.g., LaCuSb₂ [62], YbMnBi₂ [63] and YbMnSb₂ [64], or SrMnBi₂ and CaMnBi₂ [65], as well as square-net materials [51], e.g., ZrSiTe [43], ZeSiS [52,55,56], ZrSnTe [57], ZrGeTe [58], HfSiS [49,50], ZrSiS [48,49], SmSbTe [54], LaSbTe [46], or NbGeSb [66].

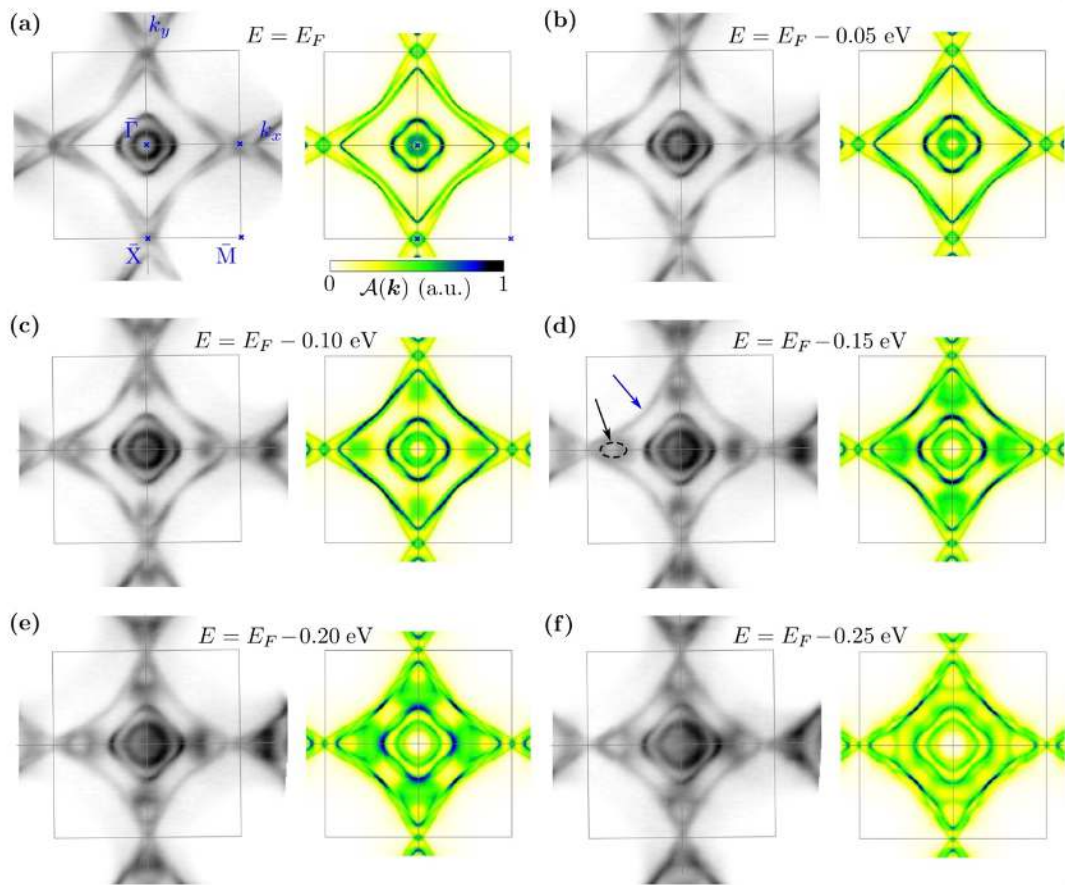


Figure 6. Comparison of the ARPES spectra obtained with a photon energy of 66 eV at a temperature of 12 K (left panels) with the theoretical surface spectral function (right panels) for selected binding energies E below the Fermi level (as labeled). The gray square denotes the Brillouin zone. The black arrow and the dashed outline indicate the additional branch explained by the spectral function.

The characteristic features for $E = E_F$ are conserved also below E_F . However, going below $E = E_F$, we can observe a few important behaviors. First, we notice the E dependence of two branches forming two diamond-like pockets of the FS (marked with the blue arrow at Figure 6d). Under decreasing E , we find the hourglass shape by the band branches (which will be discussed more precisely in the next paragraphs). Secondly, around $E = E_F - 0.1$ eV, we can observe the appearance of the parabolic-like branch in the band structure near the \bar{X} point. For lower E , this branch is well visible in the form of a circular shape in the spectral function (marked by black dashed lines and the black arrow in Figure 6d). For

$E = E_F - 0.25$ eV, this branch is linked to the diamond-like shape. It is worth mentioning that in the whole range of E , the theoretical calculations are comparable with the experimental ARPES results (cf. left and right panels in Figure 6a–f), which indicate the weak role of the electron correlations in this system in the considered energy scale.

With decreasing E , modification of the FS pocket around the \bar{X} point can be observed (Figure 6). This pocket is formed by a common part of two diamond-like pockets from the two nearest Brillouin zones. The change in the size of these pockets observed for the decreasing binding energy leads to the disappearance of the pocket crossing the border of the Brillouin zone (cf. panels from Figure 6a–f). Indeed, we can reveal this behavior carefully analyzing both experimental data and the theoretical spectral function along the \bar{X} – \bar{M} direction, i.e., at the Brillouin zone boundary (Figure 3c). The electron pocket crossing the Brillouin zone boundary vanishes around the energy ~ 0.35 eV below the Fermi level. Theoretical analyses show that the upper (electron) (above ~ -0.35 eV) and lower (hole) bands (below ~ -0.5 eV) are separated at the \bar{X} point by the ~ 0.15 eV band gap. The lower bands create a characteristic double parabolic structure corresponding to experimental results (Figure 3a).

3.3. Surface States within Direct DFT Slab Calculations

To evaluate the data described in the previous section, we performed the DFT calculation for slab geometry with different terminations (Figure 7), namely square net of Ag atoms (Figure 7a), square net of Sb atoms (Figure 7b), and two nonequivalent LaSb layers shown in Figure 7c,d. The structural models used in the DFT calculations are presented at the right side of the obtained band structures (Figure 7). Each time, ~ 10 Å of vacuum is included.

To extract the surface states, we compare calculated band structures of slabs (solid red lines) with the bulk band structures (solid gray lines) projected onto the 2D reduced Brillouin zone. In the case of the bulk bands, around the \bar{M} point, there exists a relatively large “gap” between continuum states which allows extracting the surface states in a relatively simple way. Indeed, in this region, the surface states are well visible. For three cases of chosen terminations, the surface states crossing the Fermi level are well visible around the \bar{M} point, where they form Dirac cones located either above (Figure 7a) or below (Figure 7c,d) E_F . In the case of Sb termination (Figure 7b), the surface states are deep below the Fermi level (around -1 eV). Similar states can be observed experimentally in some materials, such as NbGeSb [66]. The absence of such Dirac surface states at \bar{M} in the photoemission data would suggest the realization of the Sb or Ag square net termination. Similarly, only LaSb termination allows the realization of the surface states near E_F in the region of Γ point, as shown by blue arrows in Figure 7c,d. Nevertheless, the most interesting range of energies (around the Fermi level) corresponding to the paths $\bar{\Gamma}$ – \bar{X} and \bar{M} – $\bar{\Gamma}$ is filled by the bulk states. Contrary, e.g., to the topological insulators [4–8], the extraction of separate surface states can be hard or even impossible within the existing ARPES data due to the presence of bulk bands.

Role of surface termination—As we can see from the comparison of the results for different surface terminations, there exists a strong dependence of the realized surface states on a type of termination (cf. panels on Figure 7). Such behavior was reported before, e.g., in the case of Weyl semimetals [67]. At the same time, in each case, nearly linear bulk bands crossing the Fermi level are insensitive to the modification of termination. The same bulk bands play the most important role in the described earlier ARPES data due to the weak k_z dependence of the corresponding dispersion relations. To conclude this part, we can propose that the sample studied experimentally was terminated by the LaSb layer. However, the discussed surface states should be absent if the surface termination resulting from cleaving is different.

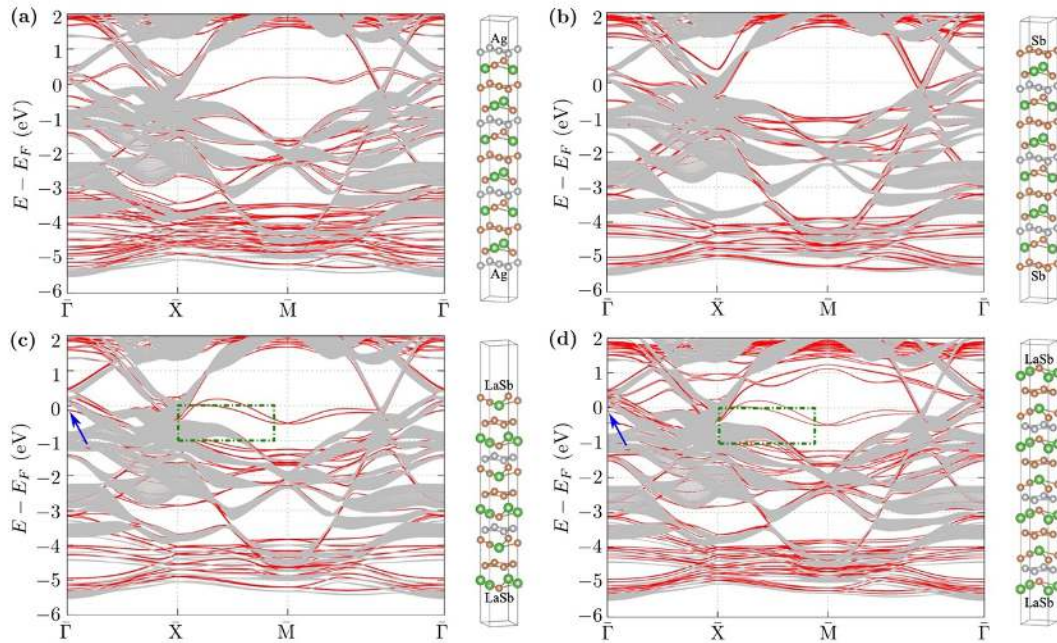


Figure 7. Band structures in slab geometry (with corresponding structures presented on right-hand side) dependent on the surface termination of Ag (a) and Sb (b) square nets and two possible terminations of the LaSb layer—conserving (c) and breaking (d) glide symmetry. Red lines denote the slab band structure from the DFT calculations, while gray lines denote the projected bulk band structure from tight binding models calculations (for eighty k_z different momenta). Blue arrows indicate the surface states below the Fermi level at the Γ point. The green dotted-dashed line in (c,d) shows the area presented in Figure 8.

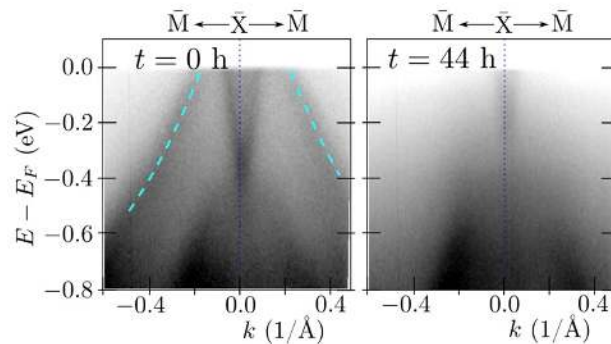


Figure 8. The ARPES results obtained around the \bar{X} point presenting the realized surface states. The panels present spectra collected at different time points following the sample cleaving. Cyan dashed lines highlight the surface state. The measurements have been realized with He-I ($h\nu = 21.218$ eV) radiation for the sample cleaved and measured at a temperature of 20 K.

From a theoretical point of view, the most favorable type of termination can be predicted by calculation of the binding energy within the DFT framework. To find this type of prediction, we calculated the binding energy ΔE between the adjacent layers: $\Delta E = E_{A+B} - E_A - E_B$, where E_{A+B} , E_A , and E_B denote the energy of products (A + B) and individual reactants (A and B), respectively. In practice, $E_A + E_B$ can be calculated when the last layer (B) is ~ 10 Å above substrate (A) with respect to the investigated surface

(A + B). The results of our calculation are collected in Table 1. As we can see, independently of the surface termination, the binding energy is always negative; i.e., there is no unique preferred termination.

Table 1. The comparison of the binding energies ΔE (as a difference between the energy of the surface E_{A+B} , and energy of individual reactants $E_A + E_B$) for different terminations (as labeled).

Termination		E_{A+B} (eV)	$E_A + E_B$ (eV)	ΔE (eV)
Ag term	[Figure 7a]	−99.00	−96.86	−2.14
Sb term	[Figure 7b]	−99.00	−96.67	−2.33
LaSb term	[Figure 7c,d]	−84.36	−82.55	−1.81

3.4. Surface States around $\bar{\Gamma}$ and \bar{X}

ARPES measurements, which visualize surface states better, were performed directly following the cleaving at 20 K. For this case, the ARPES spectra obtained along the \bar{X} – \bar{M} direction, around the \bar{X} point are presented in Figure 8. Now, we observe an additional band in the range of energies, where bulk states are not realized. This additional band disappeared much quicker compared to the rest of the structure (cf. left and right panels, presenting results at a different time following the cleaving of the crystal). What is important is that the decay time was different in different vacuum systems, namely from several minutes to tens of hours. This is a consequence of surface contamination by impurities from the environment. All this makes a strong suggestion that the described band is of surface origin. By comparing these results with the theoretical prediction, we can conclude that the LaSb termination is realized for this sample (cf. Figure 7c,d). A quick look at the crystal structure (Figure 1) leads to the conclusion that if LaSb termination results from cleaving, a neighboring layer of either Ag or Sb should also form another termination. The absence of the characteristic band of Ag termination in the ARPES spectra at the M point (Figure 7a) indicates that rather not Ag but Sb termination may be present as well. However, we do not have any direct proof of this assumption, and it is also not clear if another termination is ordered to form surface states.

The band structure along the $\bar{\Gamma}$ – \bar{X} direction is presented in Figure 9. As it can be seen, in the experimental spectra, we can well separate visible bands. The most intensive lines demonstrate the shape of the projected FS in a form of a pair of cylindrical pockets centered at $\bar{\Gamma}$ and a pair of diamond-like pockets (cf. Figure 5a). Additionally, exactly at the $\bar{\Gamma}$ point, around −0.2 eV, we can see the surface states in a form of the parabolic-like band (highlighted by a dashed white line in Figure 9i). Observation of this surface state is in agreement with the direct DFT calculations (cf. discussion in Section 3.3) and surface Green function calculations (surface state is marked by blue arrow in Figure 9b).

Additionally, examination of the band structure along the $\bar{\Gamma}$ – \bar{X} direction uncovers also other features of the band structure discussed earlier. The NLs are visible as a crossing of the bands at the \bar{X} point. This crossing is visible independently of the energy of photons used during the ARPES experiment (red dashed lines on right panels in Figure 9). ARPES scans with variable photon energy yield constant energy intensity maps as a function of $k_{\perp} = k_z$ and $k_{\parallel} = k_x$ (perpendicular and parallel to the surface component of the wave vector) in the $\bar{\Gamma}$ – \bar{X} – \bar{R} – \bar{Z} plane, and the data are compared to the calculated spectral function (see from Figure 9c–f). The data are shown for E_F (cf. Figure 9c,d) and −0.2 eV below E_F (cf. Figure 9e,f). The spectra have been collected for photon energies in the range from 20 to 84 eV, and k_{\perp} was obtained with the assumed inner potential of $V_0 = 15$ eV. The comparison of the spectra and theory may indicate the actual assignment of high symmetry points as proposed in Figure 9c–f. Taking into account this last result, as well as the excellent agreement of experimental and theoretical data (e.g., Figure 3), we conclude that the $h\nu = 66$ eV corresponds to the k_z close to the $\bar{\Gamma}$ – \bar{X} – \bar{M} plane. Indeed, the existence of the band crossing independently on k_{\perp} confirms the realization of NL at \bar{X} (which has been discussed earlier).

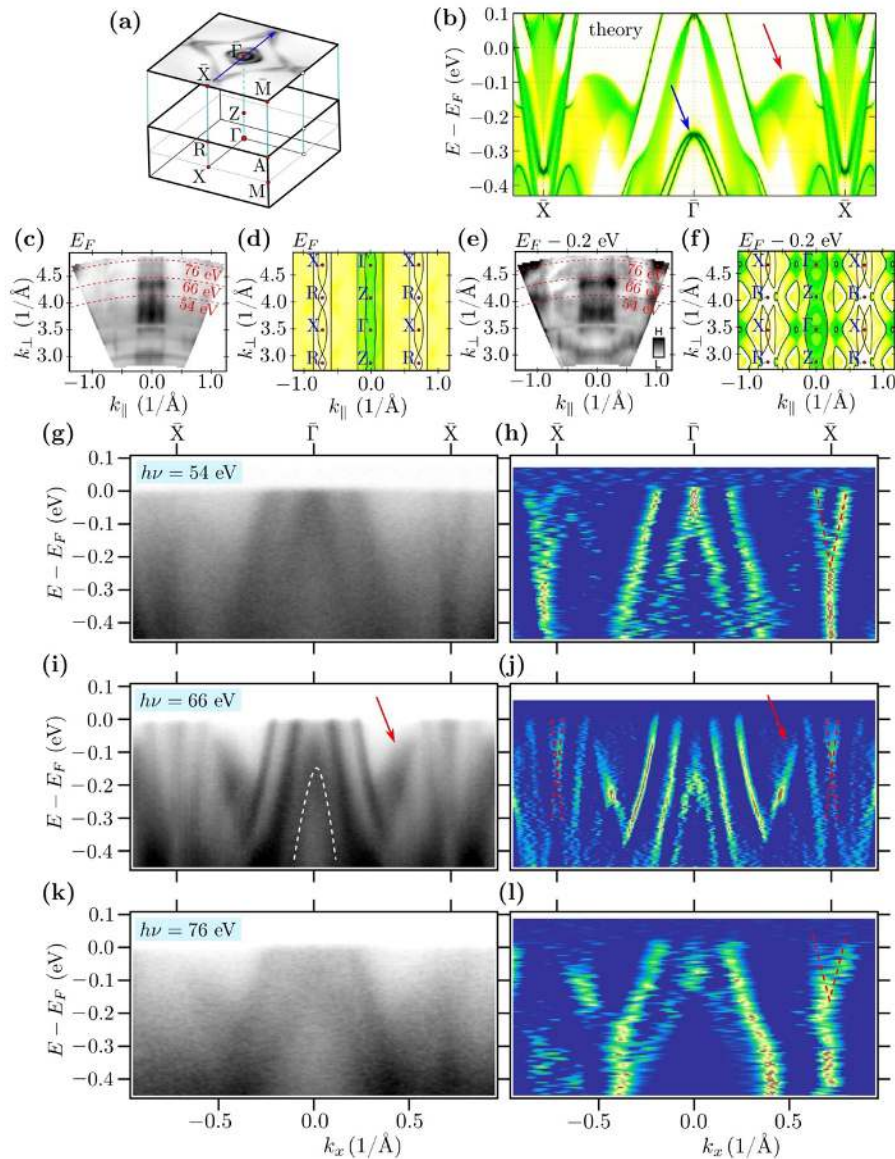


Figure 9. Cartoon representation of the bulk first Brillouin zone projection into the surface Brillouin zone (a). Theoretical surface spectral function along the \bar{X} - Γ - \bar{X} direction (b). Panels from (c–f) present intensity plots for constant energy planes at the Fermi level E_F and energy $E_F - 0.2$ eV (as labeled). The ARPES spectra (c,e) were collected in the photon energy range from 20 to 80 eV. The calculated band structure (solid black lines) along with the spectral function (background color scale) is shown in (d,f). Here, the intensity maps is a function of $k_{\perp} = k_z$ and $k_{\parallel} = k_x$ (perpendicular and parallel to the surface component of the wave vector). Panels (g–l) present experimentally obtained spectra and their 2D curvature (left and right panels, respectively) for different photon energies (as labeled). The red arrows in (b,i,j) indicate the position of additional structure in the spectra that can be explained by the projection of the bulk band on the surface Brillouin zone. The blue arrow in (b) and white dashed parabola in (i) indicate the surface state. The red dashed lines in (h,j,l) refer to the position of the band crossing of the band forming the nodal line. The measurements were made at the temperature of 12 K.

Moreover, around -0.1 eV, we can observe a blurred shape (marked by the red arrow in Figure 9i). The theoretical study clearly shows that the additional structure in the spectra can be explained by the projection of the bulk band on the surface Brillouin zone. Indeed, the calculated spectral function confirms this explanation (cf. red arrow in Figure 9b). This structure was also observed in the form of a cylindrical shape in the isoenergetic cuts (e.g., marked by a black arrow in Figure 6d).

3.5. Surface States along $\bar{\Gamma}$ - \bar{M}

In the bulk band structure, there exist several places where the SOC leads to opening of the gap between initially crossed bands. Many of them are located along the $\bar{\Gamma}$ - \bar{M} and \bar{Z} - \bar{R} paths with energies close to the Fermi level. The previous study of Shi et al. [25] suggested the realization of the Dirac cone-like structure in the vicinity of the Fermi level formed by the crossing of two linear energy bands. In this section, we present a complex study of the electronic band structure, based on theoretical and experimental results, along different cuts parallel to $\bar{\Gamma}$ - \bar{M} (Figure 10).

The surface Green function and slab band structure are presented in Figure 10b (left and right half, respectively). The crossing of the linear bands around -0.15 eV is well visible in both results (marked by blue dashed ellipses). Projection of the bulk electronic bands on the surface Brillouin zone directly presents the k_z dependence of separate bands (Figure 10c). Independently of k_z , the direct gap is realized in the bulk (around $k_x = k_y \simeq 0.2 \times 2\pi/a$). The value of this gap can be estimated as ~ 5 meV, which can be seen in a high-resolution ARPES experiment. Additionally, this gap changes its value for directions away from the $\bar{\Gamma}$ - \bar{M} path (cf. Figure S6 in the Supplementary Materials). Moreover, the bulk gap is shifted from energy -0.125 to -0.225 eV below the Fermi level.

Direct analysis of the band in slab geometry (including both LaSb and Sb terminations) is presented in Figure 10d, where the color of line denotes the contribution of the surface or bulk states (red and gray color, respectively). As previously, the surface states at the $\bar{\Gamma}$ point are visible, which is realized in a system with the LaSb termination. The other surface state (marked by the blue arrow) is realized by the second surface of the slab, which is terminated by the Sb square net. Here, we should have in mind that only LaSb termination was directly indicated by ARPES for our system. Indeed, the surface Green function calculated for the LaSb termination (Figure 10e) correctly reproduces the surface state found at the $\bar{\Gamma}$ point. At the same time, the other surface state is not observed. The corresponding experimental results for different cuts are presented in panels from Figure 10f–k. Firstly, we observe the disappearance of the surface state at the $\bar{\Gamma}$ point (red dashed line in Figure 10f) while moving away from the $\bar{\Gamma}$ - \bar{M} direction. Secondly, we observe a strong momentum-dependence of the bands forming central pockets of the FSs (two blue dashed lines in Figure 10f). For instance, at the cut 4, which crosses only the external $\bar{\Gamma}$ -centered FS, we clearly see the shift of the internal branches to lower energies. Two branches corresponding to the diamond-like part of the FS (marked by two red arrows in Figure 10f) also yield slightly different dispersions. These two branches should play a role in the realization of the discussed surface state. Directly along the $\bar{\Gamma}$ - \bar{M} direction (cut 1), a cross-like structure is visible. Away from this cut, the open gap becomes more visible, where the bottom of the upper branches is visible (marked by a green arrow in Figure 10k).

The surface Green function correctly reproduces the experimental results. In both cases, the surface state closing the gap is not visible.

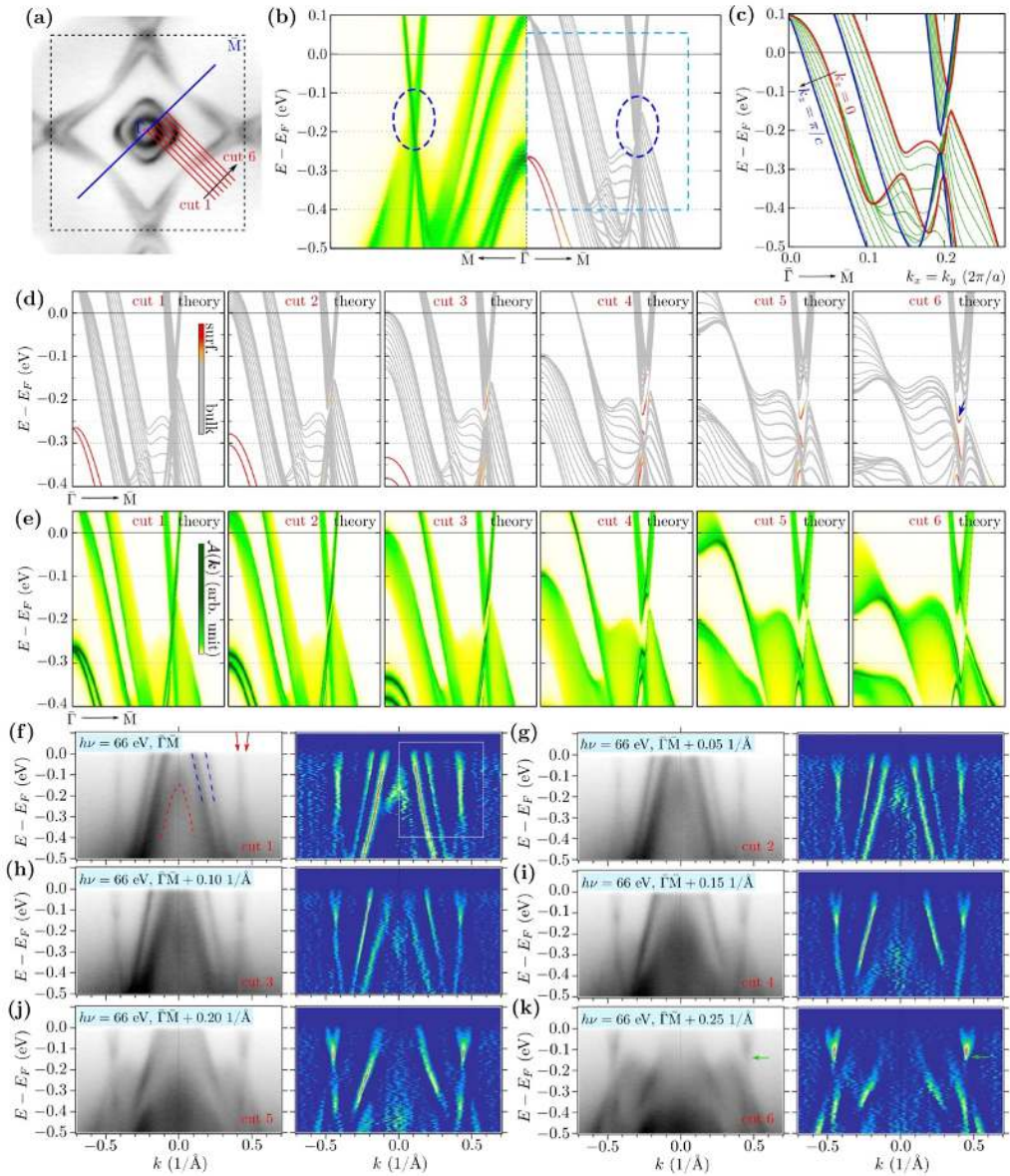


Figure 10. The electronic band structure along a series of paths presented in (a). Theoretical spectral function (left) and band structure (right) along the Γ - \bar{M} path for a finite system (b) and related bulk band structure (c). Panels (d) present band structures calculated for the slab geometry including both LaSb and Sb terminations along different cuts shown in (a). Bands with red (gray) color correspond to the surface (bulk) states. Theoretical prediction of the spectral function within the surface Green's function calculation for LaSb termination along different cuts from (a) is presented in (d). Panels (d,e) correspond to the range of parameters marked by boxes in (b,f). Panels (f-k) show the experimental spectra recorded with the ARPES measurements with $h\nu = 66$ eV at a temperature of 12 K (left panels) and their 2D curvatures (right panels) along different cuts from (a). The blue dashed lines in (f) indicate the bands forming central pockets of the FSs, while the red dashed line refers to the surface state. The red arrows in (f) indicate the position of the band corresponding to the diamond-like part of the FS, and the green arrows in (k) point to the bottom of the band above the energy gap related to the blue arrow on cut 6, i.e., panel (d).

4. Summary

In this paper, we have performed the systematic high-resolution ARPES measurements on LaAgSb₂ covering a large area of the Brillouin zone. The presented experimental results were supported by the theoretical analyses, within the ab initio (DFT) calculations, as well as by the tight binding model formulation. Both theoretical techniques allow for excellent reproduction of the experimentally observed band structure of LaAgSb₂ (cf. Section 3.2). Nodal lines related to the symmetry of the system are shown in calculations, and the corresponding ARPES spectra are obtained. Moreover, analyses of the band structure uncover the highly degenerated nodal lines, the existence of which is not a consequence of the $P4/nmm$ symmetry. These nodal lines occur due to vanishing the spin-orbit splitting, and they are located at the boundary of the Brillouin zone.

Direct studies of the system with slab geometry indicate a possibility of realization of the surface states in this compound (Section 3.3). We conclude that the appearance of the surface states strongly depends on the termination. For instance, the surface states can be realized in the form of well visible separate parabolic-like bands when the sample is not terminated by the Sb layer. Indeed, our experimental data confirm this theoretical prediction (Section 3.4). We find the surface states at the Γ and X points in the form of parabolic-like bands. However, this state disappears relatively fast due to the adsorption of surface contamination. Nevertheless, the observed surface states at the Γ and X points indicate the LaSb termination of the studied sample.

Finally, we verified if the Dirac surface states can be found along the Γ -M direction. Careful analysis of this problem was presented in Section 3.5. The theoretical examination of the band structure clearly shows that the Dirac surface state can appear only at the Sb square net termination, in contrast to the LaSb termination found in our samples. As a consequence, the Dirac surface states along Γ -M are not observed. Similar results can be obtained for the surface Green function analyses, where the surface state is also absent.

Supplementary Materials: The following supporting information can be downloaded at: <https://www.mdpi.com/article/10.3390/ma15207168/s1>, Figure S1: the bulk electronic band structure related to layers forming LaAgSb₂ structure; Figure S2: the Dirac points at X and M, Figure S3: nodal lines formed along X-R line, Figure S4: Fermi surface branches shown separately, Figure S5: comparison of the band structures in $P4/nmm$ (not realized in reality, SG:123) and $P4/mmm$ (SG:129) showing impact of the mirror symmetry and glide symmetry, Figure S6: the bulk electronic band structure along Γ -M path for $k_z = 0$ and $k_z = \pi/c$.

Author Contributions: P.S. initiated the project; Z.B. growth of single crystals; M.R. and N.O. realization of the ARPES measurements; A.P. and P.P. realization of the ab initio (DFT) calculations; A.P. realization of the surface states calculations; A.P. writing—original draft preparation; M.R., P.S., P.P. and A.P. writing—review and editing; M.R. and A.P. visualization; M.R., N.O., Z.B., P.P., P.S. and A.P. discussion. All authors have read and agreed to the published version of the manuscript.

Funding: Support of the Polish Ministry of Science and Higher Education under the grant N17/MNS/000039 is acknowledged. This work was supported by the National Science Centre (NCN, Poland) under grants No. 2017/25/B/ST3/02586 (P.P.) and 2017/24/C/ST3/00276 (A.P.).

Institutional Review Board Statement: Not applicable.

Informed Consent Statement: Not applicable.

Data Availability Statement: Not applicable.

Acknowledgments: Some figures in this work were rendered using VESTA (version 3.5.7) [68] and xCRYSDEN (version 1.5.60) [69]. A.P. appreciates funding in the frame of scholarships of the Minister of Science and Higher Education (Poland) for outstanding young scientists (2019 edition, no. 818/STYP/14/2019).

Conflicts of Interest: The authors declare no conflict of interest.

Appendix A. Tight Binding Model in Maximally Localized Wannier Orbitals Basis

Using results of the DFT calculation for electronic band structure we can find the tight binding model in the basis of the maximally localized Wannier orbitals [70–72]. It can be performed via the WANNIER90 software (version 3.0.0) [73–75]. As a result of this we can find the parameters of the tight binding Hamiltonian of free electrons in the form:

$$\mathcal{H} = \sum_{\mathbf{R}, \mathbf{R}'} \sum_{\mu, \mu'} \sum_{\sigma, \sigma'} t_{\mathbf{R}\mu\sigma, \mathbf{R}'\mu'\sigma'} c_{\mathbf{R}\mu\sigma}^\dagger c_{\mathbf{R}'\mu'\sigma'}, \quad (\text{A1})$$

where $c_{\mathbf{R}\mu\sigma}^\dagger$ ($c_{\mathbf{R}\mu\sigma}$) denotes the creation (annihilation) operator of the electron with spin σ at μ orbital localized on atom in \mathbf{R} position. Here $t_{\mathbf{R}\mu\sigma, \mathbf{R}'\mu'\sigma'}$ for $\sigma = \sigma'$ ($\sigma \neq \sigma'$) denotes the spin conserved (spin flip) hopping integrals between orbitals $\mathcal{O}_1 = (\mathbf{R}\mu)$ and $\mathcal{O}_2 = (\mathbf{R}'\mu')$. We should notice that the spin flip hopping part corresponds to the SOC, i.e., mixing of the different type of spin subspaces. From this, the normal states in momentum space can be rewritten in the matrix form:

$$\mathbb{H}_{\mu\sigma, \mu'\sigma'}(\mathbf{k}) = \sum_{\mathbf{d}} \exp(i\mathbf{k} \cdot \mathbf{d}) t_{\mathbf{R}\mu\sigma, \mathbf{R}'\mu'\sigma'}, \quad (\text{A2})$$

where $\mathbf{d} = \mathbf{R} - \mathbf{R}'$ is the real-space distance between orbital \mathcal{O}_1 and \mathcal{O}_2 . The band structure for a given \mathbf{k} -point can be found by diagonalization of the matrix $\mathbb{H}(\mathbf{k})$.

In our case, the tight binding model was found from the $8 \times 8 \times 6$ full \mathbf{k} -point DFT calculation, starting from p orbitals of Sb, as well as d orbitals of Ag and La. This gives us 32-orbital tight binding model of the LaAgSb₂. Comparison of the band structure obtained from the DFT and tight binding model can be found in Figure A1, while the Wannier (maximally localized) orbitals are presented in Figure A2.

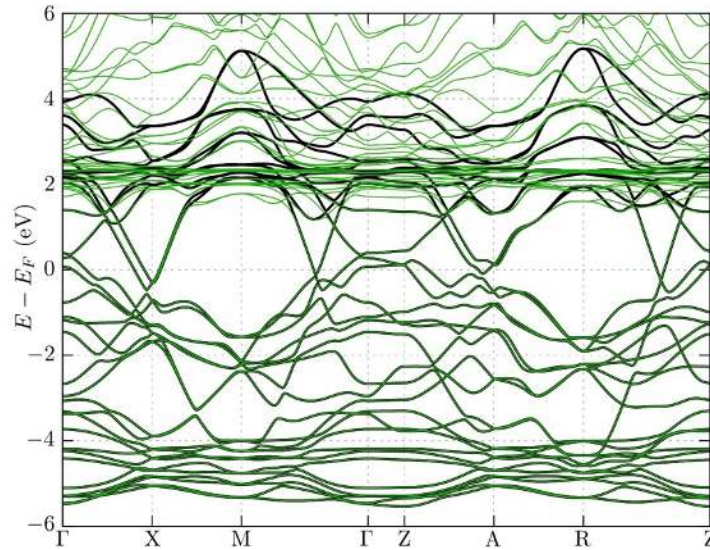


Figure A1. The comparison of the band structure obtained from the DFT calculations (green lines) and tight binding model (black lines).

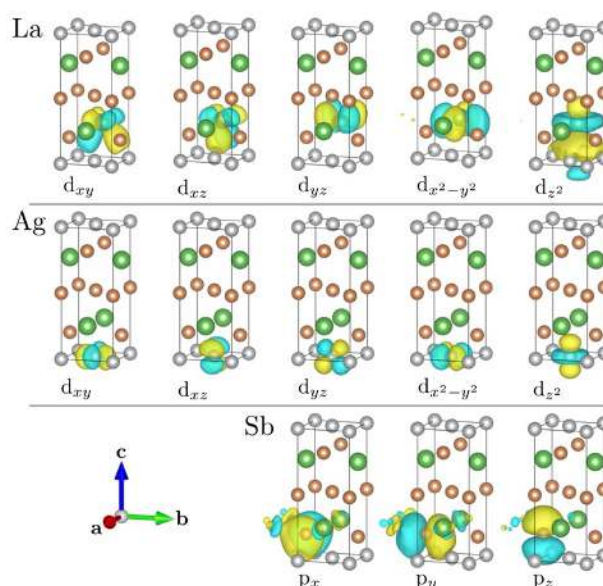


Figure A2. The final form of the maximally localized Wannier orbitals, found during procedure of the DFT band structure wannierization. Groups from top to bottom correspond to d -like orbitals of Ag and La, and p -like orbitals of Sb, as labeled.

References

- Hasan, M.Z.; Kane, C.L. *Colloquium: Topological insulators*. *Rev. Mod. Phys.* **2010**, *82*, 3045. [[CrossRef](#)]
- Qi, X.L.; Zhang, S.C. *Topological insulators and superconductors*. *Rev. Mod. Phys.* **2011**, *83*, 1057. [[CrossRef](#)]
- Sato, M.; Ando, Y. *Topological superconductors: A review*. *Rep. Prog. Phys.* **2017**, *80*, 076501. [[CrossRef](#)] [[PubMed](#)]
- Hsieh, D.; Xia, Y.; Qian, D.; Wray, L.; Meier, F.; Dil, J.H.; Osterwalder, J.; Patthey, L.; Fedorov, A.V.; Lin, H.; et al. *Observation of Time-Reversal-Protected Single-Dirac-Cone Topological-Insulator States in Bi_2Te_3 and Sb_2Te_3* . *Phys. Rev. Lett.* **2009**, *103*, 146401. [[CrossRef](#)]
- Zhang, H.; Liu, C.X.; Qi, X.L.; Dai, X.; Fang, Z.; Zhang, S.C. *Topological insulators in Bi_2Se_3 , Bi_2Te_3 and Sb_2Te_3 with a single Dirac cone on the surface*. *Nat. Phys.* **2009**, *5*, 438. [[CrossRef](#)]
- Xia, Y.; Qian, D.; Hsieh, D.; Wray, L.; Pal, A.; Lin, H.; Bansil, A.; Grauer, D.; Hor, Y.S.; Cava, R.J.; et al. *Observation of a large-gap topological-insulator class with a single Dirac cone on the surface*. *Nat. Phys.* **2009**, *5*, 398. [[CrossRef](#)]
- Alpichshev, Z.; Analytis, J.G.; Chu, J.H.; Fisher, I.R.; Chen, Y.L.; Shen, Z.X.; Fang, A.; Kapitulnik, A. *STM Imaging of Electronic Waves on the Surface of Bi_2Te_3 : Topologically Protected Surface States and Hexagonal Warping Effects*. *Phys. Rev. Lett.* **2010**, *104*, 016401. [[CrossRef](#)]
- Kuroda, K.; Arita, M.; Miyamoto, K.; Ye, M.; Jiang, J.; Kimura, A.; Krasovskii, E.E.; Chulkov, E.V.; Iwasawa, H.; Okuda, T.; et al. *Hexagonally Deformed Fermi Surface of the 3D Topological Insulator Bi_2Se_3* . *Phys. Rev. Lett.* **2010**, *105*, 076802. [[CrossRef](#)]
- Armitage, N.P.; Mele, E.J.; Vishwanath, A. *Weyl and Dirac semimetals in three-dimensional solids*. *Rev. Mod. Phys.* **2018**, *90*, 015001. [[CrossRef](#)]
- Schoop, L.M.; Pielhofer, F.; Lotsch, B.V. *Chemical Principles of Topological Semimetals*. *Chem. Mater.* **2018**, *30*, 3155. [[CrossRef](#)]
- Klemenz, S.; Lei, S.; Schoop, L.M. *Topological Semimetals in Square-Net Materials*. *Annu. Rev. Mater. Res.* **2019**, *49*, 185. [[CrossRef](#)]
- Song, C.; Park, J.; Koo, J.; Lee, K.B.; Rhee, J.Y.; Bud'ko, S.L.; Canfield, P.C.; Harmon, B.N.; Goldman, A.I. *Charge-density-wave orderings in LaAgSb_2 : An x-ray scattering study*. *Phys. Rev. B* **2003**, *68*, 035113. [[CrossRef](#)]
- Chen, R.Y.; Zhang, S.J.; Zhang, M.Y.; Dong, T.; Wang, N.L. *Revealing Extremely Low Energy Amplitude Modes in the Charge-Density-Wave Compound LaAgSb_2* . *Phys. Rev. Lett.* **2017**, *118*, 107402. [[CrossRef](#)]
- Lue, C.S.; Tao, Y.F.; Sivakumar, K.M.; Kuo, Y.K. *Weak charge-density-wave transition in LaAgSb_2 investigated by transport, thermal, and NMR studies*. *J. Phys. Condens. Matter* **2007**, *19*, 406230. [[CrossRef](#)]
- Bosak, A.; Souliou, S.M.; Faugeras, C.; Heid, R.; Molas, M.R.; Chen, R.Y.; Wang, N.L.; Potemski, M.; Le Tacon, M. *Evidence for nesting-driven charge density wave instabilities in the quasi-two-dimensional material LaAgSb_2* . *Phys. Rev. Res.* **2021**, *3*, 033020. [[CrossRef](#)]

16. Akiba, K.; Nishimori, H.; Umeshita, N.; Kobayashi, T.C. Successive destruction of charge density wave states by pressure in LaAgSb₂. *Phys. Rev. B* **2021**, *103*, 085134. [[CrossRef](#)]
17. Bud'ko, S.L.; Wiener, T.A.; Ribeiro, R.A.; Canfield, P.C.; Lee, Y.; Vogt, T.; Lacerda, A.H. Effect of pressure and chemical substitutions on the charge-density-wave in LaAgSb₂. *Phys. Rev. B* **2006**, *73*, 184111. [[CrossRef](#)]
18. Torikachvili, M.S.; Bud'ko, S.L.; Law, S.A.; Tillman, M.E.; Mun, E.D.; Canfield, P.C. Hydrostatic pressure study of pure and doped La_{1-x}R_xAgSb₂ (R = Ce, Nd) charge-density-wave compounds. *Phys. Rev. B* **2007**, *76*, 235110. [[CrossRef](#)]
19. Myers, K.D.; Bud'ko, S.L.; Antropov, V.P.; Harmon, B.N.; Canfield, P.C.; Lacerda, A.H. de Haas-van Alphen and Shubnikov-de Haas oscillations in RAgSb₂ (R = Y, La–Nd, Sm). *Phys. Rev. B* **1999**, *60*, 13371. [[CrossRef](#)]
20. Myers, K.D.; Bud'ko, S.L.; Fisher, I.R.; Islam, Z.; Kleinke, H.; Lacerda, A.H.; Canfield, P.C. Systematic study of anisotropic transport and magnetic properties of RAgSb₂ (R = Y, La–Nd, Sm, Gd–Tm). *J. Magn. Magn. Mater.* **1999**, *205*, 27. [[CrossRef](#)]
21. Wang, K.; Petrovic, C. Multiband effects and possible Dirac states in LaAgSb₂. *Phys. Rev. B* **2012**, *86*, 155213. [[CrossRef](#)]
22. Park, J.; Lee, G.; Wolff-Fabris, F.; Koh, Y.Y.; Eom, M.J.; Kim, Y.K.; Farhan, M.A.; Jo, Y.J.; Kim, C.; Shim, J.H.; et al. Anisotropic Dirac Fermions in a Bi Square Net of SrMnBi₂. *Phys. Rev. Lett.* **2011**, *107*, 126402. [[CrossRef](#)]
23. Wang, K.; Graf, D.; Lei, H.; Tozer, S.W.; Petrovic, C. Quantum transport of two-dimensional Dirac fermions in SrMnBi₂. *Phys. Rev. B* **2011**, *84*, 220401(R). [[CrossRef](#)]
24. Wang, J.K.; Zhao, L.L.; Yin, Q.; Kotliar, G.; Kim, M.S.; Aronson, M.C.; Morosan, E. Layered transition-metal pnictide SrMnBi₂ with metallic blocking layer. *Phys. Rev. B* **2011**, *84*, 064428. [[CrossRef](#)]
25. Shi, X.; Richard, P.; Wang, K.; Liu, M.; Matt, C.E.; Xu, N.; Dhaka, R.S.; Ristic, Z.; Qian, T.; Yang, Y.F.; et al. Observation of Dirac-like band dispersion in LaAgSb₂. *Phys. Rev. B* **2016**, *93*, 081105(R). [[CrossRef](#)]
26. Bukowski, Z.; Tran, V.; Stepień-Damm, J.; Troć, R. Single crystal growth, crystal structure characterization and magnetic properties of UCo_{0.5}Sb₂. *J. Solid State Chem.* **2004**, *177*, 3934. [[CrossRef](#)]
27. Zhang, P.; Richard, P.; Qian, T.; Xu, Y.M.; Dai, X.; Ding, H. A precise method for visualizing dispersive features in image plots. *Rev. Sci. Instrum.* **2011**, *82*, 043712. [[CrossRef](#)]
28. Blöchl, P.E. Projector augmented-wave method. *Phys. Rev. B* **1994**, *50*, 17953. [[CrossRef](#)] [[PubMed](#)]
29. Kresse, G.; Hafner, J. Ab initio molecular-dynamics simulation of the liquid-metal–amorphous-semiconductor transition in germanium. *Phys. Rev. B* **1994**, *49*, 14251. [[CrossRef](#)] [[PubMed](#)]
30. Kresse, G.; Furthmüller, J. Efficient iterative schemes for ab initio total-energy calculations using a plane-wave basis set. *Phys. Rev. B* **1996**, *54*, 11169. [[CrossRef](#)] [[PubMed](#)]
31. Kresse, G.; Joubert, D. From ultrasoft pseudopotentials to the projector augmented-wave method. *Phys. Rev. B* **1999**, *59*, 1758. [[CrossRef](#)]
32. Perdew, J.P.; Burke, K.; Ernzerhof, M. Generalized Gradient Approximation Made Simple. *Phys. Rev. Lett.* **1996**, *77*, 3865. [[CrossRef](#)]
33. Steiner, S.; Khmelevskiy, S.; Marsmann, M.; Kresse, G. Calculation of the magnetic anisotropy with projected-augmented-wave methodology and the case study of disordered Fe_{1-x}Co_x alloys. *Phys. Rev. B* **2016**, *93*, 224425. [[CrossRef](#)]
34. Monkhorst, H.J.; Pack, J.D. Special points for Brillouin-zone integrations. *Phys. Rev. B* **1976**, *13*, 5188. [[CrossRef](#)]
35. Sancho, M.P.L.; Sancho, J.M.L.; Sancho, J.M.L.; Rubio, J. Highly convergent schemes for the calculation of bulk and surface Green functions. *J. Phys. F: Met. Phys.* **1985**, *15*, 851. [[CrossRef](#)]
36. Wu, Q.S.; Zhang, S.N.; Song, H.F.; Troyer, M.; Soluyanov, A.A. WannierTools: An open-source software package for novel topological materials. *Comput. Phys. Commun.* **2018**, *224*, 405. [[CrossRef](#)]
37. Thirion, F.; Venturini, G.; Malaman, B.; Steinmetz, J.; Roques, B. Structures cristallines de Zr₆Cu₈Si₁₂ et Hf₂CuGe₄ et caractérisation d'une famille de composés semimétalliques "pseudolamellaires" de formule ZrSi₂Cu_x où x = 0,5, 1 et 1,33. *J. Less Common Met.* **1983**, *95*, 47. [[CrossRef](#)]
38. Brylak, M.; Möller, M.H.; Jeitschko, W. Ternary Arsenides ACuAs₂ and Ternary Antimonides AAgSb₂ (A = Rare-Earth Elements and Uranium) with HfCuSi₂-Type Structure. *J. Solid State Chem.* **1995**, *115*, 305. [[CrossRef](#)]
39. Gondek, L.; Penc, B.; Szytuła, A.; Stusser, N. Thermal dependence of the lattice constants of LaAgSb₂. *J. Alloys Compd.* **2002**, *346*, 80. [[CrossRef](#)]
40. Hase, I.; Yanagisawa, T. Electronic Band Calculation of LaTSb₂ (T = Cu, Ag, Au). *Phys. Procedia* **2014**, *58*, 42. [[CrossRef](#)]
41. Ruszafa, P.; Winiarski, M.J.; Samsel-Czekala, M. Dirac-Like Electronic-Band Dispersion of LaSb₂ Superconductor and Its Counterpart LaAgSb₂. *Acta Phys. Pol. A* **2020**, *138*, 748. [[CrossRef](#)]
42. Setyawan, W.; Curtarolo, S. High-throughput electronic band structure calculations: Challenges and tools. *Comput. Mater. Sci.* **2010**, *49*, 299. [[CrossRef](#)]
43. Topp, A.; Lippmann, J.M.; Varykhalov, A.; Duppel, V.; Lotsch, B.V.; Ast, C.R.; Schoop, L.M. Non-symmorphic band degeneracy at the Fermi level in ZrSiTe. *New J. Phys.* **2016**, *18*, 125014. [[CrossRef](#)]
44. Yang, S.Y.; Yang, H.; Derunova, E.; Parkin, S.S.P.; Yan, B.; Ali, M.N. Symmetry demanded topological nodal-line materials. *Adv. Phys. X* **2018**, *3*, 1414631. [[CrossRef](#)]
45. Klemenz, S.; Schoop, L.; Cano, J. Systematic study of stacked square nets: From Dirac fermions to material realizations. *Phys. Rev. B* **2020**, *101*, 165121. [[CrossRef](#)]

46. Wang, Y.; Qian, Y.; Yang, M.; Chen, H.; Li, C.; Tan, Z.; Cai, Y.; Zhao, W.; Gao, S.; Feng, Y.; et al. Spectroscopic evidence for the realization of a genuine topological nodal-line semimetal in LaSbTe. *Phys. Rev. B* **2021**, *103*, 125131. [[CrossRef](#)]
47. Young, S.M.; Kane, C.L. Dirac Semimetals in Two Dimensions. *Phys. Rev. Lett.* **2015**, *115*, 126803. [[CrossRef](#)]
48. Fu, B.B.; Yi, C.J.; Zhang, T.T.; Caputo, M.; Ma, J.Z.; Gao, X.; Lv, B.Q.; Kong, L.Y.; Huang, Y.B.; Richard, P.; et al. Dirac nodal surfaces and nodal lines in ZrSiS. *Sci. Adv.* **2019**, *5*, eaau6459. [[CrossRef](#)] [[PubMed](#)]
49. Chen, C.; Xu, X.; Jiang, J.; Wu, S.C.; Qi, Y.P.; Yang, L.X.; Wang, M.X.; Sun, Y.; Schröter, N.B.M.; Yang, H.F.; et al. Dirac line nodes and effect of spin-orbit coupling in the nonsymmorphic critical semimetals MSiS ($M = \text{Hf, Zr}$). *Phys. Rev. B* **2017**, *95*, 125126. [[CrossRef](#)]
50. Takane, D.; Wang, Z.; Souma, S.; Nakayama, K.; Trang, C.X.; Sato, T.; Takahashi, T.; Ando, Y. Dirac-node arc in the topological line-node semimetal HfSiS. *Phys. Rev. B* **2016**, *94*, 121108(R). [[CrossRef](#)]
51. Hosen, M.M.; Dimitri, K.; Belopolski, I.; Maldonado, P.; Sankar, R.; Dhakal, N.; Dhakal, G.; Cole, T.; Oppeneer, P.M.; Kaczorowski, D.; et al. Tunability of the topological nodal-line semimetal phase in ZrSiX-type materials ($X = \text{S, Se, Te}$). *Phys. Rev. B* **2017**, *95*, 161101(R). [[CrossRef](#)]
52. Topp, A.; Queiroz, R.; Grüneis, A.; MÜchler, L.; Rost, A.W.; Varykhalov, A.; Marchenko, D.; Krivenkov, M.; Rodolakis, F.; McChesney, J.L.; et al. Surface Floating 2D Bands in Layered Nonsymmorphic Semimetals: ZrSiS and Related Compounds. *Phys. Rev. X* **2017**, *7*, 041073. [[CrossRef](#)]
53. Schoop, L.M.; Topp, A.; Lippmann, J.; Orlandi, F.; MÜchler, L.; Vergniori, M.G.; Sun, Y.; Rost, A.W.; Duppel, V.; Krivenkov, M.; et al. Tunable Weyl and Dirac states in the nonsymmorphic compound CeSbTe. *Sci. Adv.* **2018**, *4*, eaar2317. [[CrossRef](#)]
54. Regmi, S.; Dhakal, G.; Kabeer, F.C.; Harrison, N.; Kabir, F.; Sakhya, A.P.; Gofryk, K.; Kaczorowski, D.; Oppeneer, P.M.; Neupane, M. Observation of multiple nodal lines in SmSbTe. *Phys. Rev. Mater.* **2022**, *6*, L031201. [[CrossRef](#)]
55. Schoop, L.M.; Ali, M.N.; Straßer, C.; Topp, A.; Varykhalov, A.; Marchenko, D.; Duppel, V.; Parkin, S.S.P.; Lotsch, B.V.; Ast, C.R. Dirac cone protected by non-symmorphic symmetry and three-dimensional Dirac line node in ZrSiS. *Nat. Commun.* **2016**, *7*, 11696. [[CrossRef](#)]
56. Neupane, M.; Belopolski, I.; Hosen, M.M.; Sanchez, D.S.; Sankar, R.; Szlawska, M.; Xu, S.Y.; Dimitri, K.; Dhakal, N.; Maldonado, P.; et al. Observation of topological nodal fermion semimetal phase in ZrSiS. *Phys. Rev. B* **2016**, *93*, 201104(R). [[CrossRef](#)]
57. Lou, R.; Ma, J.Z.; Xu, Q.N.; Fu, B.B.; Kong, L.Y.; Shi, Y.G.; Richard, P.; Weng, H.M.; Fang, Z.; Sun, S.S.; et al. Emergence of topological bands on the surface of ZrSnTe crystal. *Phys. Rev. B* **2016**, *93*, 241104(R). [[CrossRef](#)]
58. Hosen, M.M.; Dimitri, K.; Aperis, A.; Maldonado, P.; Belopolski, I.; Dhakal, G.; Kabir, F.; Sims, C.; Hasan, M.Z.; Kaczorowski, D.; et al. Observation of gapless Dirac surface states in ZrGeTe. *Phys. Rev. B* **2018**, *97*, 121103(R). [[CrossRef](#)]
59. Song, Y.K.; Wang, G.W.; Li, S.C.; Liu, W.L.; Lu, X.L.; Liu, Z.T.; Li, Z.J.; Wen, J.S.; Yin, Z.P.; Liu, Z.H.; et al. Photoemission Spectroscopic Evidence for the Dirac Nodal Line in the Monoclinic Semimetal SrAs₃. *Phys. Rev. Lett.* **2020**, *124*, 056402. [[CrossRef](#)]
60. Akiba, K.; Umeshita, N.; Kobayashi, T.C. Magnetotransport studies of the Sb square-net compound LaAgSb₂ under high pressure and rotating magnetic fields. *Phys. Rev. B* **2022**, *105*, 035108. [[CrossRef](#)]
61. Arakane, T.; Sato, T.; Souma, S.; Takahashi, T.; Watanabe, Y.; Inada, Y. Electronic structure of LaAgSb₂ and CeAgSb₂ studied by high-resolution angle-resolved photoemission spectroscopy. *J. Magn. Magn. Mater.* **2007**, *310*, 396. [[CrossRef](#)]
62. Chamorro, J.R.; Topp, A.; Fang, Y.; Winiarski, M.J.; Ast, C.R.; Krivenkov, M.; Varykhalov, A.; Ramshaw, B.J.; Schoop, L.M.; McQueen, T.M. Dirac fermions and possible weak antilocalization in LaCuSb₂. *APL Mater.* **2019**, *7*, 121108. [[CrossRef](#)]
63. Borisenko, S.; Evtushinsky, D.; Gibson, Q.; Yaresko, A.; Koepf, K.; Kim, T.; Ali, M.; van den Brink, J.; Hoesch, M.; Fedorov, A.; et al. Time-reversal symmetry breaking type-II Weyl state in YbMnBi₂. *Nat. Commun.* **2019**, *10*, 3424. [[CrossRef](#)]
64. Kealhofer, R.; Jang, S.; Griffin, S.M.; John, C.; Benavides, K.A.; Doyle, S.; Helm, T.; Moll, P.J.W.; Neaton, J.B.; Chan, J.Y.; et al. Observation of a two-dimensional Fermi surface and Dirac dispersion in YbMnSb₂. *Phys. Rev. B* **2018**, *97*, 045109. [[CrossRef](#)]
65. Feng, Y.; Wang, Z.; Chen, C.; Shi, Y.; Xie, Z.; Yi, H.; Liang, A.; He, S.; He, J.; Peng, Y.; et al. Strong Anisotropy of Dirac Cones in SrMnBi₂ and CaMnBi₂ Revealed by Angle-Resolved Photoemission Spectroscopy. *Sci. Rep.* **2014**, *4*, 5385. [[CrossRef](#)]
66. Marković, I.; Hooley, C.A.; Clark, O.J.; Mazzola, F.; Watson, M.D.; Riley, J.M.; Volckaert, K.; Underwood, K.; Dyer, M.S.; Murgatroyd, P.A.E.; et al. Weyl-like points from band inversions of spin-polarised surface states in NbGeSb. *Nat. Commun.* **2019**, *10*, 5485. [[CrossRef](#)]
67. Sun, Y.; Wu, S.C.; Yan, B. Topological surface states and Fermi arcs of the noncentrosymmetric Weyl semimetals TaAs, TaP, NbAs, and NbP. *Phys. Rev. B* **2015**, *92*, 115428. [[CrossRef](#)]
68. Momma, K.; Izumi, F. VESTA3 for three-dimensional visualization of crystal, volumetric and morphology data. *J. Appl. Crystallogr.* **2011**, *44*, 1272. [[CrossRef](#)]
69. Kokalj, A. XCRYSDEN—A new program for displaying crystalline structures and electron densities. *J. Mol. Graph. Model.* **1999**, *17*, 176. [[CrossRef](#)]
70. Marzari, N.; Mostofi, A.A.; Yates, J.R.; Souza, I.; Vanderbilt, D. Maximally localized Wannier functions: Theory and applications. *Rev. Mod. Phys.* **2012**, *84*, 1419. [[CrossRef](#)]
71. Marzari, N.; Vanderbilt, D. Maximally localized generalized Wannier functions for composite energy bands. *Phys. Rev. B* **1997**, *56*, 12847. [[CrossRef](#)]
72. Souza, I.; Marzari, N.; Vanderbilt, D. Maximally localized Wannier functions for entangled energy bands. *Phys. Rev. B* **2001**, *65*, 035109. [[CrossRef](#)]

73. Mostofi, A.A.; Yates, J.R.; Lee, Y.S.; Souza, I.; Vanderbilt, D.; Marzari, N. WANNIER90: A tool for obtaining maximally-localised Wannier functions. *Comput. Phys. Commun.* **2008**, *178*, 685. [[CrossRef](#)]
74. Mostofi, A.A.; Yates, J.R.; Pizzi, G.; Lee, Y.S.; Souza, I.; Vanderbilt, D.; Marzari, N. An updated version of WANNIER90: A tool for obtaining maximally-localised Wannier functions. *Comput. Phys. Commun.* **2014**, *185*, 2309. [[CrossRef](#)]
75. Pizzi, G.; Vitale, V.; Arita, R.; Blügel, S.; Freimuth, F.; Géranton, G.; Gibertini, M.; Gresch, D.; Johnson, C.; Koretsune, T.; et al. WANNIER90 as a community code: New features and applications. *J. Phys. Condens. Matter* **2020**, *32*, 165902. [[CrossRef](#)]

Supplemental Material:
Electronic band structure and surface states in Dirac semimetal LaAgSb₂

Marcin Rosmus,^{1,2} Natalia Olszowska,² Zbigniew Bukowski³, Paweł Starowicz¹, Przemysław Piekarczyk⁴, Andrzej Ptak⁴

¹Marian Smoluchowski Institute of Physics, Jagiellonian University, Prof. S. Łojasiewicza 11, PL-30348 Kraków, Poland

²Solaris National Synchrotron Radiation Centre, Jagiellonian University, Czerwone Maki 98, 30-392 Kraków, Poland

³Institute of Low Temperature and Structure Research, Polish Academy of Sciences, P.O. Box 1410, 50-950 Wrocław, Poland

⁴Institute of Nuclear Physics, Polish Academy of Sciences, ul. W. E. Radzikowskiego 152, PL-31342 Kraków, Poland

(Dated: September 13, 2022)

In this Supplemental Material we present additional band structures obtained from DFT calculations, in particular:

- Figure S1 – the bulk electronic band structure related to layers forming LaAgSb₂ structure.
- Figure S2 – the Dirac points at X and M.
- Figure S3 – nodal lines formed along X–R line.
- Figure S4 – Fermi surface branches shown separately.
- Figure S5 – comparison of the band structures in $P4/mmm$ (*not realized in reality*, SG:123) and $P4/nmm$ (SG:129) showing impact of the mirror symmetry and glide symmetry.
- Figure S6 – the bulk electronic band structure along Γ –M path for $k_z=0$ and $k_z=\pi/c$.

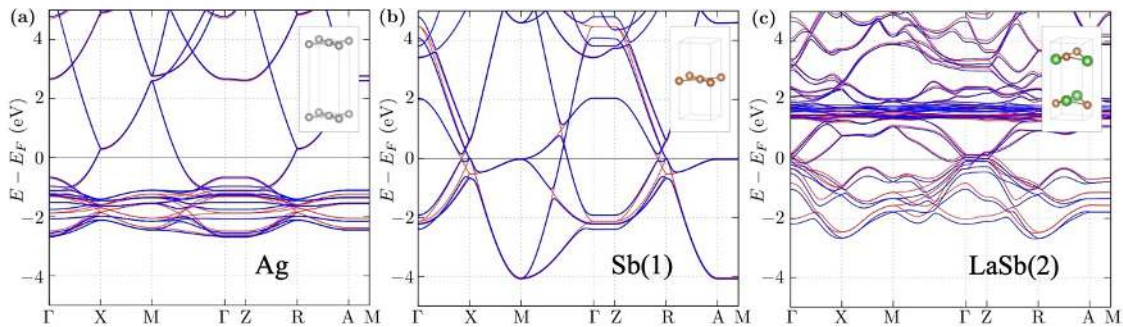


Figure S1. The bulk electronic band structure of layers forming bulk LaAgSb₂ structure (as labeled and shown in insets). Bands crossing the Fermi level in the case of Ag and Sb nets, correspond mostly to the p orbitals – which lead to the characteristic diamond-like Fermi surface with corner at X points. The Fermi surface centered at Γ is associated with bands of LaSb₂ double-layer showing nonsymmorphic glide symmetry.

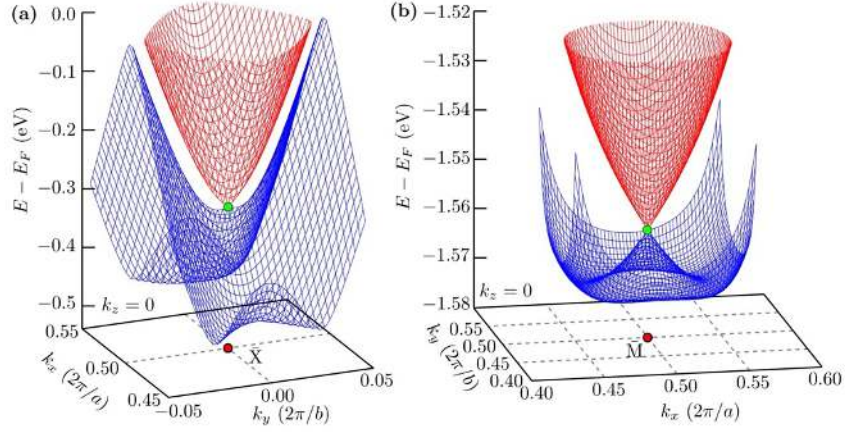


Figure S2. A realization of a Dirac point (green dot) at X (a) and M (b) points (zoom on insets at Fig. 2) forming a nodal line along X-A and M-R directions, respectively. In the case of the X point (a), the Dirac point is formed between the bottom vertex of the upper band (red) and the saddle point of the lower band (blue). In the case of M point (b), the Dirac point is realized between two bands a splitting of which is given by the spin-orbit coupling in the typical Rashba-like form.

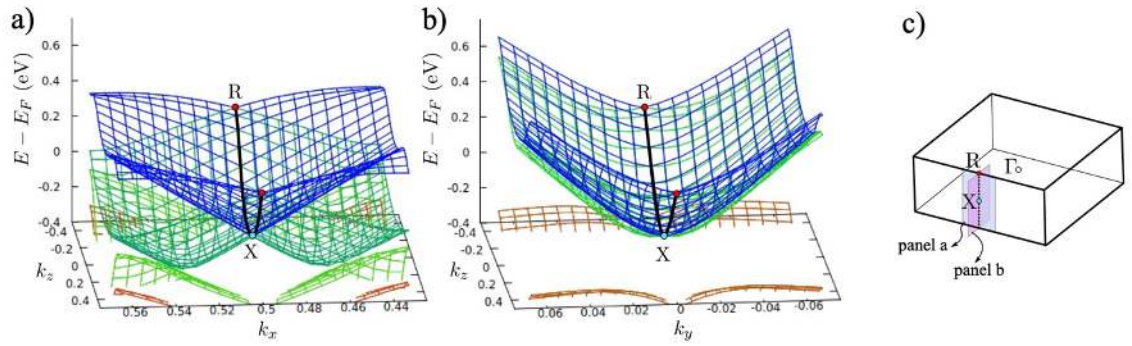


Figure S3. Band structures and Dirac nodal line along X-R direction. Panels (a) and (b) present dispersion relations in the vicinity of X-R direction along x and y axis, respectively [k -planes with respect to the Brillouin zone are presented in panel (c)]. Blue and red dots represent positions of X and R high symmetry points, respectively.

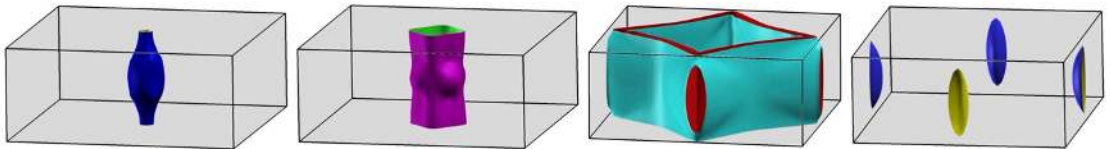


Figure S4. Branches of the Fermi surface of LaAgSb₂ shown in separate figures.

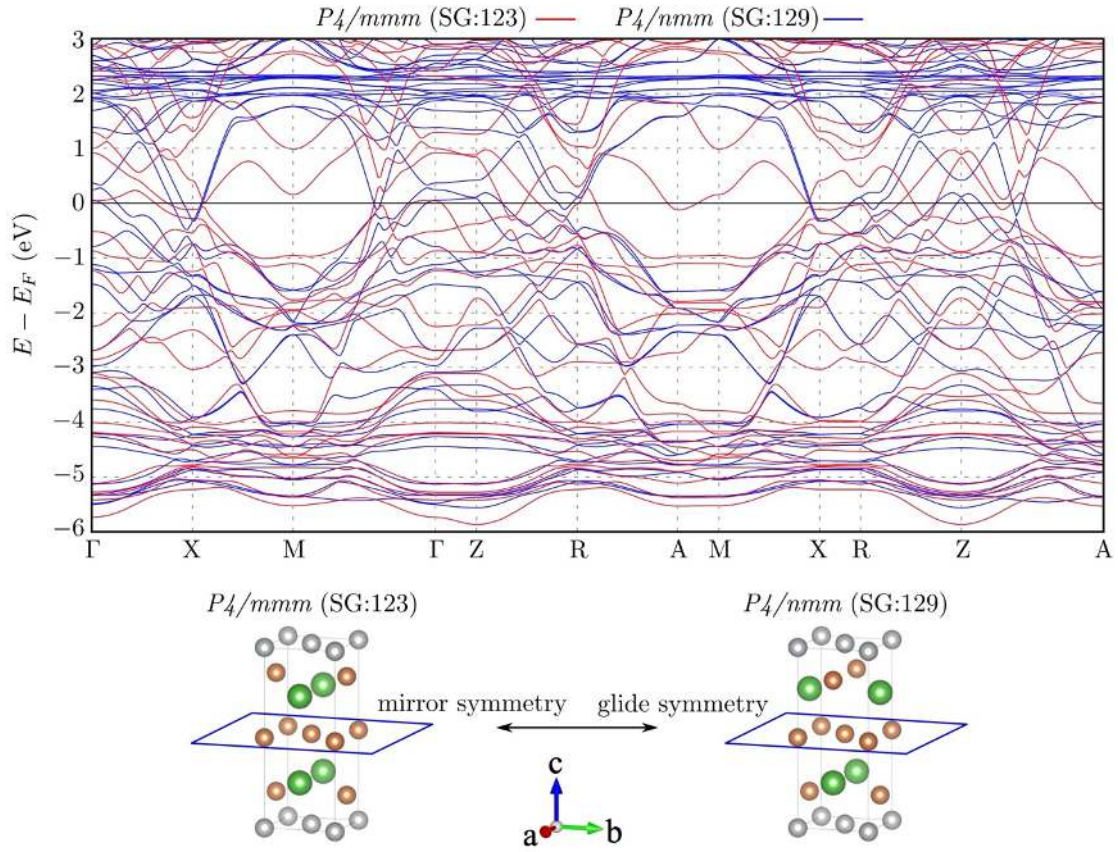


Figure S5. Comparison of the bulk electronic band structure of LaAgSb_2 for different structural variants, obtained from DFT calculations in the presence of the spin-orbit coupling. Red and blue lines correspond to structure with P_4/mmm and P_4/nmm space group, respectively. Replacement of the glide symmetry with the mirror symmetry (blue frame) causes a strong modification of the band structure of the system. In practice, this leads to a disappearance of the Dirac cones at high symmetry points X, M, R, or A, as well as a removal of degeneracy along A-M and X-R paths.

7. Dirac Dispersions and Fermi Surface Nesting in LaCuSb₂

M. Rosmus, N. Olszowska, Z. Bukowski, P. Piekarz, A. Ptok, P. Starowicz

I performed measurements of angle-resolved photoelectron spectroscopy (ARPES), together with N.O. I prepared the samples for measurements by orientation using the Laue diffraction method. I analyzed the experimental data and compared them with the theoretical results obtained by A.P. I developed the code for the data analysis. I prepared all the figures and the first draft of the manuscript. I participated in the discussion of the manuscript. The manuscript was corrected and discussed by M.R., P.S., P.P. and A.P. My contribution to the publication was 55%.

Dirac Dispersions and Fermi Surface Nesting in LaCuSb₂

Marcin Rosmus,^{1,2,*} Natalia Olszowska,² Zbigniew Bukowski,³
Przemysław Piekarz,⁴ Andrzej Ptok,⁴ and Paweł Starowicz^{1,†}

¹*Marian Smoluchowski Institute of Physics, Jagiellonian University, Prof. S. Łojasiewicza 11, PL-30348 Kraków, Poland*

²*Solaris National Synchrotron Radiation Centre, Jagiellonian University, Czerwone Maki 98, 30-392 Kraków, Poland*

³*Institute of Low Temperature and Structure Research, Polish Academy of Sciences, P.O. Box 1410, 50-950 Wrocław, Poland*

⁴*Institute of Nuclear Physics, Polish Academy of Sciences, W. E. Radzikowskiego 152, PL-31342 Kraków, Poland*

(Dated: June 4, 2023)

LaCuSb₂ is a superconductor with a transition temperature of about $T_c = 0.9$ K and is a potential platform where Dirac fermions can be experimentally observed. In this paper, we report systematic high-resolution studies of its electronic structure using the angle-resolved photoemission spectroscopy technique supported by the DFT calculation. We observe several linear dispersions forming Dirac-like structures and nodal lines. Finally, it appears that Fermi surface nesting properties are enhanced in LaCuSb₂ as compared to LaAgSb₂, while charge density waves appear in the latter system.

I. INTRODUCTION

A new chapter in solid-state physics was opened with the experimental discovery of topological insulators [1–3]. Expanding this idea led to the discovery of nodal line semimetals [4–6], Dirac [7–9] and Weyl semimetals [10–12], and other topologically non-trivial systems.

The dispersion relation in the case of Dirac semimetals is described by the relativistic Dirac equation and manifests itself in the form of linear bands forming characteristic cones [13, 14]. Such structures have been observed in Na₃Bi₈ and Cd₃As₂ [9]. A development of this idea is to extend the Dirac point in the second dimension so that it creates a nodal line [15]. Examples of systems in which nodal lines have been found are PtSnSb₄ [16], (Zr/Hf)SiS [17, 18], InBi [19], AlBSb₂ [20], and SrAsSb₃ [21]. Characteristic diamond-shaped Fermi surface is often observed in these materials [22–25].

The attention of researchers was attracted by the RT₂Sb₂ (R : rare earth, T : the d -electron transition metal) family of intermetallic compounds with an interplay between superconductivity [26, 27] and charge density wave (CDW) [28–30]. Furthermore, the theoretical calculations suggest the appearance of Dirac-like bands in these compounds [31, 32]. Several attempts have been made to study the electronic structure of these systems using the angle-resolved photoemission spectroscopy (ARPES) method. For LaAgSb₂, observation of Dirac-like structures and nesting of the Fermi surface has been reported [33], and more recently the nodal lines have been observed [34]. A particularly interesting compound of this type is LaCuSb₂, which exhibits superconducting properties below $T_c = 0.9$ K [35]. Moreover, LaCuSb₂ is considered as another system with Dirac fermions as measurements of Shubnikov-de Haas

quantum oscillations showed an electron effective mass of $0.065 m_e$ and transport measurements revealed linear magnetoresistance [36]. In agreement with these predictions the first ARPES studies indicated that linear dispersion is present for certain bands [36].

In this paper, we present a detailed and systematic study of band structure and Fermi surface of LaCuSb₂ performed with ARPES technique and DFT calculations. Dispersions of Dirac fermions are found in new regions, which have not been identified previously [36]. DFT calculations predicting the existence of nodal lines are in a good agreement with the experiment. The paper is organized as follows. Details of the techniques used are provided in Sec II. Next, in Sec. III we present and discuss our results. Finally, a summary is provided in Sect. IV.

II. METHODS AND TECHNIQUES

Single crystals of LaCuSb₂ were grown by the flux technique using Sb-rich antimony-copper melt as a flux. The excess of Cu was applied in order to prevent the formation of Cu-deficient LaCu_{1-x}Sb₂ phase. Lanthanum (purity 99.99%), copper (purity 99.99%) and antimony (purity 99.999%) were used as starting materials. The components were weighed in the atomic ratio La:Cu:Sb=1:1.5:13 and placed in an alumina crucible, which was then sealed in an evacuated silica tube. The ampoule was heated at 1100°C for 5 h followed by slow cooling (2–3°C/h) down to 700°C. At this temperature, the ampoule was flipped upside down in order to decant liquid Sb-Cu flux. Next, the ampoule was cooled to room temperature and the crucible was transferred to another silica tube, where the rest of Sb was removed from crystals by means of sublimation in a high dynamic vacuum at 600°C. Finally, single crystals were mechanically separated.

The obtained crystals were examined using a scanning electron microscope (SEM) Philips 515 and their chemical composition was determined with an energy disper-

* e-mail: marcin.rosmus@uj.edu.pl

† e-mail: pawel.starowicz@uj.edu.pl

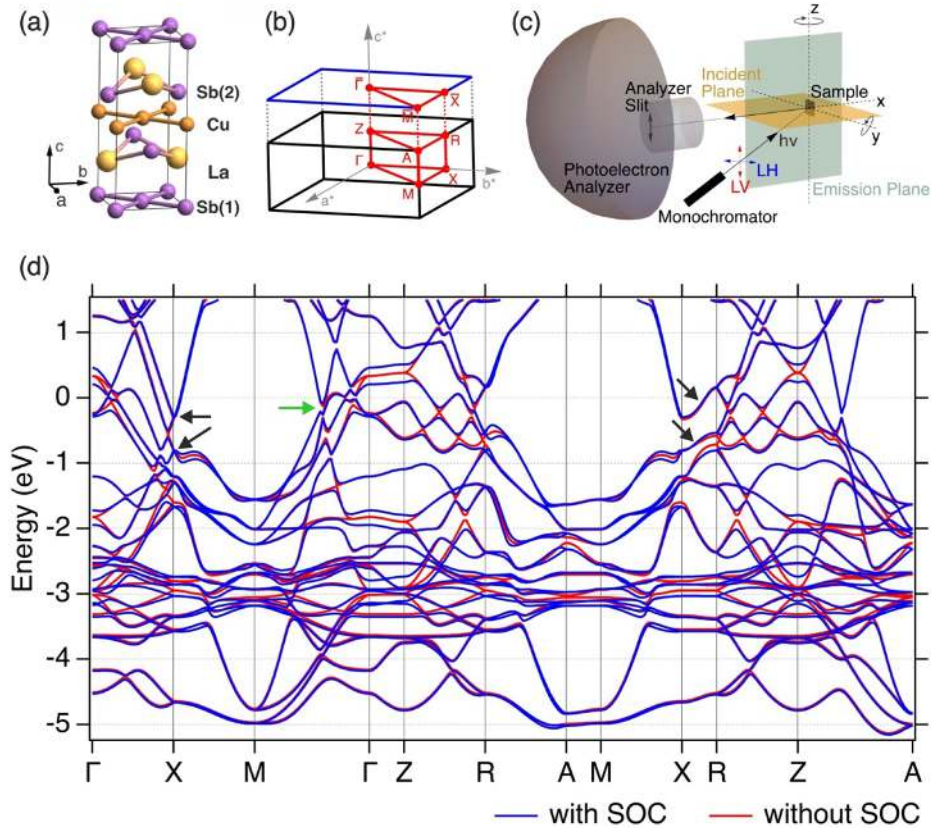


FIG. 1. The tetragonal crystal structure of LaCuSb₂ (a) and the corresponding first Brillouin zone with their high-symmetry points (b). The geometry of the ARPES measurement system (c). The bulk band structure (d) in the absence and presence of the spin-orbit coupling (blue and red lines, respectively). Black arrows indicate the position of the nodal line, while green arrow marks the location of the gapped structure.

sive X-ray (EDX) spectrometer PV9800. The phase purity and lattice parameters were determined from powder X-ray diffraction data obtained on pulverized single crystals.

High-resolution angle-resolved photoemission studies were performed at the URANOS beamline of Solaris Synchrotron [37], Kraków, Poland. The beamline is equipped with a Scienta-Omicron DA30-L electron analyzer. The geometry of the experimental setup is shown in Figure 1(c). The samples were cleaved in situ under ultra-high vacuum at room temperature. The pressure during the ARPES measurement was below 5×10^{-11} mbar and the temperature during the experiment was 14 K.

The electronic structure was calculated using density functional theory (DFT) within the projector augmented-wave (PAW) method [38] with the Vienna Ab initio Simulation Package (VASP) [38–40]. The exchange correlation potential was obtained by the gen-

eralized gradient approximation (GGA) in the Perdew–Burke–Erzerhof form [41]. Calculations were made using a $20 \times 20 \times 10$ Monkhorst–Pack \mathbf{k} -point mesh [42]. The kinetic energy cut-off for the plane-wave expansion was equal to 520 eV. The energy convergence criteria used to relax the structures, with the conjugate gradient technique, were set at 10^{-8} eV and 10^{-6} eV for the electronic and ionic iterations, respectively.

The optimized structure was used to construct the tight-binding model in the maximally localized Wannier orbitals. In the discuss case, we starting calculation from initial p -orbitals of Sb and d -orbitals of La and Cu, what correspond to 32-orbitals tight binding model. In order to study the surface states, the surface Green function for a semi-infinite system [43] was calculated using WANNIERTOOLS [44].

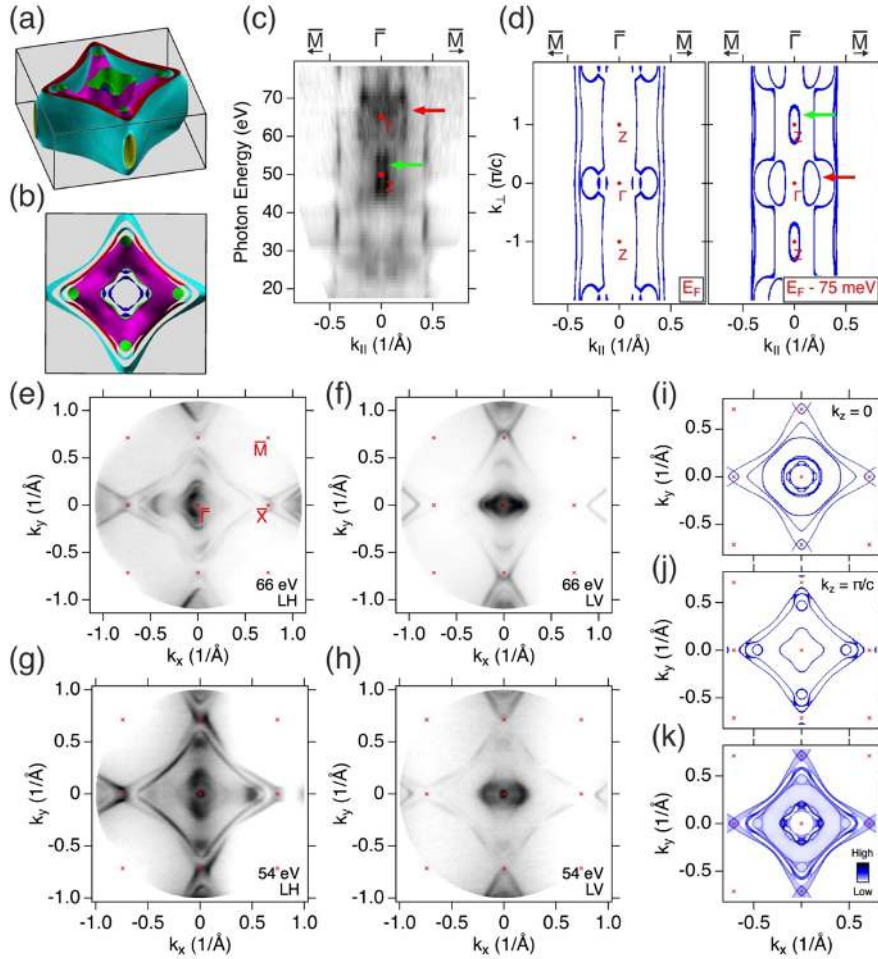


FIG. 2. Fermi surface of LaCuSb₂. Three-dimensional view of the Fermi surface calculated without SOC (a), and its top view (b). Photon energy dependence map (c) along the $\bar{M}-\bar{\Gamma}-\bar{M}$ direction for the binding energy corresponding to the Fermi level. Calculated constant energy map (d) along $\bar{M}-\bar{\Gamma}-\bar{M}$ direction. Panels (e)-(h) present the Fermi surface obtained by ARPES for different photon energies and polarisations (LH – linear horizontal, LV – linear vertical). Cross-section of the Fermi surface for $k_z = 0$ (i) and $k_z = \pi/c$ (j), while (k) present projection of the bulk Fermi surface onto two-dimensional surface BZ. Red and green arrows in (c) and (d) indicate characteristic features of the experimental and theoretical spectrum.

III. RESULTS AND DISCUSSION

LaCuSb₂ crystallizes in the tetragonal, layered structure (P4/nmm, space group No. 129), consisting of Sb(2)-La layers related by glide symmetry and two-dimensional planes formed by either Cu or Sb(1) atoms. Crystal structure of LaCuSb₂ is shown in Fig. 1(a). The lattice constants are equal to $a = 4.3828(2)$ Å and $c = 10.2097(7)$ Å [45]. The tetragonal Brillouin zone corresponding to the lattice is shown in Fig. 1(b).

Bulk calculation of the band structure, shown in Fig. 1(d), with and without spin-orbit coupling (SOC) indicates that the electronic structure consists of several bands with linear dispersion along the $\Gamma-X$ and $\Gamma-M$ path. The existence of these bands may be associated with Dirac fermions. Moreover, several places can be distinguished where band crossing exists (e.g. in the proximity of the X point). As a consequence of the symmetry of the system, the nodal lines are realized in the X-R and M-A directions. At the X and R points, the band structure without SOC shows Dirac nodes that are part

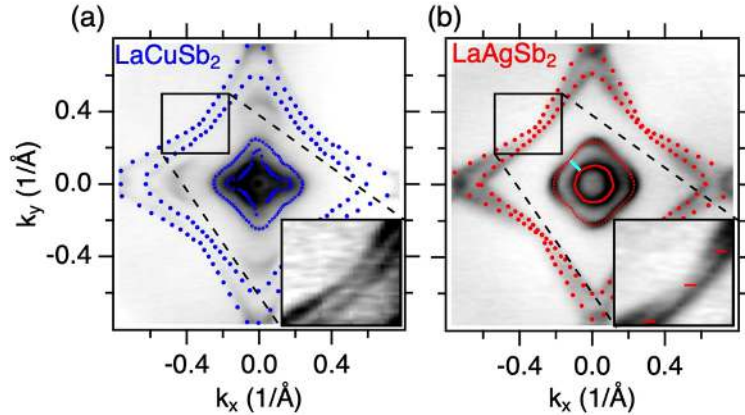


FIG. 3. Comparison of Fermi surface nesting in (a) LaCuSb_2 and (b) LaAgSb_2 . The red lines in (b) correspond to the length of the CDW vector $q_1 = 0.026 \cdot (2\pi/a)$, and the cyan line shows the possible nesting vector.

of the nodal line that crosses the Fermi energy [marked with black arrows in Fig. 1(d)]. The nodal line is present after considering the spin-orbit interaction, no gap is observed in the structure in X-R direction. The case is different in the direction of Γ -M, in which band crossing is eliminated under the influence of SOC and a gapped structure is present [green arrow in Fig. 1(d)].

According to the calculations, Fermi Surface is composed of four bands, two of them forming the characteristic large diamond-like shape spanned approximately between X points, while the other two are strongly three-dimensional and centered at the Γ point [Fig. 2(a) and (b)]. To fully understand the electronic structure of LaCuSb_2 , we performed the photon energy dependence measurement to find the photon energy corresponding to the high-symmetry points. At the collected Fermi surface, we can distinguish four bands, two of which have clear quasi-two-dimensional characters ($k_{\parallel} \sim \pm 0.4 \text{ \AA}^{-1}$), and the other two create characteristic shapes, marked with the red and green arrow in Fig. 2(c). To compare ARPES results with the theoretical calculations we analyzed several constant energy maps from the vicinity of E_F . The map corresponding to the binding energy of 75 meV revealed similar-looking structures, which allowed us to identify the location of the points of high symmetry. The difference of the 75 meV between the measured and calculated map may be the effect of the energy resolution of the k_z scan and the shifts of the simulated bands relative to the real ones. The calculations corresponding to E_F and $E_F - 75 \text{ meV}$ are shown in Fig. 2(d), the green and red arrows correspond to analogous structures in the experimental map. The position of the Γ point corresponds to photon energy about 66 eV, and the Z point to about 50 eV. The experimental in-plane Fermi surfaces are shown in Fig. 2(e)-(h). Measurements were performed using photon energies of 66 and 54 eV

with either linear vertical (LV) or linear horizontal (LH) polarization; details are specified in the figures. The intensity of the four pockets that form the Fermi surface strongly depends on the polarization of the light. The outer pocket consists of two arc-shaped lines connecting the X points. The separation between them is clearly visible in each of the measurements. The inner pockets form an intricate structure centered around the Γ point. Comparison with the theoretical calculations corresponding to the planes including the points of high symmetry shows similarity for $k_z = 0$ and a large discrepancy for $k_z = \pi/c$ [Fig. 2(i) and (j)]. However, theoretical Fermi surface map integrated over all k_z [Fig. 2(k)] shows much greater similarity to the experimental measurements, indicating a strong mixing of k_z what has already been reported for similar compounds [17, 34].

A nesting of the Fermi surface can play a role in the formation of CDW or superconducting ground state. Thus, it is instructive to study the nesting in superconducting LaCuSb_2 and compare it with the relative system LaAgSb_2 , which exhibits CDW. A detailed description of the electronic structure of LaAgSb_2 was published by Rosmus *et al.* in Ref. [34]. The main idea behind the study of nesting in the compound with Ag was related to the scenario of the Peierls transition. According to this concept, one should observe the nesting in a compound exhibiting CDW and its decay would be expected as superconductivity appears in the phase diagram. Nesting itself has already been reported for LaAgSb_2 by Shi *et al.* in Ref. [33]. They suggested that the translation takes place between the bands forming the diamond-like pockets connecting X points on the Fermi surface, and the nesting vector is consistent with the CDW vector. A comparison of the Fermi surfaces of LaCuSb_2 and LaAgSb_2 is shown in Fig. 3. These results were collected at 66 eV (our proposed Γ point) and obtained by adding LV and

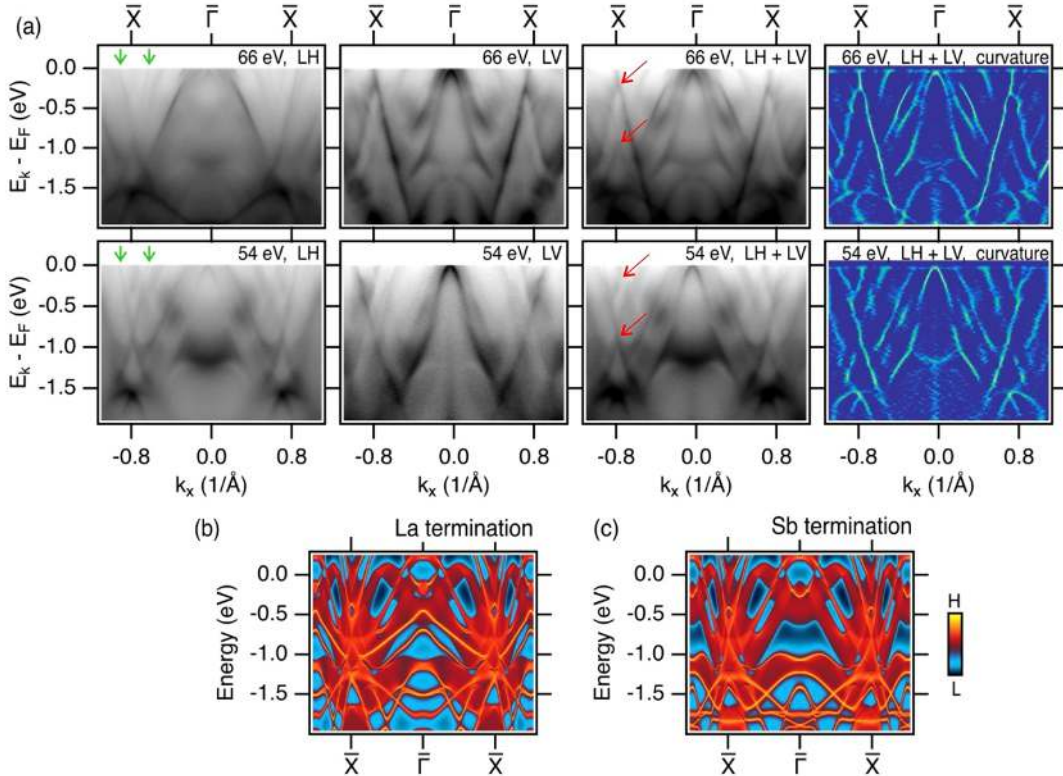


FIG. 4. Electronic structure along the $\bar{X}-\bar{\Gamma}-\bar{X}$ direction. (a) ARPES spectra collected with use of the 66 and 54 eV, LH and LV light polarizations. The curvature [46] was calculated for the sum of both polarizations. Calculated surface spectrum for La (b) and Sb (c) surface terminations, obtained from surface Green function technique. In panel (a), green arrows show positions of the linear bands, while red arrows indicate Dirac-like crosses of the bands.

LH polarization data in order to get more symmetrical maps. The insets are focused on the region in which nesting may appear. Our high-resolution ARPES measurements indicate that this nesting is not perfect, and the shape of the considered pocket cannot be reproduced by a translation alone. In fact, only single points of the Fermi surface can be connected by the nesting vector, $q_1 \sim 0.026 \cdot (2\pi/a)$ related to CDW modulation [red lines in Fig. 3(b)]. Moreover, we made attempts to measure the energy gap for LaAgSb₂ associated with the CDW. It was not observed in any of the bands (not shown) by ARPES measurements carried out at $T = 18$ K with energy resolution of 10 meV. In the case of internal pockets centered around the $\bar{\Gamma}$ point, nesting features can be found on their flattened edges $q \sim 0.068 \cdot (2\pi/a)$ [marked with cyan line in Fig. 3(b)]. The shape of the smallest pocket is significantly different in the case of the compound with Cu, where a removal of nesting is observed. However, the nesting vector found in the experiment would be about three times larger than that resulting from CDW mod-

ulation measurements q_1 , which is inconsistent with the Peierls scenario. Surprisingly, nesting at diamond-like pockets appears to be more perfect in the case of superconducting LaCuSb₂. In the case of this compound, we can speak of the similarity of diamond-like pockets sufficient to reconstruct them by shifting the appropriate Fermi surface fragments. That is a surprising result that contradicts simple expectations and shows that a simple Peierls transition approach is not sufficient to explain the nature of CDW in LaAgSb₂.

In Figure 4 we present the dispersions of LaCuSb₂ along the $\bar{X}-\bar{\Gamma}-\bar{X}$ direction. Linear bands that cross at \bar{X} point are clearly visible. With our very high-quality data, we can clearly and convincingly observe the low-intensity linear bands previously reported for ARPES by Chamorro *et al.* in Ref. [36] in this compound (green arrows in Figure 4a). Moreover, our data reveal previously unseen details of the band structure, in particular the characteristic crossing of the linear bands forming an X shape. The intersection points of these linear

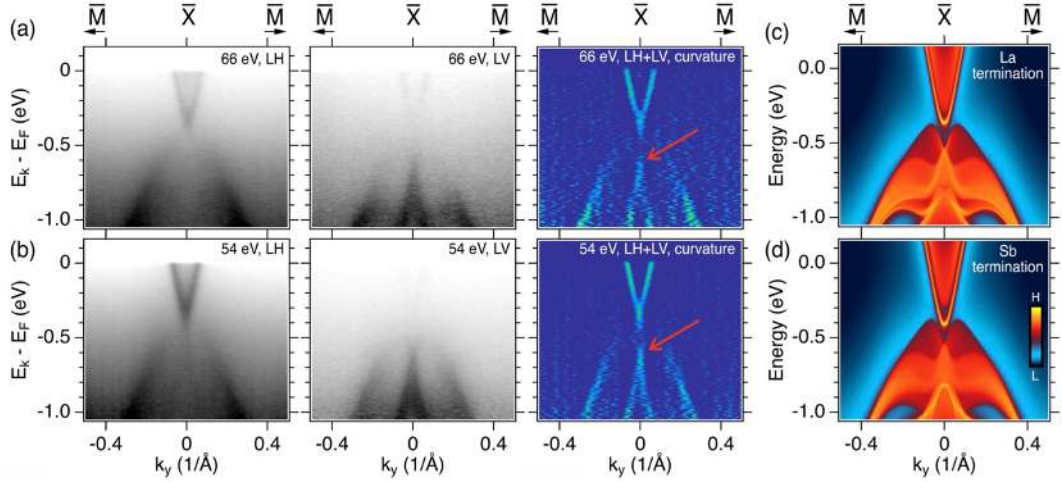


FIG. 5. The band structure along the $\bar{M}-\bar{X}-\bar{M}$ direction. (a) Measurements were made with a photon energy of 66 eV, horizontal and vertical polarization, respectively, and curvature was calculated for the sum of both polarizations. (b) Analogous to (a) for the energy of 54 eV. Red arrows indicated localization of Dirac points. Surface Green function for (c) La and (d) Sb terminations along the $\bar{M}-\bar{X}-\bar{M}$ direction. Surface Green function for (e) La and (f) Sb termination along $\bar{\Gamma}-\bar{X}-\bar{M}$ direction.

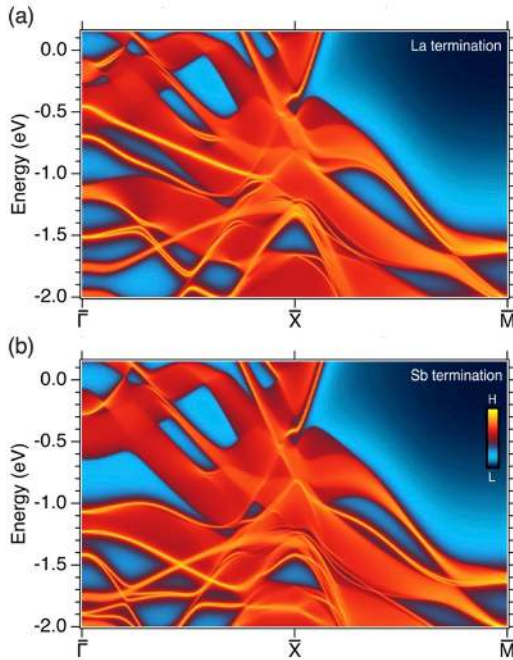


FIG. 6. Calculated surface spectrum for (a) La and (b) Sb terminations.

bands are observed for binding energies of about 0.1 eV and about 1 eV, they were marked with red arrows in Fig. 4(a). These linear bands indicate the presence of Dirac fermions in the studied system, which is consistent with linear magnetoresistance and very low effective mass obtained in Shubnikov-de Haas experiment [31, 36]. Moreover, comparing the location of these points of intersection with bulk calculations [Fig. 1(d)], it can be presumed that they are part of the nodal line forming in the X-R direction. The question of the existence of these nodal lines is continued in the description of the structure measured in the direction $\bar{M}-\bar{X}-\bar{M}$. The observed electronic structure is very well reproduced by surface green function calculations [Fig. 4(b) and (c)], except for the hole pocket appearing in calculations around the $\bar{\Gamma}$ point. It is not visible in the experiment for the used photon energy and polarizations. The calculations were performed for two surface terminations [see Fig. 4(b) for La termination, and Fig. 4(c) for Sb termination). Based on a few details (e.g. “wavy” band at -1 eV energy at $\bar{\Gamma}$ and parabolic band visible at 66 eV with maxima at about -1.5 eV) it can be concluded that the measured spectra correspond to Sb termination.

The dispersion along the $\bar{M}-\bar{X}-\bar{M}$ direction is shown in Figure 5. The ARPES results revealed a structure consisting of an electron pocket and linear bands. The visible dispersion agrees well with the theoretical result shown in Fig. 5(c) and 5(d). Calculations suggest the existence of an energy gap between the bands and the band crossing forming the nodal line in the X-R direction. In fact, there is a lack of intensity in the measured spectra

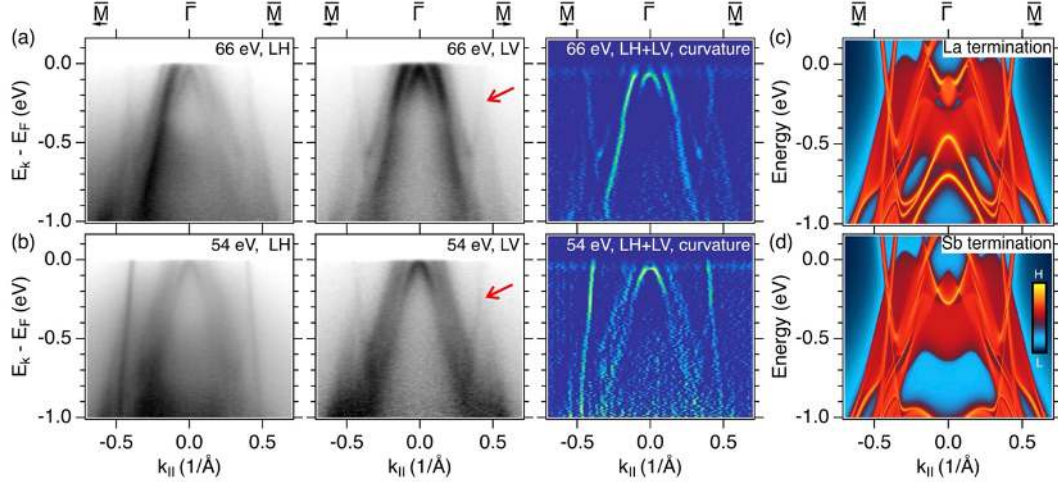


FIG. 7. The electronic structure along the $\bar{M}-\bar{\Gamma}-\bar{M}$ direction. Measurements were made with a photon energy of 66 eV, horizontal and vertical polarization, respectively, and curvature was calculated for the sum of both polarizations. (b) Analogous to (a) for energy of 54 eV. The red arrows show the location of the crosses of linear bands.

that matches the predicted gap, and it occurs at a binding energy of about 0.5 eV. However, the quality of the data does not allow us to decide whether this is actually an energy gap or an effect of matrix elements. On the other hand, the linear crossing bands forming the Dirac point and consequently the nodal line are visible. The location of the Dirac points is indicated by red arrows in the curvatures in Fig. 5. The visibility of these bands strongly depends on the light polarization; the electron pocket crossing F is clearly visible in LH, while the linear part of the structure is visible in LV. The bands measured at 66 eV and 54 eV are very similar, which proves their two-dimensional nature. To better understand the shape of the bands and the compatibility between the spectra collected along the $\bar{X}-\bar{\Gamma}-\bar{X}$ and $\bar{M}-\bar{X}-\bar{M}$ directions in Figure 6 we presented the calculations along the $\bar{\Gamma}-\bar{X}-\bar{M}$ path. The lack of intensity around 0.5 eV at \bar{X} point fits the spectra collected in both directions, while the bands form the electron pocket, which is clearly visible in the $\bar{M}-\bar{X}-\bar{M}$ direction, do not show an analogous dispersion in the $\bar{X}-\bar{\Gamma}-\bar{X}$ direction. In Figure 4a, this pocket corresponds to the increase in intensity observed at \bar{X} point in the energy range -0.4 to 0 eV. The situation is analogous to the nodal line, the bands forming it in the $\bar{X}-\bar{\Gamma}-\bar{X}$ direction have a much smaller slope, which is why their crossing is better visible in the $\bar{M}-\bar{X}-\bar{M}$ direction.

In the direction of $\bar{M}-\bar{\Gamma}-\bar{M}$, almost linear bands are visible crossing the Fermi level [Fig. 7(a) and (b)]. These bands cross and create a characteristic Dirac-like shape. Band-crossing is observed at about 0.2 eV below the E_F [marked with red arrows in Fig. 7(a) and (b)]. An analogous shape is visible in the surface Green function

[Fig. 7(c) and (d)]. ARPES measurements indicate the gapless nature of this feature. According to the bulk calculation [Fig. 1(d)], the gap should be present, however in the surface Green function no gap is visible. As the surface function is an integration along the k_z direction, it may mean that the hypothetical energy gap changes its location in the energy scale for different k_z values. ARPES spectra for low excitation energies are sensitive to the surface and have a relatively low resolution in k_z , therefore they are better modeled by the surface Green function, which explains the lack of the energy gap.

IV. SUMMARY

In conclusion, we performed a detailed ARPES study supported by the theoretical calculation of LaCuSb₂ superconductor. Our results showed the existence of crossing linear bands near the \bar{X} point and along the $\bar{M}-\bar{\Gamma}-\bar{M}$ direction. There are potentially related to the occurrence of Dirac fermions in this compound. We observed several places where linear bands intersect and form nodal lines in the $X-R$ and $\Gamma-Z$ directions. A comparison of the Fermi surface nesting of LaCuSb₂ and LaAgSb₂ compounds showed stronger nesting in LaCuSb₂. The experimentally observed nesting vectors for LaAgSb₂ do not explain the CDW in that material because they are not consistent with the CDW modulation vector.

ACKNOWLEDGMENTS

A. P. is grateful to Laboratoire de Physique des Solides (CNRS - Université Paris-Saclay) for hospitality during a part of the work on this project. P.P. and A.P. acknowledge the support by National Science Centre (NCN, Poland) under Project No. 2021/43/B/ST3/02166.

-
- [1] M. Z. Hasan and C. L. Kane, Colloquium: Topological insulators, *Rev. Mod. Phys.* **82**, 3045 (2010).
- [2] F. D. M. Haldane, Nobel lecture: Topological quantum matter, *Rev. Mod. Phys.* **89**, 040502 (2017).
- [3] V. Bhardwaj and R. Chatterjee, Topological Materials: New Quantum Phases of Matter, *Resonance* **25**, 431 (2020).
- [4] C. Fang, H. Weng, X. Dai, and Z. Fang, Topological nodal line semimetals, *Chinese Phys. B* **25**, 117106 (2016).
- [5] I. Lee, S. I. Hyun, and J. H. Shim, Topological classification of nodal-line semimetals in square-net materials, *Phys. Rev. B* **103**, 165106 (2021).
- [6] C. Fang, Y. Chen, H.-Y. Kee, and L. Fu, Topological nodal line semimetals with and without spin-orbital coupling, *Phys. Rev. B* **92**, 081201 (2015).
- [7] N. P. Armitage, E. J. Mele, and A. Vishwanath, Weyl and Dirac semimetals in three-dimensional solids, *Rev. Mod. Phys.* **90**, 015001 (2018).
- [8] Z. K. Liu, B. Zhou, Y. Zhang, Z. J. Wang, H. M. Weng, D. Prabhakaran, S.-K. Mo, Z. X. Shen, Z. Fang, X. Dai, Z. Hussain, and Y. L. Chen, Discovery of a three-dimensional topological Dirac semimetal, *Na₃Bi*, *Science* **343**, 864 (2014).
- [9] Z. K. Liu, J. Jiang, B. Zhou, Z. J. Wang, Y. Zhang, H. M. Weng, D. Prabhakaran, S.-K. Mo, H. Peng, P. Dudin, T. Kim, M. Hoesch, Z. Fang, X. Dai, Z. X. Shen, D. L. Feng, Z. Hussain, and Y. L. Chen, A stable three-dimensional topological Dirac semimetal *Cd₃As₂*, *Nature Mater.* **13**, 677 (2014).
- [10] B. Q. Lv, H. M. Weng, B. B. Fu, X. P. Wang, H. Miao, J. Ma, P. Richard, X. C. Huang, L. X. Zhao, G. F. Chen, Z. Fang, X. Dai, T. Qian, and H. Ding, Experimental discovery of Weyl semimetal *TaAs*, *Phys. Rev. X* **5**, 031013 (2015).
- [11] H. Weng, C. Fang, Z. Fang, B. A. Bernevig, and X. Dai, Weyl semimetal phase in noncentrosymmetric transition-metal monophosphides, *Phys. Rev. X* **5**, 011029 (2015).
- [12] S.-Y. Xu, I. Belopolski, N. Alidoust, M. Neupane, G. Bian, C. Zhang, R. Sankar, G. Chang, Z. Yuan, C.-C. Lee, S.-M. Huang, H. Zheng, J. Ma, D. S. Sanchez, B. Wang, A. Bansil, F. Chou, P. P. Shibayev, H. Lin, S. Jia, and M. Z. Hasan, Discovery of a Weyl fermion semimetal and topological Fermi arcs, *Science* **349**, 613 (2015).
- [13] A. A. Burkov, Topological semimetals, *Nature Mater.* **15**, 1145 (2016).
- [14] A. A. Burkov, M. D. Hook, and L. Balents, Topological nodal semimetals, *Phys. Rev. B* **84**, 235126 (2011).
- [15] S.-Y. Yang, H. Yang, E. Derunova, S. S. P. Parkin, B. Yan, and M. N. Ali, Symmetry demanded topological nodal-line materials, *Advances in Physics: X* **3**, 1414631 (2018).
- [16] Y. Wu, L.-L. Wang, E. Mun, D. D. Johnson, D. Mou, L. Huang, Y. Lee, S. L. Bud'ko, P. C. Canfield, and A. Kaminski, Dirac node arcs in *PtSn₄*, *Nat. Phys.* **12**, 667 (2016).
- [17] B.-B. Fu, C.-J. Yi, T.-T. Zhang, M. Caputo, J.-Z. Ma, X. Gao, B. Q. Lv, L.-Y. Kong, Y.-B. Huang, P. Richard, M. Shi, V. N. Strocov, C. Fang, H.-M. Weng, Y.-G. Shi, T. Qian, and H. Ding, Dirac nodal surfaces and nodal lines in *ZrSiS*, *Sci. Adv.* **5**, eaa6459 (2019).
- [18] C. Chen, X. Xu, J. Jiang, S.-C. Wu, Y. P. Qi, L. X. Yang, M. X. Wang, Y. Sun, N. B. M. Schröter, H. F. Yang, L. M. Schoop, Y. Y. Lv, J. Zhou, Y. B. Chen, S. H. Yao, M. H. Lu, Y. F. Chen, C. Felser, B. H. Yan, Z. K. Liu, and Y. L. Chen, Dirac line nodes and effect of spin-orbit coupling in the nonsymmorphic critical semimetals *MSiS* ($M = \text{Hf, Zr}$), *Phys. Rev. B* **95**, 125126 (2017).
- [19] S. A. Ekahana, S.-C. Wu, J. Jiang, K. Okawa, D. Prabhakaran, C.-C. Hwang, S.-K. Mo, T. Sasagawa, C. Felser, B. Yan, Z. Liu, and Y. Chen, Observation of nodal line in non-symmorphic topological semimetal *InBi*, *New J. Phys.* **19**, 065007 (2017).
- [20] D. Takane, S. Souma, K. Nakayama, T. Nakamura, H. Oinuma, K. Hori, K. Horiba, H. Kumigashira, N. Kimura, T. Takahashi, and T. Sato, Observation of a dirac nodal line in *AlB₂*, *Phys. Rev. B* **98**, 041105 (2018).
- [21] Y. K. Song, G. W. Wang, S. C. Li, W. L. Liu, X. L. Lu, Z. T. Liu, Z. J. Li, J. S. Wen, Z. P. Yin, Z. H. Liu, and D. W. Shen, Photoemission spectroscopic evidence for the dirac nodal line in the monoclinic semimetal *SrAs₃*, *Phys. Rev. Lett.* **124**, 056402 (2020).
- [22] Y. Yen, C.-L. Chiu, P.-H. Lin, R. Sankar, T.-M. Chuang, and G.-Y. Guo, Dirac nodal line and Rashba spin-split surface states in nonsymmorphic *ZrGeTe*, *New J. Phys.* **23**, 103019 (2021).
- [23] T. Nakamura, S. Souma, Z. Wang, K. Yamauchi, D. Takane, H. Oinuma, K. Nakayama, K. Horiba, H. Kumigashira, T. Oguchi, T. Takahashi, Y. Ando, and T. Sato, Evidence for bulk nodal loops and universality of Dirac-node arc surface states in *ZrGeX_c* ($X_c = \text{S, Se, Te}$), *Phys. Rev. B* **99**, 245105 (2019).
- [24] M. Neupane, I. Belopolski, M. M. Hosen, D. S. Sanchez, R. Sankar, M. Szlawska, S.-Y. Xu, K. Dimitri, N. Dhakal, P. Maldonado, P. M. Oppeneer, D. Kaczorowski, F. Chou, M. Z. Hasan, and T. Durakiewicz, Observation of topological nodal fermion semimetal phase in *ZrSiS*, *Phys. Rev. B* **93**, 201104 (2016).
- [25] S. Regmi, R. Smith, A. P. Sakhya, M. Sprague, M. I. Mondal, I. B. Elius, N. Valadez, A. Ptok, D. Kaczorowski, and M. Neupane, Observation of gapless nodal-line states in *NdSbTe*, *Phys. Rev. Mater.* **7**, 044202 (2023).

- [26] K. Vijaya Lakshmi, L. Menon, A. Nigam, A. Das, and S. Malik, Magneto-resistance studies on $RTSb_2$ compounds ($R = La, Ce$ and $T = Ni, Cu$), *Phys. B* **223-224**, 289 (1996).
- [27] F. Han, C. D. Malliakas, C. C. Stoumpos, M. Sturza, H. Claus, D. Y. Chung, and M. G. Kanatzidis, Superconductivity and strong intrinsic defects in $LaPd_{1-x}Bi_2$, *Phys. Rev. B* **88**, 144511 (2013).
- [28] C. Song, J. Park, J. Koo, K.-B. Lee, J. Y. Rhee, S. L. Bud'ko, P. C. Canfield, B. N. Harmon, and A. I. Goldman, Charge-density-wave orderings in $LaAgSb_2$: An x-ray scattering study, *Phys. Rev. B* **68**, 035113 (2003).
- [29] R. Singha, S. Samanta, T. S. Bhattacharya, S. Chatterjee, S. Roy, L. Wang, A. Singha, and P. Mandal, Lattice dynamics of the topological dirac semimetal $LaAgSb_2$ with charge density wave ordering, *Phys. Rev. B* **102**, 205103 (2020).
- [30] A. Bosak, S.-M. Souliou, C. Faugeras, R. Heid, M. R. Molas, R.-Y. Chen, N.-L. Wang, M. Potemski, and M. Le Tacon, Evidence for nesting-driven charge density wave instabilities in the quasi-two-dimensional material $LaAgSb_2$, *Phys. Rev. Res.* **3**, 033020 (2021).
- [31] P. Ruszała, M. J. Winiarski, and M. Samsel-Czekala, Dirac-like band structure of $LaTESb_2$ ($TE = Ni, Cu$, and Pd) superconductors by DFT calculations, *Comput. Mater. Sci.* **154**, 106 (2018).
- [32] I. Hase and T. Yanagisawa, Electronic band calculation of $LaTSb_2$ ($T = Cu, Ag, Au$), *Physics Procedia* **58**, 42 (2014).
- [33] X. Shi, P. Richard, K. Wang, M. Liu, C. E. Matt, N. Xu, R. S. Dhaka, Z. Ristic, T. Qian, Y.-F. Yang, C. Petrovic, M. Shi, and H. Ding, Observation of dirac-like band dispersion in $LaAgSb_2$, *Phys. Rev. B* **93**, 081105 (2016).
- [34] M. Rosmus, N. Olszowska, Z. Bukowski, P. Starowicz, P. Piekarczyk, and A. Ptok, Electronic band structure and surface states in Dirac semimetal $LaAgSb_2$, *Materials* **15**, 7168 (2022).
- [35] Y. Muro, N. Takeda, and M. Ishikawa, Magnetic and transport properties of dense Kondo systems, $CeTSb_2$ ($T = Ni, Cu, Pd$ and Ag), *J. Alloys Compd.* **257**, 23 (1997).
- [36] J. R. Chamorro, A. Topp, Y. Fang, M. J. Winiarski, C. R. Ast, M. Krivenkov, A. Varykhalov, B. J. Ramshaw, L. M. Schoop, and T. M. McQueen, Dirac fermions and possible weak antilocalization in $LaCuSb_2$, *Appl. Phys. Rev.* **7**, 121108 (2019).
- [37] J. Szlachetko, J. Szade, E. Beyer, W. Błachucki, P. Ciochoń, P. Dumas, K. Freindl, G. Gazdowicz, S. Glatt, K. Guła, J. Hormes, P. Indyka, A. Klonecka, J. Kołodziej, T. Kołodziej, J. Korecki, P. Korecki, F. Kosiorowski, K. Kosowska, G. Kowalski, M. Kozak, P. Koziół, W. Kwiatek, D. Liberda, H. Lichtenberg, E. Madej, A. Mandziak, A. Marendziak, K. Matlak, A. Maximenko, P. Nita, N. Olszowska, R. Panaś, E. Partyka-Jankowska, M. Piszak, A. Prange, M. Rawski, M. Roman, M. Rosmus, M. Sikora, J. Sławek, T. Sobol, K. Sowa, N. Spiridis, J. Stepień, M. Szczepanik, T. Ślęzak, T. Tyliśczyk, G. Ważny, J. Wiechecki, D. Wilgocka-Ślęzak, B. Wolanin, P. Wróbel, T. Wróbel, M. Zając, A. Wawrzyniak, and M. Stankiewicz, SOLARIS National Synchrotron Radiation Centre in Krakow, Poland, *Eur. Phys. J. Plus* **138**, 10 (2023).
- [38] G. Kresse and D. Joubert, From ultrasoft pseudopotentials to the projector augmented-wave method, *Phys. Rev. B* **59**, 1758 (1999).
- [39] G. Kresse and J. Furthmüller, Efficient iterative schemes for ab initio total-energy calculations using a plane-wave basis set, *Phys. Rev. B* **54**, 11169 (1996).
- [40] G. Kresse and J. Hafner, Ab initio molecular-dynamics simulation of the liquid-metal–amorphous-semiconductor transition in germanium, *Phys. Rev. B* **49**, 14251 (1994).
- [41] J. P. Perdew, K. Burke, and M. Ernzerhof, Generalized gradient approximation made simple, *Phys. Rev. Lett.* **77**, 3865 (1996).
- [42] H. J. Monkhorst and J. D. Pack, Special points for Brillouin-zone integrations, *Phys. Rev. B* **13**, 5188 (1976).
- [43] M. P. L. Sancho, J. M. L. Sancho, J. M. L. Sancho, and J. Rubio, Highly convergent schemes for the calculation of bulk and surface Green functions, *J. Phys. F: Met. Phys.* **15**, 851 (1985).
- [44] Q. Wu, S. Zhang, H.-F. Song, M. Troyer, and A. A. Soluyanov, WannierTools: An open-source software package for novel topological materials, *Comput. Phys. Commun.* **224**, 405 (2018).
- [45] X. X. Yang, Y. Lu, S. Zhou, S. Mao, J. Mi, Z. Man, and J. Zhao, $RCu_{1+x}Sb_2$ ($R = La, Ce, Pr, Nd, Sm, Gd, Tb, Dy, Ho$ and Y) Phases with Defect $CaBe_2Ge_2$ -Type Structure, *Materials Science Forum* **475-479**, 861 (2005).
- [46] P. Zhang, P. Richard, T. Qian, Y.-M. Xu, X. Dai, and H. Ding, A precise method for visualizing dispersive features in image plots, *Rev. Sci. Instrum.* **82**, 043712 (2011).

8. Summary

This doctoral dissertation contains systematic ARPES studies of the following compounds: $\text{Fe}_{1-x}\text{M}_x\text{Te}_{1-y}\text{Se}_y$ ($\text{M} = \text{Co}, \text{Ni}; y \sim 0.35$), $\text{CaFe}_{2-x}\text{Co}_x\text{As}_2$ ($x = 0.07, 0.15$), LaAgSb_2 and LaCuSb_2 . For the tested compounds, the band structure was determined, Fermi surfaces were mapped, and experimental data were supported by theoretical calculations.

In the case of the two investigated iron-based superconductors, we observed the influence of doping with transition metal atoms on the electron structure; however, the observed effects have a different origin. For $\text{Fe}_{1-x}\text{M}_x\text{Te}_{1-y}\text{Se}_y$, along with the addition of impurities, we observe deformation of the electronic structure, consisting of shifting the bands and changing their slopes, leading to a change in the topology of the Fermi surface. Based on the available data, both collected as part of this doctoral thesis, as well as the literature on the transport properties of these specific compounds¹, it can be assumed that the effects are continuous. In the case of the $\text{CaFe}_{2-x}\text{Co}_x\text{As}_2$ samples we examined, the change in band structure that we observed was associated with a phase transition caused by a specific concentration of Co atoms. Despite examining samples located on the edge of a specific region in the phase diagram, we did not observe shifts or distortions of the electron structure. This indicates a different mechanism related to doping in these two superconductors, in $\text{Fe}_{1-x}\text{M}_x\text{Te}_{1-y}\text{Se}_y$ related to scattering on dopants and the introduction of additional interactions, while in $\text{CaFe}_{2-x}\text{Co}_x\text{As}_2$ it induces a phase transition.

We showed that CaFe_2As_2 hosts a Dirac cone for which there is indication of a connection with the phase of spin density waves, however, we did not observe an energy gap in the region of the presence of cones and where the characteristic features of the nodal SDW phase should be manifested.

LaCuSb_2 and LaAgSb_2 crystallize in the same structure, differing only slightly in lattice constants. The band structure of both compounds is similar; however, a number of differences are observed. The most significant and interesting is the one related to the nesting of the outer pocket on the Fermi surface. Surprisingly, it appears less clear for LaAgSb_2 in which the CDW phase is observed. The inner pocket is also different for both of these compounds; for LaCuSb_2 it has a richer structure and a three-dimensional character, while for LaAgSb_2 it is rather two-dimensional and resembles a flattened oval.

In both compounds, we observed similar nodal lines and linear bands that formed characteristic Dirac crossings. The nodal lines are located in the k_z direction, Dirac-like states can be observed in the vicinity of \bar{X} point and at the $\bar{\Gamma M}$ path. The existence of these states in LaCuSb_2 and LaAgSb_2 indicates the presence of Dirac fermions in both compounds.

9. List of Published Articles

Articles included in the thesis

1. Effect of electron doping in $\text{FeTe}_{1-y}\text{Se}_y$ realized by Co and Ni substitution
M. Rosmus, R. Kurlito, D. J. Gawryluk, J. Goraus, M. Z. Cieplak, P. Starowicz
Superconductor Science and Technology **32** (10), 2019, 105009
2. Electronic Band Structure and Surface States in Dirac Semimetal LaAgSb_2
M. Rosmus, N. Olszowska, Z. Bukowski, P. Starowicz, P. Piekarz, A. Ptok
Materials **15**, (20), 2022 7168

Articles co-authored by the author of the thesis

3. Studies of electronic structure across a quantum phase transition in $\text{CeRhSb}_{1-x}\text{Sn}_x$
R. Kurlito, J. Goraus, **M. Rosmus**, A. Ślebarski, P. Starowicz
The European Physical Journal B **92**, 2019, 1-812019
4. Photoemission signature of momentum-dependent hybridization in CeCoIn_5
R. Kurlito, M. Fidrysiak, L. Nicolaï, J. Minár, **M. Rosmus**, A. Tejada, J. E. Rault, F. Bertran, A. P. Kądziaława, D. Legut, D. Gnida, D. Kaczorowski, K. Kissner, F. Reinert, J. Spałek, P. Starowicz
Physical Review B **104** (12), 2021, 1251
5. Role of intercalated cobalt in the electronic structure of $\text{Co}_{1/3}\text{NbS}_2$
P. Popčević, Y. Utsumi, I. Biało, W. Tabiś, M. A. Gala, **M. Rosmus**, J. J. Kołodziej, N. Olszowska, M. Garb, H. Berger, I. Batistić, N. Barišić, L. Forró, E. Tutiš
Physical Review B **105** (15), 2022, 15511432022
6. Topological Lifshitz transition in Weyl semimetal NbP decorated with heavy elements
S. Wadge, B. J. Kowalski, C. Autieri, P. Iwanowski, A. Hruban, N. Olszowska, **M. Rosmus**, J. Kołodziej, A. Wiśniewski
Physical Review B **105** (23), 2022, 23530422022

7. Electronic properties of TaAs₂ topological semimetal investigated by transport and ARPES
 S. Wadge, G. Grabecki, C. Autieri, B. J. Kowalski, P. Iwanowski, G. Cuono, M.F. Islam, C. M. Canali, K. Dybko, A. Hruban, A. Łusakowski, T. Wojciechowski, R. Diduszko, A. Lynnyk, N. Olszowska, **M. Rosmus**, J. Kołodziej, A. Wiśniewski
 Journal of Physics: Condensed Matter **34** (12), 2022, 12560172022

8. Influence of Doping on the Topological Surface States of Crystalline Bi₂Se₃ Topological Insulators
 K. Nowak, M. Jurczyszyn, M. Chrobak, K. Maćkosz, A. Naumov, N. Olszowska, **M. Rosmus**, I. Miotkowski, A. Kozłowski, M. Sikora, M. Przybylski
 Materials **15** (6), 2022, 208322022

9. SOLARIS national synchrotron radiation centre in Krakow, Poland
 J. Szlachetko, J. Szade, E. Beyer, W. Błachucki, P. Ciochoń, P. Dumas, K. Freindl, G. Gazdowicz, S. Glatt, K. Guła, J. Hormes, P. Indyka, A. Klonecka, J. Kołodziej, T. Kołodziej, J. Korecki, P. Korecki, F. Kosiorowski, K. Kosowska, G. Kowalski, M. Kozak, P. Kozioł, W. Kwiatek, D. Liberda, H. Lichtenberg, E. Madej, A. Mandziak, A. Marendziak, K. Matlak, A. Maximenko, P. Nita, N. Olszowska, R. Panaś, E. Partyka-Jankowska, M. Piszak, A. Prange, M. Rawski, M. Roman, **M. Rosmus**, M. Sikora, J. Sławek, T. Sobol, K. Sowa, N. Spiridis, J. Stępień, M. Szczepanik, T. Ślęzak, T. Tyliczszak, G. Ważny, J. Wiechecki, D. Wilgocka-Ślęzak, B. Wolanin, P. Wróbel, T. Wróbel, M. Zając, A. Wawrzyniak, M. Stankiewicz
 The European Physical Journal Plus **138** (1), 2023, 1-102023

10. Fermiology of Chiral Cadmium Diarsenide CdAs₂, a Candidate for Hosting Kramers–Weyl Fermions
 F. Mazzola, Y. Zhang, N. Olszowska, **M. Rosmus**, G. D’Olimpio, M. C. Istrate, G.G. Politano, I. Vobornik, R. Sankar, C. Ghica, J. Gao, A. Politano
 The Journal of Physical Chemistry Letters **14**, 2023, 3120-3125

11. Band structure of a nonparabolic two-dimensional electron gas system
 D. Wutke, M. Garb, A. Krawczyk, A. Mielczarek, N. Olszowska, **M. Rosmus**, J. J. Kołodziej
 Physical Review B **107** (15), 2023, 155139

10. Bibliography

1. Bezusyy, V. L., Gawryluk, D. J., Malinowski, A. & Cieplak, M. Z. Transition-metal substitutions in iron chalcogenides. *Phys. Rev. B - Condens. Matter Mater. Phys.* **91**, 1–5 (2015).
2. Harnagea, L. *et al.* Phase diagram of the iron arsenide superconductors $\text{Ca}(\text{Fe}_{1-x}\text{Co}_x)_2\text{As}_2$ ($0 \leq x \leq 0.2$). *Phys. Rev. B - Condens. Matter Mater. Phys.* **83**, 1–10 (2011).
3. Ali, K. & Maiti, K. Emergent electronic structure of CaFe_2As_2 . *Sci. Rep.* **7**, 1–17 (2017).
4. Chen, F. *et al.* Electronic structure reconstruction of CaFe_2As_2 in the spin density wave state. in *Journal of Physics and Chemistry of Solids* vol. 72 469–473 (2011).
5. Yi, M. *et al.* Symmetry-breaking orbital anisotropy observed for detwinned $\text{Ba}(\text{Fe}_{1-x}\text{Co}_x)_2\text{As}_2$ above the spin density wave transition. *Proc. Natl. Acad. Sci. U. S. A.* **108**, 6878–6883 (2011).
6. Muro, Y., Takeda, N. & Ishikawa, M. Magnetic and transport properties of dense Kondo systems, CeTSb_2 (T=Ni, Cu, Pd and Ag). *J. Alloys Compd.* **257**, 23–29 (1997).
7. Akiba, K., Umeshita, N. & Kobayashi, T. C. Observation of superconductivity and its enhancement at the charge density wave critical point in LaAgSb_2 . *Phys. Rev. B* **106**, 161113 (2022).
8. Song, C. *et al.* Charge-density-wave orderings in LaAgSb_2 : An x-ray scattering study. *Phys. Rev. B - Condens. Matter Mater. Phys.* **68**, 1–6 (2003).
9. Zhang, P. *et al.* Observation of topological superconductivity on the surface of an iron-based superconductor. *Science* **360**, 182–186 (2018).
10. Xu, G., Lian, B., Tang, P., Qi, X. L. & Zhang, S. C. Topological Superconductivity on the Surface of Fe-Based Superconductors. *Phys. Rev. Lett.* **117**, 047001 (2016).
11. Richard, P. *et al.* Observation of dirac cone electronic dispersion in BaFe_2As_2 . *Phys. Rev. Lett.* **104**, 2–5 (2010).
12. Pan, L. *et al.* Evolution of the Fermi surface topology in doped 122 iron pnictides. *Phys. Rev. B - Condens. Matter Mater. Phys.* **88**, 1–7 (2013).
13. Ran, Y., Wang, F., Zhai, H., Vishwanath, A. & Lee, D. H. Nodal spin density wave and band topology of the FeAs-based materials. *Phys. Rev. B - Condens. Matter Mater. Phys.* **79**, 1–9 (2009).
14. Shi, X. *et al.* Observation of Dirac-like band dispersion in LaAgSb_2 . *Phys. Rev. B* **93**, 1–5 (2016).
15. Chamorro, J. R. *et al.* Dirac fermions and possible weak antilocalization in LaCuSb_2 . *Appl. Phys. Rev.* **7**, (2019).
16. Ruszała, P., Winiarski, M. J. & Samsel-Czekala, M. Dirac-like band structure of LaTESb_2 (TE = Ni, Cu, and Pd) superconductors by DFT calculations. *Comput. Mater. Sci.* **154**, 106–110 (2018).
17. Józef Spalek. *Wstęp do fizyki materii skondensowanej*. (PWN, 2015).
18. Onnes, H. K. Further experiments with liquid helium. C. On the change of electric resistance of pure metals at very low temperatures etc. IV. The resistance of pure mercury at helium temperatures. 261–263 (1991) doi:10.1007/978-94-009-2079-8_15.
19. Gor'kov, L. P. Microscopic Derivation Of The Ginzburg-Landau Equations In The

- Theory Of Superconductivity. *J Exptl Theor. Phys USSR* **36**, 1918–1923 (1959).
20. Monthoux, P., Balatsky, A. V. & Pines, D. Weak-coupling theory of high-temperature superconductivity in the antiferromagnetically correlated copper oxides. *Phys. Rev. B* **46**, (1992).
 21. Duan, D., Yu, H., Xie, H. & Cui, T. Ab Initio Approach and Its Impact on Superconductivity. *J. Supercond. Nov. Magn.* **32**, 53–60 (2019).
 22. Bednorz, J. G. & Miiller, K. A. *Condensed Possible High T_c Superconductivity in the Ba-La-Cu-0 System.* *Z. Phys. B-Condensed Matter* vol. 64 189–193 (1986).
 23. Kamihara, Y. *et al.* Iron-based layered superconductor: LaOFeP. *J. Am. Chem. Soc.* **128**, 10012–10013 (2006).
 24. Ge, J. F. *et al.* Superconductivity above 100 K in single-layer FeSe films on doped SrTiO₃. *Nat. Mater.* 2014 143 **14**, 285–289 (2014).
 25. Bardeen, J., Cooper, L. N. & Schrieffer, J. R. Microscopic Theory of Superconductivity. *Phys. Rev.* **106**, 162 (1957).
 26. Kamihara, Y., Watanabe, T., Hirano, M. & Hosono, H. Iron-based layered superconductor La[O_{1-x}F_x]FeAs (x= 0.05-0.12) with T_c = 26 K. *J. Am. Chem. Soc.* **130**, 3296–3297 (2008).
 27. Johannes, M., Subedi, A., Zhang, L., Singh, D. J. & Du, M. H. The iron age of superconductivity Subject Areas: Superconductivity A Viewpoint on: Density functional study of FeS, FeSe, and FeTe: Electronic structure, magnetism, phonons, and superconductivity. *Phys Rev B* **1**, 134514 (2008).
 28. Liu, X. *et al.* Electronic structure and superconductivity of FeSe-related superconductors. *J. Phys. Condens. Matter* **27**, (2015).
 29. Mizuguchi, Y. & Takano, Y. Review of Fe chalcogenides as the simplest Fe-based superconductor. *J. Phys. Soc. Jpn.* **79**, 1–2 (2010).
 30. King, S. F., Roberts, J. P., Hirschfeld, P. J., Korshunov, M. M. & Mazin, I. I. Reports on Progress in Physics Gap symmetry and structure of Fe-based superconductors. *Prog. Phys. Rep Prog Phys* **74**, 124508–124552 (2011).
 31. Thirupathaiyah, S. *et al.* Effect of impurity substitution on band structure and mass renormalization of the correlated FeTe_{0.5}Se_{0.5} superconductor. *Phys. Rev. B* **93**, 1–7 (2016).
 32. Wu, X., Qin, S., Liang, Y., Fan, H. & Hu, J. Topological characters in Fe(Te_{1-x}Se_x) thin films. *Phys. Rev. B* **93**, 115129 (2016).
 33. Wang, Z. *et al.* Topological nature of the FeSe_{0.5}Te_{0.5} superconductor. *Phys. Rev. B - Condens. Matter Mater. Phys.* **92**, 115119 (2015).
 34. Tai, Y. Y., Zhu, J. X., Graf, M. J. & Ting, C. S. Calculated phase diagram of doped BaFe₂As₂ superconductor in a C4-symmetry breaking model. *Epl* **103**, (2013).
 35. Biswal, G. & Mohanta, K. L. A recent review on iron-based superconductor. *Mater. Today Proc.* **35**, 207–215 (2021).
 36. Chu, J. H., Analytis, J. G., Kucharczyk, C. & Fisher, I. R. Determination of the phase diagram of the electron-doped superconductor Ba(Fe_{1-x}Co_x)₂As₂. *Phys. Rev. B - Condens. Matter Mater. Phys.* **79**, 1–6 (2009).
 37. Ni, N. *et al.* First-order structural phase transition in CaFe₂As₂. *Phys. Rev. B - Condens. Matter Mater. Phys.* **78**, 1–5 (2008).
 38. Liu, C. *et al.* Evidence for a Lifshitz transition in electron-doped iron arsenic superconductors at the onset of superconductivity. *Nat. Phys.* **6**, 419–423 (2010).

39. Lifshitz, M. Anomalies of electron characteristics of a metal in the high pressure region. *Soviet Physics JETP*, **11**, 1130-1135.
40. Kordyuk, A. A. Iron-based superconductors: Magnetism, superconductivity, and electronic structure (Review Article). *Low Temp. Phys.* **38**, 888 (2012).
41. Leijnse, M. & Flensberg, K. Introduction to topological superconductivity and Majorana fermions. *Semicond. Sci. Technol.* **27**, 124003 (2012).
42. Alicea, J. New directions in the pursuit of Majorana fermions in solid state systems. *Rep. Prog. Phys.* **75**, (2012).
43. Moore, J. E. The birth of topological insulators. *Nature* **464**, 194–198 (2010).
44. Haldane, F. D. M. Nobel lecture: Topological quantum matter. *Rev. Mod. Phys.* **89**, 1–10 (2017).
45. Wang, J. *Special Topic: Topological Matter Superconductivity in topological semimetals*. *National Science Review* **6**, 199–202 (2019)
46. Bhardwaj, V. & Chatterjee, R. Topological Materials: New Quantum Phases of Matter. *Resonance* **25**, 431–441 (2020).
47. Hasan, M. Z. & Kane, C. L. Colloquium: Topological insulators. *Rev. Mod. Phys.* **82**, 3045–3067 (2010).
48. Shen, S.-Q. *Topological Insulators*. vol. 187 (Springer Singapore, 2017).
49. Thouless, D. J., Kohmoto, M., Nightingale, M. P. & den Nijs, M. Quantized Hall Conductance in a Two-Dimensional Periodic Potential. *Phys. Rev. Lett.* **49**, 405–408 (1982).
50. Avron, J. E., Osadchy, D. & Seiler, R. A topological look at the quantum hall effect. *Phys. Today* **56**, 38–42 (2003).
51. Chen, Y. *et al.* Recent Advances in Topological Quantum Materials by Angle-Resolved Photoemission Spectroscopy. *Matter* **3**, 1114–1141 (2020).
52. Hsieh, D. *et al.* A tunable topological insulator in the spin helical Dirac transport regime. *Nature* **460**, 1101–1105 (2009).
53. Chen, Y. L. *et al.* Massive Dirac Fermion on the Surface of a Magnetically Doped Topological Insulator. *Science* **329**, 5992 659-662
54. Zhang, H. *et al.* Topological insulators in Bi₂Se₃, Bi₂Te₃ and Sb₂Te₃ with a single Dirac cone on the surface. *Nat. Phys.* **2009 56 5**, 438–442 (2009).
55. Chen, Y. L. *et al.* Single dirac cone topological surface state and unusual thermoelectric property of compounds from a new topological insulator family. *Phys. Rev. Lett.* **105**, (2010).
56. Lin, H. *et al.* Single-dirac-cone topological surface states in the TlBiSe₂ class of topological semiconductors. *Phys. Rev. Lett.* **105**, (2010).
57. Fang, C., Weng, H., Dai, X. & Fang, Z. Topological nodal line semimetals. *Chin. Phys. B* **25**, (2016).
58. Xu, S.-Y. *et al.* Observation of Fermi arc surface states in a topological metal. *Science* **347**, 294–298 (2015).
59. Wang, Z., Weng, H., Wu, Q., Dai, X. & Fang, Z. Three-dimensional Dirac semimetal and quantum transport in Cd₃As₂. *Phys. Rev. B - Condens. Matter Mater. Phys.* **88**, (2013).
60. Yang, L. X. *et al.* Weyl semimetal phase in the non-centrosymmetric compound TaAs. *Nat. Phys.* **11**, 728–732 (2015).

61. Lv, B. Q. *et al.* Observation of Weyl nodes in TaAs. *Nat. Phys.* **11**, 724–727 (2015).
62. Weng, H., Fang, C., Fang, Z., Andrei Bernevig, B. & Dai, X. Weyl semimetal phase in noncentrosymmetric transition-metal monophosphides. *Phys. Rev. X* **5**, (2015).
63. Lv, B. Q. *et al.* Experimental discovery of weyl semimetal TaAs. *Phys. Rev. X* **5**, (2015).
64. Jiang, J. *et al.* Signature of type-II Weyl semimetal phase in MoTe₂. *Nat. Commun.* **8**, (2017).
65. Kim, Y., Wieder, B. J., Kane, C. L. & Rappe, A. M. Dirac Line Nodes in Inversion-Symmetric Crystals. *Phys. Rev. Lett.* **115**, (2015).
66. Chen, Y. *et al.* Nanostructured Carbon Allotropes with Weyl-like Loops and Points. *Nano Lett.* **15**, 6974–6978 (2015).
67. Xu, G., Weng, H., Wang, Z., Dai, X. & Fang, Z. Chern semimetal and the quantized anomalous Hall effect in HgCr₂Se₄. *Phys. Rev. Lett.* **107**, (2011).
68. Bzdušek, T., Wu, Q. S., Rüegg, A., Sigrist, M. & Soluyanov, A. A. Nodal-chain metals. *Nature* **538**, 75–78 (2016).
69. Wu, Y. *et al.* Dirac node arcs in PtSn₄. *Nat. Phys.* **12**, 667–671 (2016).
70. Ekahana, S. A. *et al.* Observation of nodal line in non-symmorphic topological semimetal InBi. *New J. Phys.* **19**, (2017).
71. Song, Y. K. *et al.* Photoemission Spectroscopic Evidence for the Dirac Nodal Line in the Monoclinic Semimetal SrAs₃. *Phys. Rev. Lett.* **124**, (2020).
72. Bian, G. *et al.* Topological nodal-line fermions in spin-orbit metal PbTaSe₂. *Nat. Commun.* **7**, 1–8 (2016).
73. Chen, C. *et al.* Dirac line nodes and effect of spin-orbit coupling in the nonsymmorphic critical semimetals MSiS (M=Hf, Zr). *Phys. Rev. B* **95**, (2017).
74. Bradlyn, B. *et al.* Beyond Dirac and Weyl fermions: Unconventional quasiparticles in conventional crystals. *Science* **353**, (2016).
75. Chang, G. *et al.* Topological quantum properties of chiral crystals. *Nat. Mater.* **17**, 978–985 (2018).
76. Noji, T. *et al.* Growth, annealing effects on superconducting and magnetic properties, and anisotropy of FeSe_{1-x}Te_x (0.5 ≤ x ≤ 1) single crystals. *J. Phys. Soc. Jpn.* **79**, 1–5 (2010).
77. Fang, M. H. *et al.* Superconductivity close to magnetic instability in Fe(Se_{1-x}Te_x)_{0.82}. *Phys. Rev. B - Condens. Matter Mater. Phys.* **78**, 1–5 (2008).
78. Dong, C. *et al.* Revised phase diagram for the FeTe_{1-x}Se_x system with fewer excess Fe atoms. *Phys. Rev. B - Condens. Matter Mater. Phys.* **84**, 1–6 (2011).
79. Liu, T. J. *et al.* From (π,0) magnetic order to superconductivity with (π,π) magnetic resonance in Fe_{1.02}Te_{1-x}Se_x. *Nat. Mater.* **2010** **9**, 718–720 (2010).
80. Hsu, F. C. *et al.* Superconductivity in the PbO-type structure α-FeSe. *Proc. Natl. Acad. Sci. U. S. A.* **105**, 14262–14264 (2008).
81. Sun, Y., Yamada, T., Pyon, S. & Tamegai, T. Influence of interstitial Fe to the phase diagram of Fe_{1+y}Te_{1-x}Se_x single crystals. *Sci. Rep.* **6**, 1–8 (2016).
82. Katayama, N. *et al.* Investigation of the Spin-Glass Regime between the Antiferromagnetic and Superconducting Phases in Fe_{1+y}Se_xTe_{1-x}. *J. Phys. Soc. Jpn.* **79**, 1–4 (2010).
83. Inabe, T., Kawamata, T., Noji, T., Adachi, T. & Koike, Y. Superconducting

- symmetry studied from impurity effects in single-crystal $\text{Fe}_{1-y}\text{MySe}_{0.3}\text{Te}_{0.7}$ ($M = \text{Co, Ni, Zn}$). *J. Phys. Soc. Jpn.* **82**, (2013).
84. Neupane, M. *et al.* Electron-hole asymmetry in the superconductivity of doped BaFe_2As_2 seen via the rigid chemical-potential shift in photoemission. *Phys. Rev. B* **83**, 94522 (2011).
 85. Ideta, S. *et al.* Dependence of Carrier Doping on the Impurity Potential in Transition-Metal-Substituted FeAs-Based Superconductors. *Phys. Rev. Lett.* **110**, 107007 (2013)
 86. Vilmercati, P. *et al.* Nonrigid band shift and nonmonotonic electronic structure changes upon doping in the normal state of the pnictide high-temperature superconductor $\text{Ba}(\text{Fe}_{1-x}\text{Co}_x)_2\text{As}_2$. *Phys. Rev. B* **94**, 1–14 (2016).
 87. Canfield, P. C. *et al.* Structural, magnetic and superconducting phase transitions in CaFe_2As_2 under ambient and applied pressure. *Phys. C Supercond. Its Appl.* **469**, 404–412 (2009).
 88. Wang, Q. *et al.* Symmetry-broken electronic structure and uniaxial Fermi surface nesting of untwinned CaFe_2As_2 . *Phys. Rev. B - Condens. Matter Mater. Phys.* **88**, 1–6 (2013).
 89. Matusiak, M., Bukowski, Z. & Karpinski, J. Nernst effect in single crystals of the pnictide superconductor $\text{CaFe}_{1.92}\text{Co}_{0.08}\text{As}_2$ and parent compound CaFe_2As_2 . *Phys. Rev. B - Condens. Matter Mater. Phys.* **81**, 90–93 (2010).
 90. Xu, B. *et al.* Optical study of Dirac fermions and related phonon anomalies in the antiferromagnetic compound CaFeAsF . *Phys. Rev. B* **97**, 1–6 (2018).
 91. Terashima, T. *et al.* Fermi Surface with Dirac Fermions in CaFeAsF Determined via Quantum Oscillation Measurements. *Phys. Rev. X* **8**, 11014 (2018).
 92. Chen, Z. G. *et al.* Two-Dimensional Massless Dirac Fermions in Antiferromagnetic AFe_2As_2 ($A = \text{Ba, Sr}$). *Phys. Rev. Lett.* **119**, 1–6 (2017).
 93. Matusiak, M. & Wolf, T. In-plane transport anisotropy in a $\text{Ba}_{1-x}\text{K}_x\text{Fe}_2\text{As}_2$ iron-based superconductor. *Supercond. Sci. Technol.* **32**, (2019).
 94. Huynh, K. K., Tanabe, Y. & Tanigaki, K. Both electron and hole Dirac cone states in $\text{Ba}(\text{FeAs})_2$ confirmed by magnetoresistance. *Phys. Rev. Lett.* **106**, 1–4 (2011).
 95. Sutherland, M. *et al.* Evidence for Dirac nodes from quantum oscillations in SrFe_2As_2 . *Phys. Rev. B - Condens. Matter Mater. Phys.* **84**, 1–5 (2011).
 96. Richard, P. *et al.* Observation of dirac cone electronic dispersion in BaFe_2As_2 . *Phys. Rev. Lett.* **104**, (2010).
 97. Armitage, N. P., Mele, E. J. & Vishwanath, A. Weyl and Dirac semimetals in three-dimensional solids. *Rev. Mod. Phys.* **90**, 15001 (2018).
 98. Hase, I. & Yanagisawa, T. Electronic Band Calculation of LaTSb_2 ($T = \text{Cu, Ag, Au}$). *Phys. Procedia* **58**, 42–45 (2014).
 99. Yang, X. X. *et al.* $\text{RCu}_{1+x}\text{Sb}_2$ ($R = \text{La, Ce, Pr, Nd, Sm, Gd, Tb, Dy, Ho}$ and Y) Phases with Defect CaBe_2Ge_2 -Type Structure. *Mater. Sci. Forum* **475–479**, 861–864 (2005).
 100. Gondek, L., Penc, B., Szytula, A. & Stusser, N. Thermal dependence of the lattice constants of LaAgSb_2 . *J. Alloys Compd.* **346**, 80–83 (2002).
 101. Bosak, A. *et al.* Evidence for nesting-driven charge density wave instabilities in the quasi-two-dimensional material LaAgSb_2 . **033020**, 1–11 (2021).

102. Myers, K. D., Antropov, V. P., Harmon, B. N., Canfield, P. C. & Lacerda, A. H. de Haas – van Alphen and Shubnikov – de Haas oscillations in RAgSb₂ (R=Y, La-Nd, Sm).
Physical Review B **60**, 371–379 (1999).
103. Myers, K. D. *et al.* Systematic study of anisotropic transport and magnetic properties of RAgSb₂ (R = Y, La-Nd, Sm, Gd-Tm). *J. Magn. Magn. Mater.* **205**, 27–52 (1999).
104. Wang, K. & Petrovic, C. Multiband effects and possible Dirac states in LaAgSb₂. *Phys. Rev. B - Condens. Matter Mater. Phys.* **86**, 1–7 (2012).
105. Damascelli, A., Hussain, Z. & Shen, Z. X. Angle-resolved photoemission studies of the cuprate superconductors. *Rev. Mod. Phys.* **75**, 473–541 (2003).
106. Damascelli, A. Probing the Electronic Structure of Complex Systems by ARPES. *Phys. Scr.* **T109**, 61 (2004).
107. Szlachetko, J. *et al.* SOLARIS National Synchrotron Radiation Centre in Krakow, Poland. *Eur Phys J Plus* **138**, 10 (2023).
108. URANOS - Narodowe Centrum Promieniowania Synchrotronowego SOLARIS - Uniwersytet Jagielloński. <https://synchrotron.uj.edu.pl/linie-badawcze/uranos>.